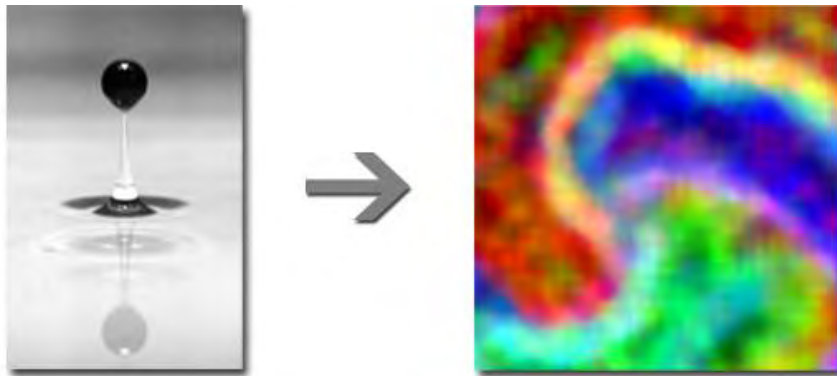


# Wet granular dynamics:

From single particle bouncing  
to collective motion



HABILITATION THESIS

submitted to

Fakultät für Mathematik, Physik und Informatik  
Universität Bayreuth

**Kai Huang**

Bayreuth

July 13, 2014



# **Wet granular dynamics:**

From single particle bouncing  
to collective motion

HABILITATION THESIS

submitted to

Fakultät für Mathematik, Physik und Informatik  
Universität Bayreuth

**Kai Huang**

Experimentalphysik V, Universität Bayreuth  
95440 Bayreuth, Germany

Bayreuth

July 13, 2014



For *Nian & Jovin*  
for the power of love



## Preface

Bayreuth, July 13, 2014

Dating back to 1300 B.C., the word ‘sand’ (沙) had already been used in Chinese bronze inscriptions as one of the earliest words. The desire to communicate on sand at the very beginning of the language evolution demonstrates the ubiquity of granular matter. Since then, the attempts of mankind to describe and understand such a material have never stopped. For example, in the epic poem ‘On the nature of things’ written in around 55 B.C., Lucretius describes granular flow as the following [Carus & Leonard, 2004]:

“ ...To suck the poppy-seeds from palm of hand  
Is quite as easy as drinking water down,  
And they, once struck, roll like unto the same.”

Such daily life experience shows the liquid like behaviour of granular matter. However, a little more strictly speaking, to which extend such a granular liquid behaves like a simple liquid in thermodynamic equilibrium? What can we learn from this similarity? How to classify and define physical quantities of such a ‘liquid’? Could it be possible to have a continuum description of its flow? For granular flow, in addition to the ‘macroscopic’ perspective, it is also feasible to take the ‘microscopic’ perspective and discuss the collective behaviour from the mobility of individual particles. What can we learn from the connections between both perspectives?

My efforts to address the above questions during the period from 2006 to 2014 are summarized in this cumulative habilitation thesis. In particular, the case with cohesion arising from wetting liquid added to the particles is focused, because of its importance in real life applications. In Chapter 1, a more detailed description of the motivation for the research, from both physical and industrial perspectives, together with a brief review of the advances in this field are given. From a ‘microscopic’ point of view, Chapter 2 is devoted to the particle-particle interactions with the wetting liquid mediated. The intrinsic time, length and energy scales associated with the impacts and a collisional model are described. From a ‘macroscopic’ point of view, Chapter 3 contains the collective behaviour of granular matter: From phase transitions to pattern formation. Comparisons between dry and wet granular dynamics, and recent efforts on the dynamics of aspherical particles are also included. Finally in Chapter 4, the connections

between dynamics at both ‘microscopic’ and ‘macroscopic’ levels, as well as the links between systems in and out of thermodynamic equilibrium, are summarized, in order to provide a general framework for further studies and to shed light on the widespread applications. In Chapters 6 and 7, detailed descriptions of the work in preprint and published forms are attached. In the thesis, these articles are cited with links to their first pages. All internal links are painted with dark brown, i.e., a color of sand.

Part of the work presented in the thesis is supported by the Deutsche Forschungsgemeinschaft (DFG) through grant number HU1939/2-1.

The research I have been carrying out would not be possible without the support and help from all the colleagues I have been working with. First of all, I would like to take this chance to thank all of them.

I am grateful to Stephan Herminghaus, for giving me the opportunity to continue my academic career in Germany after my Ph.D, and for providing me indispensable support during my stay in the Max Planck Institute for Dynamics and Self-organization in Göttingen. I have enjoyed the enlightening discussions and active collaborations with Matthias Schröter, Martin Brinkmann, Jürgen Vollmer and Ralf Seemann since my stay in Göttingen. I would also like to thank former colleagues Axel Hager-Fingerle, Masound Sohaili, Mario Scheel and Klaus Röller, for helping me both with my research and personal life. I always remembers their warm-hearted help when I tried to settle down in this very much different country 8 years ago.

I would also like to express my deep gratitude to Ingo Rehberg, for providing me the opportunity to continue my career as the leader of the sand group in Experimentalphysik V. His enthusiastic encouragement, helpful hints and critiques are always beneficial. I would also like to extend my acknowledgement to my predecessor Christof Krülle, for his continuous support since I started in Bayreuth, especially for those days he drove more than 600 kilometers to attend the weekly seminar of the sand group. I am also grateful to Reinhard Richter, for his help both as a colleague and as a friend. It is also a pleasure to appreciate all my students during the past 5 years: Frank Gollwitzer, Christopher May, Michael Wild, Lorenz Butzhammer, Laura Meißner, Felix Ott, Philipp Ramming, Simeon Völkel, and Thomas Müller.

Special thanks to the other mentors of the habilitation thesis, Thomas Fischer and Matthias Schmidt, for their helpful hints on my career. I should also extend my acknowledgement to Andrea Fortini and Daniel de las Heras, for the enlightening discussions on our recent collaborations.

Most of all, I would like to thank my wife Nian, for her love over the past 15 years, for caring about me more than I myself do, and for giving birth to our son, Jovin.

## Contents

<b>Preface</b>	<b>i</b>
<b>1 Introduction</b>	<b>1</b>
1.1 A classification	1
1.2 Motivation	4
1.3 A brief historical review	7
<b>2 ‘Microscopic’ interactions</b>	<b>11</b>
2.1 Dry impact	13
2.2 Wet impact	17
2.2.1 Influence from surface tension	19
2.2.2 Influence from viscosity	23
2.2.3 Influence from inertia	25
2.3 Scaling	26
2.4 Wetting	30
<b>3 Collective behaviour</b>	<b>33</b>
3.1 How wet is wet?	34
3.2 Dry granular dynamics: A brief review	35
3.3 Wet granular dynamics under horizontal agitations	40
3.3.1 Surface melting under swirling motion	40
3.3.2 Clustering under steady shear flow	46
3.4 Wet granular dynamics under vertical agitations	51
3.4.1 Melting	51
3.4.2 Granular ‘gas bubbles’	54
3.4.3 Phase diagram and scaling laws	58
3.4.4 Pattern formation	60
3.5 How does shape matter?	65
3.5.1 Granular rods	65
3.5.2 Hexagonal disks and more	67
<b>4 Concluding remarks</b>	<b>69</b>
<b>5 Bibliography</b>	<b>71</b>

<b>6 Preprint Articles</b>	<b>83</b>
[P1] FORTINI, A. & HUANG, K. 2014 Role of defects in the onset of wall-induced granular convection. (submitted to <i>Phys. Rev. E</i> )	83
[P2] MÜLLER, T., DE LAS HERAS, D., REHBERG, I. & HUANG, K. 2014 Ordering of granular rods driven far from thermodynamic equilibrium. (to be submitted)	90
<b>7 Recent Articles</b>	<b>95</b>
[R1] MAY, C., WILD, M., REHBERG, I. & HUANG, K. 2013 Analog of surface melting in a macroscopic nonequilibrium system. <i>Phys. Rev. E</i> <b>88</b> , 062201.	95
[R2] MÜLLER, T., GOLLWITZER, F., KRÜLLE, C. A., REHBERG, I. & HUANG, K. 2013 Scaling of the normal coefficient of restitution for wet impacts. <i>AIP Conf. Proc.</i> <b>1542</b> , 787.	101
[R3] HUANG, K., BUTZHAMMER, L. & REHBERG, I. 2013 Scaling of the normal coefficient of restitution for wet impacts. <i>AIP Conf. Proc.</i> <b>1542</b> , 702.	106
[R4] GOLLWITZER, F., REHBERG, I., KRÜLLE, C. A. & HUANG, K. 2012 Coefficient of restitution for wet particles. <i>Phys. Rev. E</i> <b>86</b> , 011303.	111
[R5] HUANG, K., BRINKMANN, M. & HERMINGHAUS, S. 2012 Wet granular rafts: aggregation in two dimensions under shear flow. <i>Soft Matter</i> <b>8</b> , 11939.	120
[R6] HUANG, K. & REHBERG, I. 2011 Period Tripling Causes Rotating Spirals in Agitated Wet Granular Layers. <i>Phys. Rev. Lett.</i> <b>107</b> , 028001.	130
[R7] HUANG, K., KRÜLLE, C. & REHBERG, I. 2010 Snooping in the sand. <i>ZAMM - J. Appl. Math. Mech.</i> <b>90</b> , 911.	134
[R8] HUANG, K., SOHAILI, M., SCHRÖTER, M. & HERMINGHAUS, S. 2009a Fluidization of granular media wetted by liquid He <sup>4</sup> . <i>Phys. Rev. E</i> <b>79</b> , 010301.	143
[R9] HUANG, K., RÖLLER, K. & HERMINGHAUS, S. 2009b Universal and non-universal aspects of wet granular matter under vertical vibrations. <i>Eur. Phys. J. Spec. Top.</i> <b>179</b> , 25.	147
[R10] FELTRUP, A., HUANG, K., KRÜLLE, C. A. & REHBERG, I. 2009 The rotation-reptation transition under broken rotational symmetry. <i>Eur. Phys. J. Spec. Top.</i> <b>179</b> , 19.	155
[R11] FINGERLE, A., ROELLER, K., HUANG, K. & HERMINGHAUS, S. 2008 Phase transitions far from equilibrium in wet granular matter. <i>New J. Phys.</i> <b>10</b> , 053020.	161

## 1.1 A classification

As large agglomerations of macroscopic particles, granular materials are ubiquitous in the universe. From the LCROSS project that found icy water on the moon through exploring the granular jet created by an impact on a crater of the moon in 2009 [Kerr, 2010; Colaprete *et al.*, 2010], to the activities of the latest Mars rover curiosity landing in 2013 [MSL, 2013], our endeavours to explore the universe are becoming more and more closely related to the dynamics of granular matter. No need to mention the Saturn's rings, typical examples of granular gases, which are composed of icy particles spreading hundreds of thousand of kilometers in a rather thin layer with a few tens of meters thick [Cassini, 2014]. Modelling the evolution of such rings and wave propagations inside in response to external perturbations are believed to shed light on the early stage of planet formation [Crida & Charnoz, 2012].

Back to the earth, the dynamics of *wet* granular matter is of more importance, since our blue planet is largely covered with water. Every child knows that something tremendous is happening when a small amount of water is added into sand. It is the magic played by the water added that enables all the fun of playing sand on the beach. Despite of the omnipresence of such experiences, it is not until very recent physicists start to find a clue on the stability of wet sand with the help of X-ray tomography [Scheel *et al.*, 2008]. Generally speaking, the complexity of such kind of problems in static wet granular matter arises from the heterogeneities in both particle packings and liquid distributions.

Concerning the packing of spheres of the same size as a starting point, Kepler's conjecture states that the maximum packing density is the face-centered-cubic (FCC) packing with a packing density  $\phi = \pi/\sqrt{18} \approx 0.74$ , where  $\phi$  is defined as the volume of the spheres over the total volume that the particles occupy. In 1831, Gauß proved that particles packed in a regular lattice indeed have such a maximum packing density. However, how to prove for the endless irregular packing? In 1951, Tóth showed that this infinite number of configurations can be reduced to a finite but large number. With the help of computer simulations, Hales finally showed a proof of Kepler's conjecture in 2005 [Hales, 2005], which was concluded to be more than 99% complete by the 12 referees from Annuals of Mathematics, after 4 years of reviewing process. Despite of such a success, packing of mono-disperse spheres in reality will not have the energetically favoured FCC packing. Instead, a packing density between the so called random close packing (RCP, with  $\phi \approx 0.64$ ) [Scott, 1960; Scott & Kilgour, 1969] and random loose

packing (RLP, with  $\phi \approx 0.56$ ) [Onoda & Liniger, 1990] will be a more reasonable guess. Moreover, the packing of aspherical particles is a dramatically different story: Turning spheres into ellipsoids can easily lead to an enhanced RCP of  $\phi > 0.70$ , a trick used by M&M<sup>®</sup> to pack the candies more efficiently in a jar [Donev *et al.*, 2004]. As to poly-disperse particles, the Arab saying

“You think your basket is full when you have stuffed it with oranges. In truth, it is full of void, for you can still add nuts, and even chickpeas after that.”

actually elucidates the pathway towards a more and more dense packing, correspondingly a more and more rigid structure in terms of granulates used in civil engineering. Additionally, no sand grains are the same in nature, not even look the same. The collection of microscopic photography by Gary Greenberg [Greenberg, 2008] nicely demonstrates such a diversity, and tells us that walking on the beach is actually an experience of travelling along millions of years of biological and geological history.

On the other hand, the cohesion induced by the additional wetting liquid strongly depends on the geometry of the liquid within the voids of packing. This cohesion will most likely change the local packing of particles, triggering a feedback on the distribution of the wetting liquid. Such an interaction will eventually lead to a steady state with an enhanced overall rigidity compared with a dry granular packing. As a consequence, the sand does not have an angle of repose any more, and is ready to be sculptured into almost any shape we want. Without disturbance, a sand sculpture will stay forever, because the thermal energy scale is orders of magnitude smaller than the local potential energy scale required to change the packing. That is the hallmark separating granular from colloidal particles [Duran, 2000]. Typically, the realm of granulates compose of particles with a size range from a few microns such as clay particles to a few thousand kilometers such as large ice floes, covering 12 orders of magnitude.

Figure 1.1 (a) shows an example of wet granular matter in a liquidlike state. The photo was taken in a jumping competition in London Olympic Games 2012. During the impact of the athlete with the wet sand, the kinetic energy transferred to the wet sand drives it into the liquidlike state. In such a situation, wet granular matter acts as an effective damper to protect the player. Compared with sand flowing in an hour glass, or with sand saltating during dune migrations, agitated wet sand behaves differently: The kinetic energy injected doesn't enter the translational and rotational degrees of freedoms of individual particles directly. Instead, the strong cohesion leads to the formation of clusters, the size of which presumably depends on the intrinsic energy scale governed by the formation of capillary bridges inside the wet granular sample. In order to understand the basic principle behind such kind of dynamical behaviour, we start with wet spherical particles in the lab. After a small amount of water is added into the glass beads, a closer view shown in Fig. 1.1 (b) clearly demonstrates the formation of capillary bridges between adjacent particles, which introduces cohesion in the wet granular sample. As an approximation, the cohesive force can be estimated by  $F_b = 2\pi R\sigma$ , where  $R$  and  $\sigma$  correspond to the radius of the sphere and surface tension of the wetting liquid respectively. For glass beads with  $R \approx 200 \mu\text{m}$ , comparable to typical sand grains on the beach, the capillary force is two orders of magnitude larger than the gravity of the particle, explaining why simply shaking the hand is not sufficient

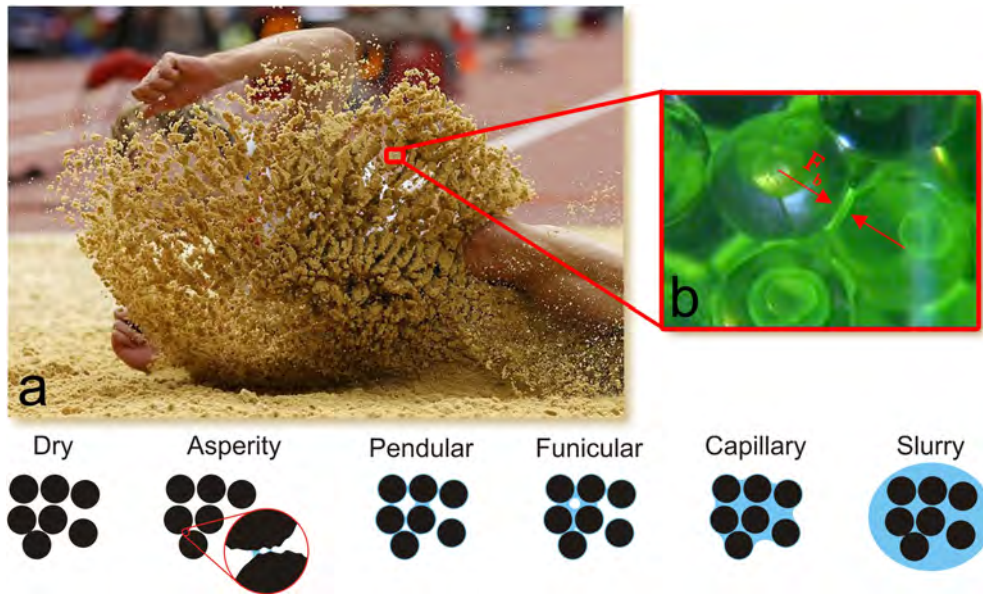


**Figure 1.1:** Upper panel: A daily life experience (a) of agitated wet granular matter taken during London Olympic Games in 2012 (Image courtesy of Wall Street Journal). The strong tendency for sand grains to form clusters can be attributed to the cohesion introduced by the wetting liquid, as the closer view (b) of water wetting glass beads indicates. Fluorescent dyes are added into the liquid to highlight the capillary bridges. Lower panel: Depending on the amount of wetting liquid added, various states of wet granular matter can be distinguished. See text for a more detailed definition.

to get rid of the sand grains sticking there after playing on the beach. A balance of the capillary force with the gravity suggests that the former dominates for particles with a radius up to 2 mm. Together with the rupture distance of the capillary bridge, the capillary force gives rise to a certain energy scale to overcome, in order for a granular particle to escape the attraction from its neighbours. As continuous energy injections are necessary to compensate such an energy dissipation, agitated wet granular matter can be treated as a non-equilibrium model system. More details of such force and energy scales will be discussed in Chap. 2.

Depending on the amount of wetting liquid added, wet granular matter can be classified into various states, as the lower panel of Fig. 1.1 shows. Dry corresponds to the case where cohesion is negligible, or say the inertia of the particles dominates. The asperity state is the slightly wetting situation where small capillary bridges between the asperities of adjacent particles that are in contact arise. The cohesive force in such a region depends on the length scale associated with the roughness of the sphere surface. The pendular state arises as the small liquid bridges at the asperity level merge into one single bridge. In such a state, the curvature of the spheres starts to play the main role in determining the cohesive force. Further increasing the amount of liquid added leads to the merging of capillary bridges into liquid clusters with voids, which is called a funicular state. As the voids inside are completely filled and the cohesion relies only on the curvature of the wet granular assembly, we speak of a capillary state. Finally, the slurry state means that all particles are immersed in the wetting liquid, and correspondingly no three phase contact lines exist any more. In

such a state, the cohesive force diminishes and the particles interact with each other through hydrodynamic interactions.

Strictly speaking there is no real dry granular matter in our daily life because of the influence from the environment, which may arise from the viscous drag force from the surrounding fluid, from the cohesion induced by the humidity, or from the electrostatic force due to charges. However, as long as the influence from the environment is sufficiently small compared with the inertia of the particles, the collective behaviour can be treated as dry granular phenomena. In order to characterize the relative importance, we can define dimensionless numbers similar to those in fluid mechanics. As an example, reminiscent to the Reynolds number, we define  $R_v = \rho_p R v / \mu$  for the inertia of particles with respect to the viscous drag force, where  $\rho_p$ ,  $v$ , and  $\mu$  are density, velocity of the particle, and the viscosity of the fluid correspondingly. For glass beads with a size of 1 mm moving in air,  $R_v \approx 10^4$  suggests a dry granular matter problem. If the same type of particles moving in water,  $R_v \approx 10$  suggests that the interactions with the surrounding liquid have to be taken into account. Similarly, the ratio between the gravity of particles and the cohesive force from the capillary bridges  $R_c \propto \frac{\rho_p R^2}{\sigma}$  will give us a guide on whether the cohesion should be considered or not. Note that the importance of the inertia of particles grows quadratically with the size of the spheres. Therefore, the smaller the particles, the more the influence from the humid environment should be considered.

Normally the asperity regime [Halsey & Levine, 1998] is not considered in the typical classification [Newitt & Conway-Jones, 1958; Iveson *et al.*, 2001; Mitarai & Nori, 2006] of wet granular matter because of its narrow range in the liquid content  $W$  scale. Here  $W$  is defined as the volume of the wetting liquid over the total volume that the wet granular sample occupies. Taking glass beads with a diameter of 1 mm as an example, the transition from the asperity to the pendular state occurs at  $W \approx 10^{-5}$ . Such a small threshold value clearly indicates the prominent role that humidity might play on the mechanical stability of sub-millimeter sized particles. Moreover, despite of the small threshold, enhanced rigidity has already been demonstrated to start well below the threshold for the pendular state to start [Huang *et al.*, 2009a], which will be described in more detail in the following Chap. 2.

The term wet granular matter throughout the following text represents the states with the presence of cohesion arising from wetting liquid added. Special focus will be given to the pendular state where mutual interactions between adjacent particles with a well defined energy scale dominate.

## 1.2 Motivation

The motivations for understanding the dynamics of wet granular matter are twofold: To shed light on the widespread applications due to its omnipresence, and to use it as a non-equilibrium model system.

Let's start with a discussion on the ubiquity of wet granular matter. In the center of Fig. 1.2, the sculpture mimicking the logo of Beijing Olympic Games 2008 is an example demonstrating the influence from the wetting liquid on the stability of sand. It is the dominating cohesive force present in a wide range of liquid content that makes wet sand a nice sculpturing material that attracts artists all over the world to meet

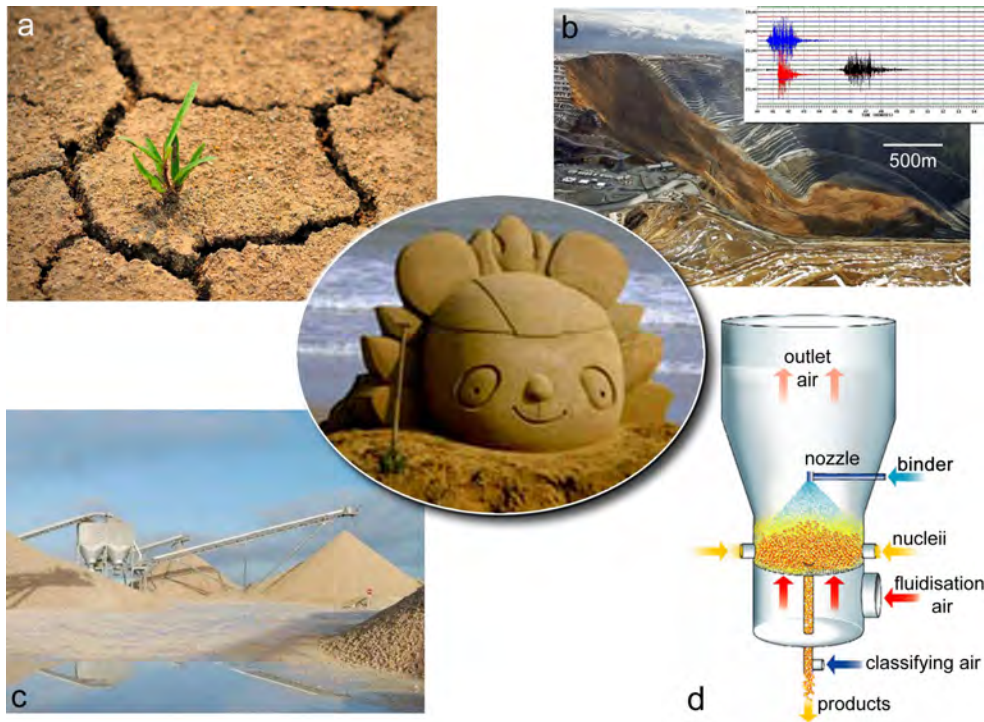


**Figure 1.2:** Understanding the dynamics of wet granular matter, such as wet sand used to build sand sculptures (center, photo courtesy of dfic.cn), is of importance in a large variety of industries including (a) agriculture, damage control of (b) natural disasters (Bingham Canyon mine landslide in 2013, image courtesy of American Geophysical Union), (c) civil engineering (image courtesy of European Aggregates Association), and (d) chemical engineering (image courtesy of Stefan Heinrich from Technical University of Hamburg Harburg).

regularly for competitions on building sand sculptures [SAND, 2014].

Perhaps examples more close to our daily life are from the kitchen. Preparing espresso as an example: It starts with grinding coffee beans into wet granulates in order to release the taste originally sealed inside, and follows with a filtration process of pumping compressed steam into the wet granulate. The efficiency of the initial grinding process, and the filtration process will influence dramatically the taste of the coffee.

Actually, not only coffee, but also many other foods found in the kitchen are in the form of granular matter. Because granular matter is typically not a good thermal conductor, adding a small amount of liquid, such as water used in cooking rice, or oil used in frying peas, is always necessary for cooking. Therefore, cooking, from a physical point of view, concerns very much on the heat transfer through wet granular matter.

Moreover, think about the plants where our daily foods are originally from. As shown in Fig. 1.2 (a), they are supported by soil, a type of wet granular matter concerned seriously in agriculture. How do the interactions between the roots of a plant with the surrounding soil take place, and in which way the wetting liquid inside helps in the nutrition transportation into the plants? To address those questions, a recent collaboration with Mathias Schröter and Ina Meier from Göttingen has been established to monitor the root growth of plants in an artificial soil, namely wet spherical particles, with the help of three dimensional computer tomography (CT). Because the emerging dynamics there corresponds to a different class, the outcome from this collaboration

is not included in the habilitation thesis.

At a larger length scale, natural disasters, such as avalanches, landslides, debris or mud flows, are also associated with the dynamics of wet granular matter, especially the transition from a solidlike to a fluidlike<sup>1</sup> state. The onset of such a transition, typically an abrupt event, is extremely important since these disasters may cause severe damage to our society. Taking the Bingham Canyon mine landslide (Fig. 1.2 b) occurred last year in Utah, USA, as an example, it is an extreme large event causing serious damages to the mining area. Luckily no one was injured in such a disaster because the deformation of the slope started weeks before and a continuous monitoring of the stress was able to give an alarm before the landslide happens. It is so huge that not only the local seismic recording station (inset of Fig. 1.2 b), but also the global seismic dataset located over 3000 km away in Columbia University, New York State, had a clear record on it and predicted a mass release of tens of millions of tons [AGU, 2013].

Thinking of the houses we are living in and of the Vitamin tablets we take, wet granular materials are as well widely concerned in the industries. Taking civil engineering as an example: The materials for construction are called aggregates, which are typically of mineral origin such as sand, gravel, and crushed rocks (Fig. 1.2 c). According to the UEPG (Union Européenne des Producteurs de Granulats, Europäischer Gesteinsverband, or European Aggregates Association) annual report in 2013, it is by far the largest non-energy extraction sector. Let the numbers speak: It is a sector processes roughly 3 billion tonnes a year of aggregates, composes of 15,000 companies at 26,000 quarries and pits across Europe, employs 238,000 people directly and indirectly. It is so huge a sector that its growth has a direct correlation to the GDP (Gross domestic product) [UEPG, 2013]. Last but not least, a substantial portion of products from chemical engineering, food and pharmaceutical industries is in the form of granular aggregates. One commonly used way to create such granulates is the so called granulation process. As sketched in Fig. 1.2 (d), liquid binders are used to glue functional powders fluidized by air flow together in such a process. The final size and strength of the granulates formed rely strongly on the balance between the energy scale of the capillary bridge, i.e. the binding energy, and the kinetic energy of particles during impacts. In a simplified view on such an event, considering the effective coefficient of restitution (COR) for wet impacts, binding or breaking corresponds to 0 or a finite COR. A thorough understanding on the impact at a ‘microscopic’ level, as will be discussed in Chap. 2, is essential in modelling not only the granulation process, but also other industrial processes such as extraction, dredging, crushing, grinding, separation, sifting, washing, desliming, mixing, packing, storage and transport. Again, concerning the impact on our society, let numbers speak: Processing 1 ton of granular materials has an energy cost of about 10 kWh with 10 kg of Carbon Dioxide (CO<sub>2</sub>) produced [UEPG, 2013]. In USA, roughly 1.3% of total energy produced across the country is used in grinding granular materials [Duran, 2000].

From a physical point of view, the energy dissipation through the frequent collisions between particles or rupturing of liquid bridges attributes agitated wet granular matter as a model system far from thermodynamic equilibrium. Upon energy injection, such a non-equilibrium system may behave like a solid, a liquid or a gas. As will be dis-

---

<sup>1</sup>Note that the term fluid is used as a synonym for liquid throughout the thesis, although strictly speaking fluid includes both liquid and gas phases.

cussed in detail in Chap. 3, critical phenomena such as phase transitions and pattern formation found in experiments can be discussed in connection to those observed in equilibrium systems, and compared with large scale molecular dynamics (MD) simulations. This fact gives us a chance of using such a model system to characterize the non-equilibrium steady state (NESS) arising from the balance between the energy injection and dissipation. Such characterizations will not only provide guidelines for the widespread applications of wet granular matter, but also shed light on a continuum description of non-equilibrium systems in general.

### 1.3 A brief historical review

Due to its ubiquity, granular matter is always acting as one of the essential components in different philosophies and world views across various cultures. As an example, the stamp named ‘Erde’ shown in Fig. 1.3 uses sand to represent earth, one of the four basic elements that the world is composed of. Again due to its ubiquity, our awareness of granular dynamics started to develop thousands of years ago, probably even earlier than the word to describe such a material was invented. Taking the pictographic Chinese language as an example, the word ‘sand’ in one of its ancient form, as overlaid in Fig. 1.3, gives us a clue on how ancient people imagine such a material: A composition of small dots that mimic sand grains at a ‘microscopic’ level, together with curved lines that represent the ripples formed by the ‘macroscopic’ collective motion of sand grains. It is among the first few hundreds words invented at the early stage of Chinese language evolution roughly 3400 years ago.

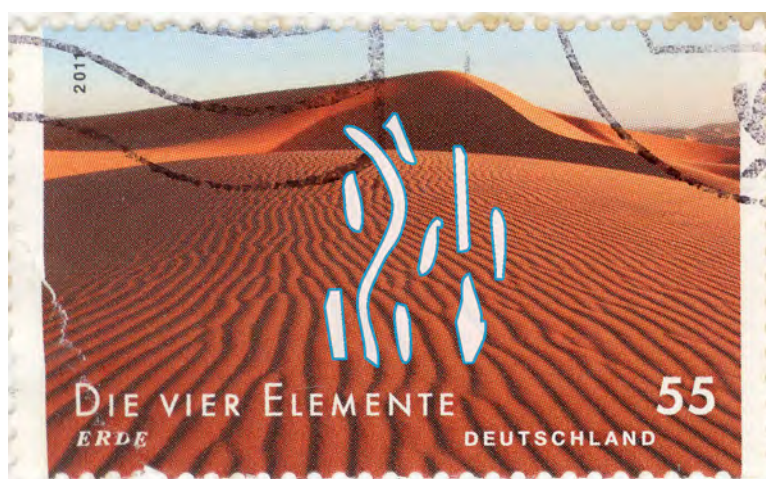


**Figure 1.3:** In the stamp series ‘The four elements’, a picture of sand dunes with ripples is used to represent earth (image courtesy of Deutsche Post). The overlaid character is the calligraphy of the word ‘sand’ in Chinese bronze inscriptions.

Learning is always a refining process, and this is also true for granular matter. The aforementioned awareness of granular materials, as well as the view of flowing poppy seeds from Lucretius [Carus & Leonard, 2004] sets the starting point of our understanding on such a material. Such an understanding evolves with time, mostly driven

by real life applications. It was the needs to build better forts that Coulomb coined the frictional law [Coulomb, 1773]; it was intrigued by the problem of packing more cannon balls on the decks of warships that Kepler's conjecture was proposed [Hales, 2005]; and it was for visualizing the performance of musical instruments that Chladni figures were discovered [Chladni, 1787]. Those are only few out of many other examples (See e.g. Newton [1687]; Faraday [1831]; Hertz [1882]; Reynolds [1885]; Janssen [1895]) on how granular materials are understood from specific perspectives. In the 20th century, driven by the industrialization process, investigations on granular materials experienced a boost and had consequently been split into various fields, such as earth scientists focusing on dynamics of marine sand, desert sand and dune migrations [Fredsoe & Deigaard, 1992; Pye, 2009; Goudie, 2013], engineers more orientated to the process of such a material [Litster *et al.*, 2004; Rumpf, 1962; Stronge, 2004], civil engineers focusing on soil mechanics [Das, 1997; Schofield & Wroth, 1968].

Despite of the advances on various applications, a unified physical view on the dynamics of granular matter, especially wet granular matter, is still lacking. Proper definitions of various NESS, and the physical quantities to describe them are still under debate. At the current stage, one typical approach driven by applications is to treat granular materials as a continuum medium and use fluid mechanics to describe its dynamical behaviour. This approach will unavoidably encounter the problem when granular matter undergoes phase transitions, e.g. a transition from a liquidlike to a solidlike state. The other approach uses discrete element method (DEM) to calculate the mobilities of individual particles based on certain force laws, in order to predict the large scale collective behaviour with computer simulations. However, describing wet, or even dry impacts at the particle level is typically a complicated story. Assumptions have to be made for large scale simulations of granular matter to be possible [Yu *et al.*, 2013], and contributions to applications with such modelling normally requires a try and trial process. Taking the granulation process as an example, it is not until very recently that useful predictions can be made [Iveson *et al.*, 2001].

In order to have a deeper understanding on granular dynamics, more and more interest has been generated in the past decades from the physical community. In the 1980s, triggered by the discovery of self-organized criticality (SOC) [Bak *et al.*, 1987; Jensen, 1998; Bak, 1999], equipped with the rapidly advancing computer simulation and imaging techniques, a series of investigations have been performed to find the essential ingredients that determine the dynamics of granular materials, such as the avalanches of a sand pile [Jaeger *et al.*, 1989; Held *et al.*, 1990; Frette *et al.*, 1996]. As will be discussed in Chap. 3, it turns out that granular dynamics contains interesting topics itself that are often counter-intuitive and far from understood. Driven by curiosity, physicists tried to find essential components that dominate granular dynamics. After more than one decade's investigations, a few review articles [Guyon *et al.*, 1990; Nagel, 1992; Jaeger *et al.*, 1996; de Gennes, 1999; Goldhirsch, 2003; Aranson & Tsimring, 2006] and introductory books [Duran, 2000; Ristow, 2000; Brilliantov & Pöschel, 2004; Mehta, 2007; Aranson & Tsimring, 2009] were published. In the past decade, more and more interest has been drawn to the physics of wet granular matter. Advances and open questions in such an emerging field have been summarized in recent reviews [Mitarai & Nori, 2006; Herminghaus, 2005, 2013].

As a summary of the knowledge learned from the experimental investigations on wet granular matter, the chapters in the thesis are organized as the following: Chap-

---

ter 2 is largely devoted to the ‘microscopic’ particle-particle interactions that determine the intrinsic time, length and energy scales in wet granular matter, including impact mechanics of a spherical particle bouncing on a flat surface covered with a liquid layer, an analysis on the energy dissipation associated with the impact, and a tentative model for simulations. Chapter 3 contains various collective behaviour of wet granular matter, agitated either vertically or horizontally via shaking, swirling or shearing. The focuses will be given to the phase transitions and pattern formation in monolayer as well as multiple-layer systems. Comparisons to dry granular dynamics, as well as the influence from the shape of particles will also be presented briefly. In Chapter 4, possible connections between the ‘macroscopic’ behaviour and ‘microscopic’ particle-particle interactions will be drawn as a conclusion. Finally, an outlook with open questions toward a deeper understanding of such a material will be given.



## 'Microscopic' interactions

The universe is viewed as agglomerations of particles. These particles may be point like (0 dimension) as in astrophysics and quantum electromechanics; may be string like (1 dimension) as in string theory [Becker *et al.*, 2006]; may be grains of sand (3 dimensions) that granular matter is composed of.

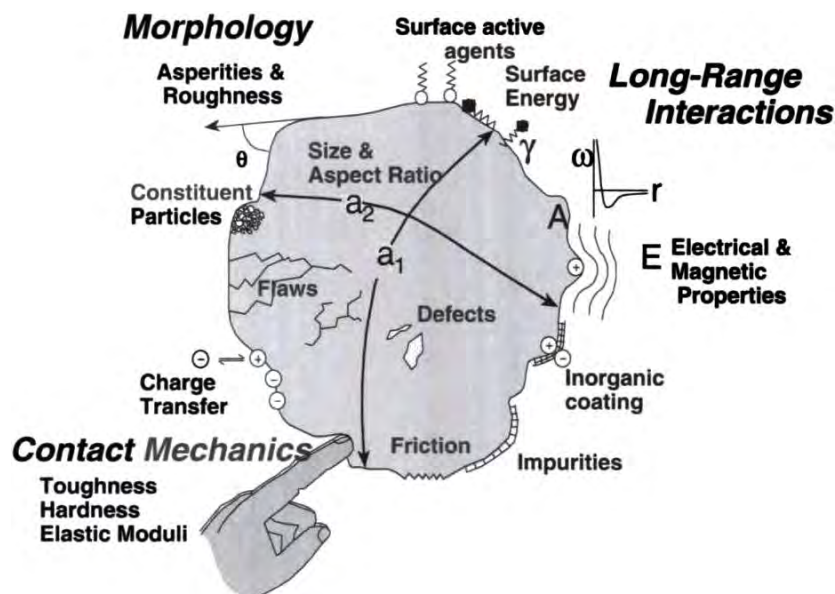


**Figure 2.1:** A view on a granular particle taken from an engineering text book [Litster *et al.*, 2004], with a list of factors that may influence the dynamics of the particle.

The dynamics of a single granular particle can be described fully by classical mechanics, which seems to be ‘simple’. However, a closer view on such a particle reveals its complexity: As the sketch from an engineering textbook shows in Fig. 2.1, there exist a vast number of possible ingredients to be considered, including material properties (e.g. elastic modulus and hardness), geometric aspects (e.g. particle size and shape), surface properties (e.g. roughness, charges, wettability and impurities), as well as internal defects. All those properties will affect the force and energy scales associated with the particle-particle and particle-environment interactions. A proper characterization of those quantities is actually becoming the heart of modern particle processing technologies [Litster *et al.*, 2004], as the treasured advice given by Roland Clift in the 1st international particle processing forum states:

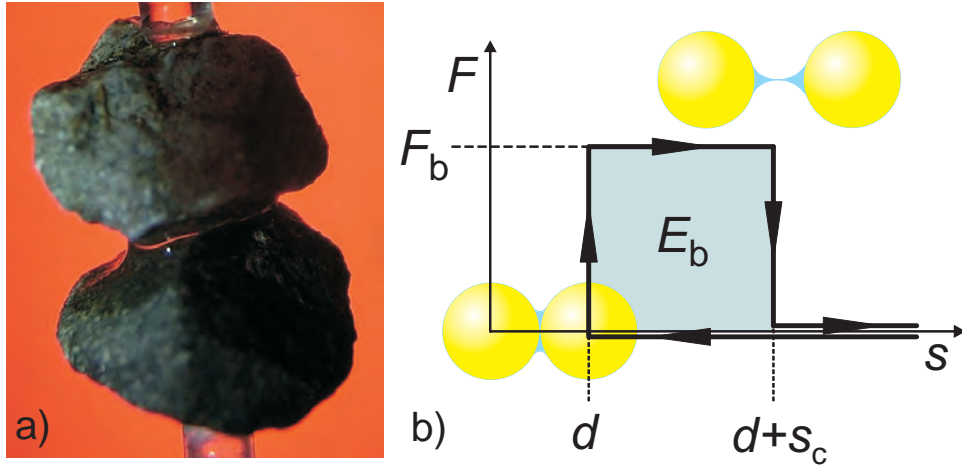


**Figure 2.2:** a) A snapshot of two grains connected with each other via a capillary bridge, which introduces a cohesive force  $F_b$  between them. The scale bar corresponds to 1 mm. b) The minimal capillary model [Fingerle *et al.*, 2008] used to describe the interactions between two wet grains, which considers spherical particles with the same diameter  $d$ , constant capillary force  $F_b$ , and a rupture distance  $s_c$  of the capillary bridge formed. The sketches on the bottom-left and upper-right corners illustrate the configurations of the wet spheres with separation distance  $s = 0$  and  $s_c$  correspondingly.

“Measure properties, don’t perform rituals.”

However, even if we have a proper definition for each of those properties and are able to measure them accurately, are we able to predict the ‘macroscopic’ behaviour, such as when, where, and how strongly a landslide occurs? That is difficult because a general framework that accounts for the collective behaviour of granular matter, in which those measured quantities can be plugged in, is still lacking. As an example, it is not until very recent that a two dimensional continuum model for sheared dense granular flow is proposed [Jop *et al.*, 2006]. And its validity under various conditions is still to be justified. It is more complex for the case of wet granular matter, owing to the additional influence from the wetting liquid. As the snapshot of two wet grains shown Fig. 2.2 (a) indicates, the cohesive force  $F_b$  arising from the formation of liquid bridge relies, in addition to the aforementioned particle properties, on the local geometry of the gap as well as liquid properties.

From a physical perspective, it is essential to sort out the key components that dominate the collective behaviour, so as to develop simplified descriptions of granular dynamics for more efficient computer simulations targeting at real life applications. Fig. 2.2 (b) shows one of such simplifications on wet granular matter: It treats grains as spherical particles, and models the mutual interactions between two wet spheres with a hysteresis loop that contains a length  $s_c$  and an energy scale  $E_{cb}$  that arise from the rupture distance and energy of a capillary bridge. The detailed nature of the binding and the rupture of capillary bridges and interactions between various liquid bridges are ignored. Such kind of *minimal model* can be conveniently implemented into computer simulations, and comparisons to corresponding experiments reveal that it describes phase transitions of agitated wet granular particles qualitatively well [Fin-

gerle *et al.*, 2008]. Moreover, a modification of the force laws applied yields almost identical phase diagrams, suggesting the detailed nature of the rupture event does not play an important role in determining the transition from a liquilike to a gaslike state of vertically agitated wet granular matter, as will be discussed further in Sec. 3.4.3. The essential quantity here is the rupture energy that characterizes the dominating energy dissipation inside the granulates. As a system driven far from thermodynamic equilibrium, it is the balance between such energy dissipation and injection that determines the non-equilibrium steady state.

This chapter is devoted to the characterizations of particle-particle interactions for dry 2.1 and wet 2.2 cases. Special focus will be given to the coefficient of restitution, which quantifies the energy dissipation associated. Finally, preliminary investigations on the contact angle hysteresis will be presented in Section 2.4.

## 2.1 Dry impact

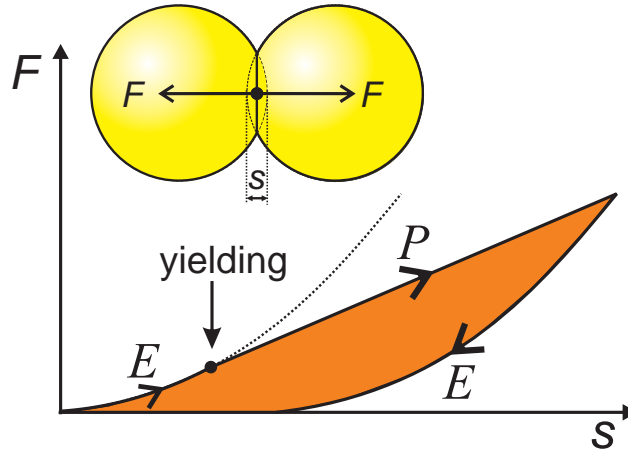


**Figure 2.3:** Contact force  $F$  between two spheres as a function of the penetration depth  $s$ .  $E$  and  $P$  stand for elastic and plastic deformation regions correspondingly. The dash line is an extension of the elastic deformation curve below yielding, following the Hertz contact law. Inset is a sketch of two spheres in contact.

Before we discuss the energy dissipation, let's start with the elastic interaction between two spherical particles, also named as Hertz's problem. In his paper 'On the contact of elastic solids' ('Über die Berührung fester elastischer Körper') published in 1882 [Hertz, 1882], he showed that, within the elastic limit, the contact force between two spheres (inset of Fig. 2.3) is related to the penetration depth  $s$  by

$$F_{\text{el}} = k \cdot s^{3/2}, \quad (2.1)$$

where the elastic constant  $k \propto Y\sqrt{R}/(1-\nu^2)$  depends on the effective radius  $R$ , Young's modulus  $Y$ , and Poisson's ratio  $\nu$  of the particles. Suppose two particles of identical size collide with each other elastically, i.e. no energy dissipation, the above relation can be used to estimate the maximum penetration depth and the duration of the collision. Suppose the mass of the sphere is  $m$  and the initial relative velocity is  $v$ , energy conservation leads to

$$\frac{1}{2}mv^2 - \frac{1}{2}m\left(\frac{ds}{dt}\right)^2 = \frac{1}{2}k \cdot s^{5/2}. \quad (2.2)$$

As all the initial kinetic energy is turned into the potential energy, the maximum penetration depth

$$s_{\max} = \left(\frac{m}{k}\right)^{2/5} \cdot v^{4/5} \quad (2.3)$$

is reached. The duration for the collision can be estimated by [Duran, 2000]

$$\tau = 2 \int_0^{s_{\max}} \frac{ds}{\sqrt{v^2 - ks^{5/2}/m}} \approx 2.94 \left(\frac{m^2}{k^2v}\right)^{1/5}. \quad (2.4)$$

At the end of his paper, Hertz took the collision of two steel balls with a size of the earth as an example:

For two steel spheres with the size of the earth, a collision with initial velocity of  $10 \frac{\text{mm}}{\text{s}}$  takes about 27 hours.

“Für zwei Stahlkugeln von der Grösse der Erde, die mit einer Anfangsgeschwindigkeit von  $10 \frac{\text{mm}}{\text{s}}$  zusammenträfen, würde die Dauer der Berührung nahe an 27 Stunden betragen.”

The extremely long time predicted for this example arises from the large size and small relative velocity. In reality, two 1.5 mm spheres colliding with velocity 5 cm/s will lead to  $s_{\max} = 0.2 \mu\text{m}$  and  $\tau = 11.7 \mu\text{s}$ . In comparison to the sound speed in Aluminium, this duration is sufficient for an elastic wave to travel back and forth inside the sphere for  $\approx 20$  times.

For pure Aluminium, the yield stress  $\sigma_Y \approx 9 \text{ MPa}$  leads to an elastic-plastic transition at a strain of  $\sigma_Y/Y \approx 1.30 \cdot 10^{-4}$ . Note that this is already slightly smaller than the strain caused by the impact  $s_{\max}/2R \approx 1.33 \cdot 10^{-4}$ . This comparison suggests that the elastic limit could be easily surpassed in most impacts we are dealing with. In another word, energy dissipation has to be considered in real life applications.

One convenient approach to characterize the energy dissipation is to measure the coefficient of restitution (COR), the ratio between relative rebound and impact velocity of two colliding particles. This definition was introduced by Newton in his famous book ‘The mathematical principles of natural philosophy’ [Newton, 1687]. There he described an inelastic impact as the following:

“... In bodies imperfectly elastic the velocity of the return is to be diminished together with the elastic force ... and makes the bodies to return one from the other with a relative velocity, which is in a *given ratio* to that relative velocity with which they met ... ”

Using a device with a similar construction to the Newton’s pendulum (Fig. 2.4), he performed impact experiments to measure the COR of various types of particles, and used the results to demonstrate the validity of the third law of motion:

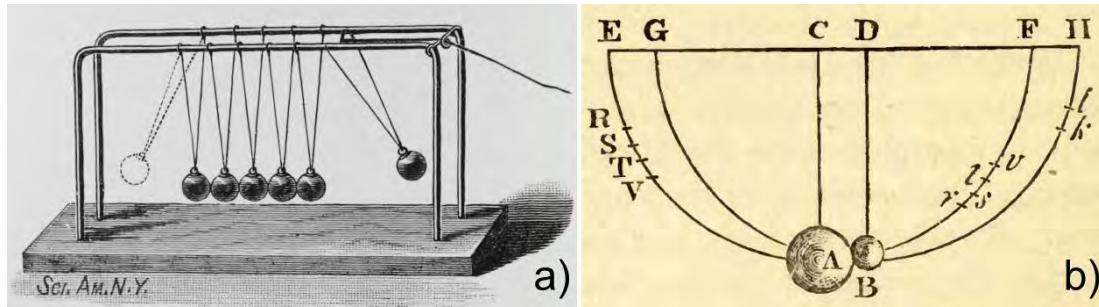


**Figure 2.4:** A snapshot of Newton’s cradle (a) and a sketch of the experimental set-up used to measure the coefficient of restitution (COR) by I. Newton [Newton, 1687].

“ ... This I tried in balls of wool, made up tightly, and strongly compressed. For, first, by letting go the pendulous bodies, and measuring their reflexion, I determined the quantity of their elastic force; and then, according to this force, estimated the reflexions that ought to happen in other cases of congress. And with this computation other experiments made afterwards did accordingly agree; the balls always receding one from the other with a relative velocity, which was to the relative velocity with which they met as about 5 to 9. Balls of steel returned with almost the same velocity: those of cork with a velocity something less; but in balls of glass the proportion was as about 15 to 16. And thus the third Law, so far as it regards percussions and reflexions, is proved by a theory exactly agreeing with experience.”

Those measurements are actually quite accurate in comparison to nowadays experiments with high speed photography. Taking the case of glass particles as an example, the error is within 0.03, demonstrating that the COR is indeed a good parameter to characterize binary impacts. However, this assumption that the COR is a material dependent property is known nowadays to be incorrect: More accurate and systematic experiments have demonstrated that the COR depends on the impact velocity, the size, shape, and even the preparation protocol of the particles [Stronge, 2004]. In principle, any factor listed in the above Fig. 2.1 may affect the COR to some extent. Concerning the modelling of granular dynamics, the dependency of COR on the impact velocity  $v_i$  is of great importance, since the other properties of agitated particles don’t change as much as  $v_i$ .

To account for the energy dissipation, we have to speculate possible mechanisms and test their relative importance. Those mechanisms may include plastic or viscoelastic deformations, impact generated body and surface acoustic waves that dissipate into heat through internal frictions, crack formation, capillary interactions with the presence of wetting liquid, sliding frictional forces, etc.

One frequently adopted model for dry impacts is to assume plastic deformation above yielding. Figure 2.3 shows a sketch of the simplest case of a plastic force growing linearly with penetration depth  $s$ , in contrast to the Hertz’s law  $\propto s^{3/2}$  shown as the dash line. Such a combination leads to an offset compared with the unloading process, which is assumed to be elastic. The shaded region indicates the loss of energy through the loading-unloading process, owing to such a plastic deformation [Thornton, 1997].

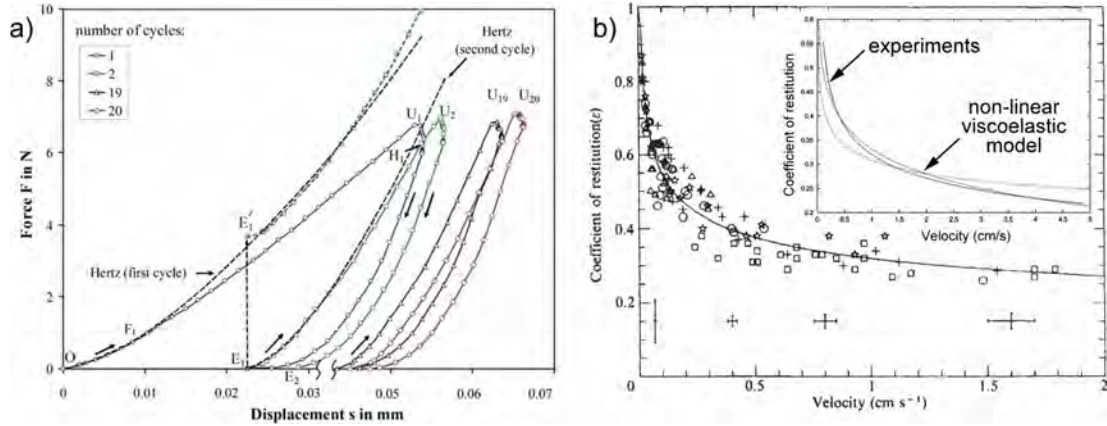


**Figure 2.5:** a) Force displacement curves of a granular particle under cyclic loading and unloading [Antonyuk *et al.*, 2010] b) Normal coefficient of restitution of ice particles as a function of the impact velocity [Bridges *et al.*, 1984]. Inset shows a comparison between the fitted curve from the data shown in the main panel and a model [Brilliantov *et al.*, 1996].

In the past decades, a substantial amount of work has been devoted to a proper description of the force law governing the impact, leading to a handful of different models. Based on the pathways taken towards energy dissipation, they can be classified into viscoelastic or perfectly plastic cases, linear or nonlinear cases, and combinations in between. For more detailed information of various models, the reader may refer to a recent review [Antonyuk *et al.*, 2010].

As indicated in Fig. 2.3, plastic deformations are not fully recoverable. As a consequence, permanent deformations of the particles arise during each impact, which immediately lead to the question of how reproducible the COR obtained is. Indeed, the amount of energy dissipated has been found to depend on the runs of experiments, or history of the particle under investigations. The force-displacement curves of a spherical particle under cyclic loading-unloading shown in Fig. 2.5 (a) demonstrate such a feature: Deviation from elastic deformation occurs for each loading period, leading to a hysteresis loop that characterizes the energy dissipation associated with the loading-unloading cycle. The loop shifts to higher  $s$  value with the cyclic number and with a reduced loop area, indicating that the particles become more and more elastic upon impacts. Despite of the shift with the number of impacts, the area within the loop, i.e. energy dissipated, tends to saturate to a certain value, suggesting that reproducible COR can still be obtained after sufficient number of initial impacts for plastically deforming particles.

Beside plastic deformations, models assuming viscoelastic deformations consider the dissipation of energy through effective viscous damping during impact, which will recover completely after rebound. Therefore no permanent deformation is allowed. It is claimed that such kind of modelling has a better consistency with the assumption of spherical particles in comparison to the plastic model [Brilliantov & Pöschel, 2004]. More specifically, in addition to elastic force proposed by Hertz, such type of models consider a viscous term that determines the energy dissipation:

$$F_v = \frac{3}{2} Ak\sqrt{s}\dot{s}, \quad (2.5)$$

where  $s$  is the penetration depth and  $k$  is the elastic constant (see Eq. 2.1).

$$A = \frac{(3\eta_2 - \eta_1)^2}{3(3\eta_2 + 2\eta_1)} \cdot \frac{(1 - \nu^2)(1 - 2\nu)}{Y\nu^2} \quad (2.6)$$

is a dissipative factor arising from material properties [Brilliantov & Pöschel, 2004; Brilliantov *et al.*, 1996], where  $\eta_1$  and  $\eta_2$  are viscous coefficient from the dissipative stress tensor.

Taking  $F_{\text{el}}$  and  $F_v$  as the only forces acting on the sphere, one can write the equation of motion and derive the coefficient of restitution for a normal impact [Brilliantov & Pöschel, 2004]:

$$e_n = 1 - C_1 A \kappa^{2/5} v_i^{1/5} + C_2 A^2 \kappa^{4/5} v_i^{2/5} \mp \dots, \quad (2.7)$$

where  $\kappa = k/m_{\text{eff}}$  with  $m_{\text{eff}}$  the effective mass of the particle, and  $C_1, C_2, \dots$  are pure numbers. Taking a first order approximation, it predicts a decay of the COR with  $v_i$ . This is reasonable considering the scaling of the damping term with  $v_i$ : A larger initial velocity leads to a larger energy dissipation from viscosity, i.e. a smaller COR. Such a model has been successfully used to explain the  $v_i$  dependence of the COR for ice particles, in order to shed light on the formation of the Saturn's rings from a 'microscopic' perspective, as shown in Fig. 2.5 (b) [Bridges *et al.*, 1984; Brilliantov *et al.*, 1996].

In a more recent work [Weir & Tallon, 2005], the energy loss due to elastic wave generation is also found to play an important role in determining the COR. Within such type of energy loss, roughly 67% turned into the surface acoustic (Rayleigh) waves, 7% into pressure (P) waves and 26% into shear (S) waves. Moreover, a dimensionless number,  $v_i/c$  with  $c$  the speed of sound, is argued to be a key parameter determining such types of energy loss.

To summarize: Despite of the advances over past centuries, impacts between particles, even without considering the influence from the environment, are still not completely understood. A proper classification of the associated energy dissipation mechanisms, and a search for the essential parameters dominating the process still have a long way to go. Nevertheless, motivated by the vast number of applications in various industries, as described in Chap. 1, a consideration of the humid environment is essential and has been a topic of interest over the past decades. Thus we focus on the impacts of wet particles in the following section.

## 2.2 Wet impact

As the experience of playing basketball in the rain tells, wet impacts cost more energy than the dry ones, owing to the additional energy taken from the wetting liquid covering the ground. A closer look at this process, shown in Fig. 2.6, reveals rich dynamical behaviour of the wetting liquid during the impact, such as the formation of liquid bridges, surface waves, cavitation, singularity upon the rupture of liquid bridges [Eggers, 1997], as well as satellite droplets formation. Those droplets may bounce or coalesce partially with the liquid film, leading to a cascade of daughter droplets [Thoroddsen & Takehara, 2000; Thoroddsen, 2006]. First reported by Rayleigh [1899], the dynamics of the bouncing droplets can be attributed to the interplay between the time scale for the impact

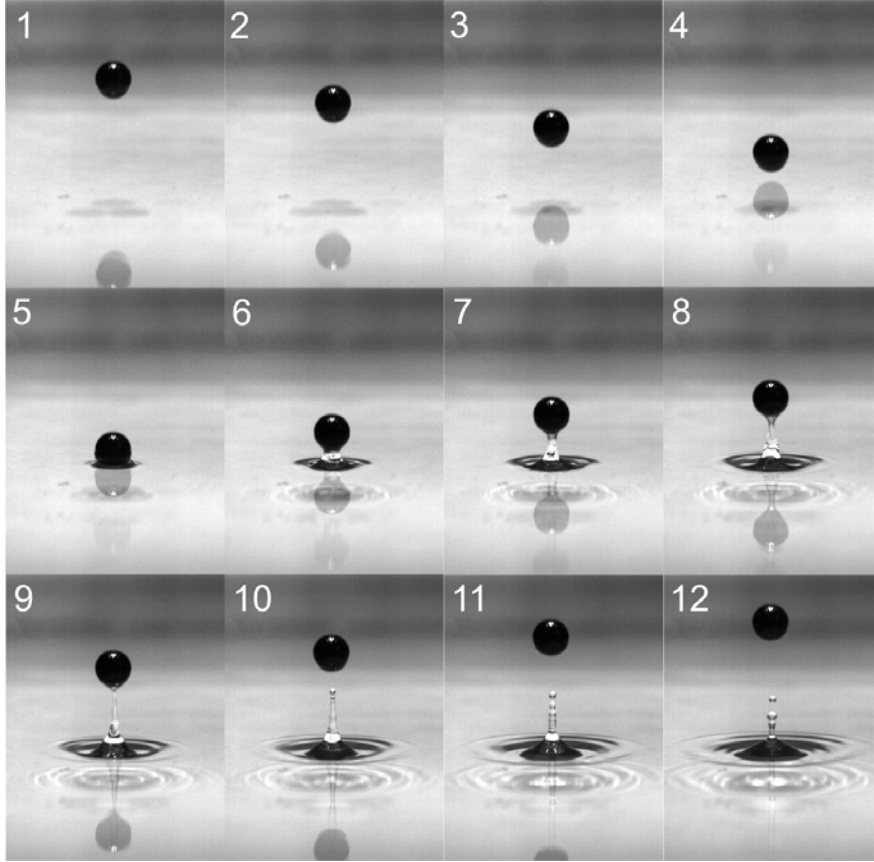


**Figure 2.6:** A series of snapshots showing a wet spherical glass bead bouncing on a glass plate covered with a 1 mm thick water film. [R4: Gollwitzer *et al.*, 2012]

and that for the air to flow out of the gap, leading to the possibility to avoid coalescence completely by introducing oscillations to the bulk liquid [Couder *et al.*, 2005].

Since the energy required for such rich dynamics of the droplets arises from the kinetic energy of the bouncing particle, it is counted as the energy loss that influences the COR. Moreover, direct inspections indicate that the influence from surface tension could also play a role, owing to the formation and rupture of liquid bridges. No need to mention the viscous effect, which can be extremely large as the liquid film is compressed during the impact. According to the lubrication theory, the viscous drag force diverges as the liquid film is sufficiently thin. Depending on the time scale of impact and that for the liquid to be squeezed out, recent investigations predict that glass transition of the liquid has to be considered in modelling the impact of wet particles [Donahue *et al.*, 2010*b*, 2012].

Before go to the details of various energy dissipation mechanisms, it is helpful to have an overview of the main components and a characterization of their relative importance. As shown in Fig. 2.7, inertia, surface tension and viscosity are considered to be the main energy dissipation sources. Depending on the liquid and particle properties, one or another factor will dominate. In order to judge the relative importance of the three factors, capillary number  $Ca \equiv \mu v / \sigma$ , Reynolds number  $Re \equiv \rho_1 v R / \mu$ , and bond number  $Bo \equiv Re \cdot Ca = \rho_1 v^2 R / \sigma$  are used, where  $\rho_1$  represents the density of the

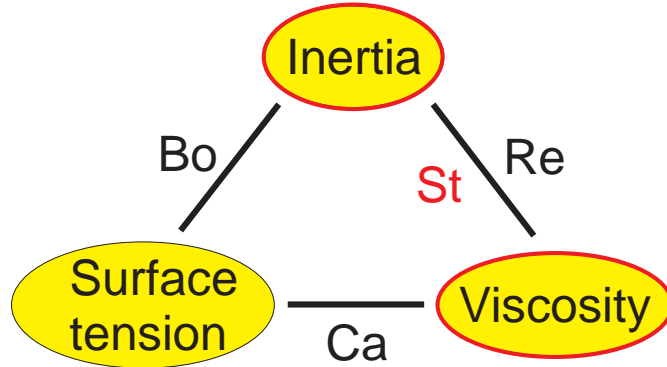


**Figure 2.7:** Possible liquid properties that influence the energy loss of a wet impact. The associated dimensionless numbers can be used to distinguish the dominating factors.

liquid. On the limit of viscosity dominating, the elastohydrodynamic theory developed by Davis *et al.* [1986] have been successfully employed to describe the COR [Barnocky & Davis, 1988; Davis *et al.*, 2002; Donahue *et al.*, 2010a] for normal as well as oblique impacts. It considers the coupling between the elastic deformation of spheres and the hydrodynamics of the liquid film in the low Reynolds number ( $Re$ ) regime where lubrication theory applies. It turns out that the impact dynamics can be characterized with the dimensionless Stokes number that measures the inertia of the particles with respect to the viscous force:

$$St \equiv \frac{mv}{6\pi\mu R^2} = \frac{2\rho_p Rv}{9\mu}, \quad (2.8)$$

where  $m$  and  $\rho_p$  represent the mass and density of the sphere.

In most daily life experiences or industrial applications, such as the one shown in Fig. 2.6, the precondition for the elastohydrodynamic theory is violated. This is due to the strong inertia effect, as judged by the relatively high  $Re$ . Therefore, it is essential to figure out the important factors, and search for additional dimensionless numbers to be considered, and eventually discuss the scalings of the COR with those parameters. In short, the central task is to have a simplified model that is capable of capturing the essential physical mechanisms, and adaptable to large scale computer simulations. As a first step toward such a goal, we analyse the three possible factors shown in Fig. 2.7 in the following subsections.

### 2.2.1 Influence from surface tension

Due to surface tension, a liquid surface has the tendency to minimize its area. For example, emulsion droplets will have a spherical shape. For a more complicated geometry such as at the pore level of a porous media, or between grains in a granular medium, a determination of the shape of the embedded liquid is not so straightforward. Taking the simplest geometry of a gap between two equally sized spheres as a starting point, the liquid bridge formed there can be approximated to have a toroidal shape, which gives rise to two curvatures: The radius of curvature of the bridge profile in the meridional plane  $r_1$  and the neck radius  $r_2$  (see the inset of Fig. 2.8 for a sketch).

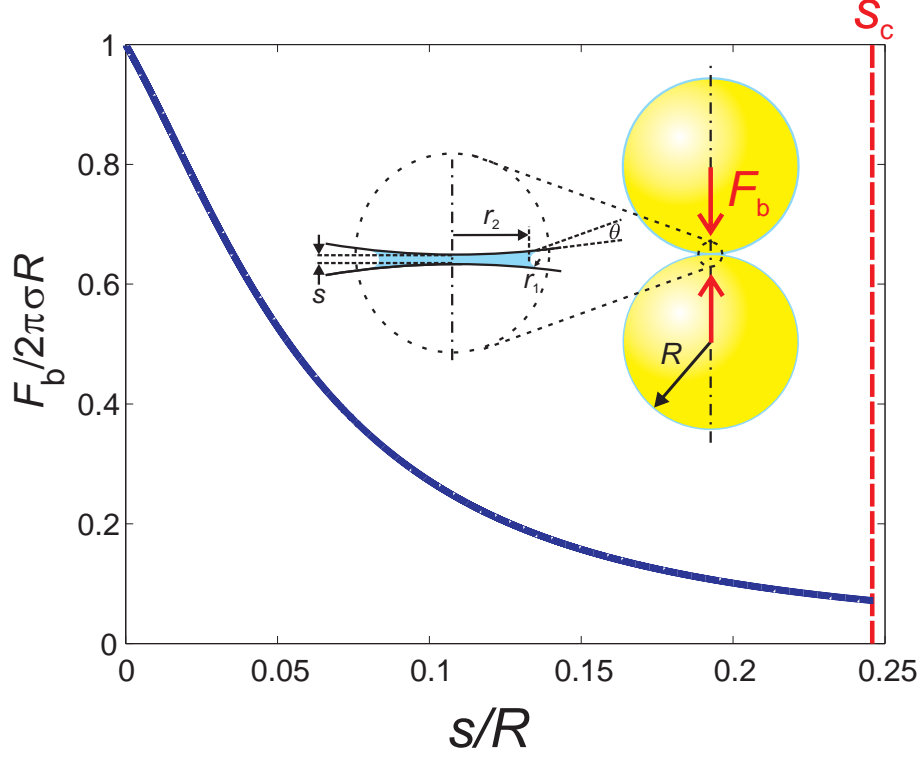


**Figure 2.8:** Capillary force induced by the liquid bridge formed between two spheres, as sketched in the inset, as a function of the separation distance, see text for details.

Hence, the pressure difference across the air-liquid interface, i.e. the Laplace pressure, can be estimated with the Young-Laplace equation,

$$\Delta p = \sigma \left( \frac{1}{r_1} + \frac{1}{r_2} \right). \quad (2.9)$$

Further assuming that the cohesive force is determined by the curvatures at the neck, and ignoring the influence from gravity, i.e. considering the size of bridges smaller than the capillary length  $l_c = \sqrt{\sigma/\rho_l g}$  with  $g$  the gravitational acceleration, the capillary force between two spherical particles can be estimated with

$$F_b = 2\pi r_2 \sigma - \pi r_2^2 \Delta p, \quad (2.10)$$

where the first term corresponds to the line tension acting on the perimeter of the neck, and second term, typically dominating, arises from the pressure difference on the cross section of the neck. Such assumptions can be extended to liquid bridges between various shaped surfaces, such as sphere-plane, plane-cone, or cone-cone surfaces (see e.g. Butt & Kappl [2009] for a recent review).

On the limit of bridge volume  $V_b \rightarrow 0$ , i.e.  $r_1 \ll r_2 \ll R$ , and for the case of close contact  $s = 0$ , Eq. 2.10 can be further simplified [Herminghaus, 2005] into <sup>1</sup>

<sup>1</sup>For such a limiting case, the second term in Eq. 2.10 dominates, and the Pythagorean theory  $R^2 + (r_1 + r_2)^2 = (R + r_1)^2$  leads to the relation  $r_2^2 \approx 2Rr_1$ .

$$F_b = 2\pi r_2 \sigma - \pi r_2^2 \Delta p \approx 2\pi R \sigma \cos \theta \quad (2.11)$$

with  $\theta$  the contact angle. Note that the particle size is the only length scale left in this simplification, thus it provides a convenient estimation on the cohesive force.

As the distance between the spheres varies, a numerical solution for  $F_b$  as a function of  $s$  with fixed  $\Delta p$  shows a monotonic decay of  $F_b$  until the capillary bridge ruptures. This agrees well with experiments done on the quasi-static limit [Willett *et al.*, 2000]. Based on such an agreement, a close form relation was introduced to estimate the capillary force between two equal sized spheres

$$F_b = \frac{2\pi\sigma R \cos \theta}{1 + 2.1s_r + 10.0s_r^2}, \quad (2.12)$$

where  $s_r \equiv \frac{s}{2} \cdot \sqrt{R/V_b}$  is the rescaled half-separation distance with  $V_b$  the volume of the capillary bridge. Additionally, the rescaled rupture distance can be estimated analytically with

$$s_c = \left(1 + \frac{\theta}{2}\right) \cdot \left(\frac{V_b^{\frac{1}{3}}}{R} + \frac{V_b^{\frac{2}{3}}}{10R^2}\right). \quad (2.13)$$

It suggests that, as a first order approximation, one can estimate the rupture distance simply from the cubic root of the bridge volume  $V_b^{\frac{1}{3}}$  for the case of complete wetting.

Figure 2.8 presents an estimation of the capillary force, rescaled to its maximum value (Eq. 2.11), as a function of the rescaled separation distance  $s/R$ . It corresponds to the case of a water bridge between two equal sized glass spheres with a radius of 1 mm, and a liquid content  $W = 1\%$ . The liquid content is related to the bridge volume through  $V_b = \frac{8\pi W}{3\phi N} \cdot R^3$  with  $N$  the coordination number and  $\phi$  the packing fraction. The capillary force decays monotonically with the separation distance until the rescaled rupture distance  $s_c$  is reached.

Careful comparisons to the experiments [Willett *et al.*, 2000] reveal that the error for such an estimation grows with  $V_b$ . For a rescaled volume  $V_b^{\frac{1}{3}}/R \approx 0.001$ , or correspondingly a half opening angle of  $\beta \approx 10^\circ$  (see Fig. 2.9 a for a definition), the above estimation is accurate within 4%. A more accurate analytical estimation for  $V_b^{\frac{1}{3}}/R$  up to 0.1, covering almost the whole pendular state, is also provided in the same reference as an appendix.

In Eq. 2.10, the two dominating curvatures,  $r_1$  and  $r_2$ , are not independent from each other and also not easily accessible in experiments. Thus, we try to represent the Laplace pressure with respect to the separation distance  $s$  and the half opening angle  $\beta$  of the liquid bridge (see the sketch in Fig. 2.9 a). Based on geometry, we can write  $\Delta p$  as a function of  $\beta$  and  $s$  with  $r_1 = \frac{R(1-\cos\beta)+s/2}{\cos(\beta+\theta)}$ , and  $r_2 = R \sin \beta - r_1(1 - \sin(\theta + \beta))$ . As the example with  $s = 0.02R$  shown in Fig. 2.9 demonstrates, there exists a critical  $\beta_c \approx 0.055$  at which  $\Delta p$  exhibits a valley, suggesting a minimum of the Laplace pressure. Because of the pressure difference in various liquid bridges, liquid transport is expected to occur through either the thin film covering the particles or through the vapor phase. For  $\beta < \beta_c$ , liquid transports from small to large liquid bridges since larger ones have relatively small pressure in the liquid phase. On the contrary, liquid transports from large to small bridges for the case of  $\beta > \beta_c$ . Thus, the

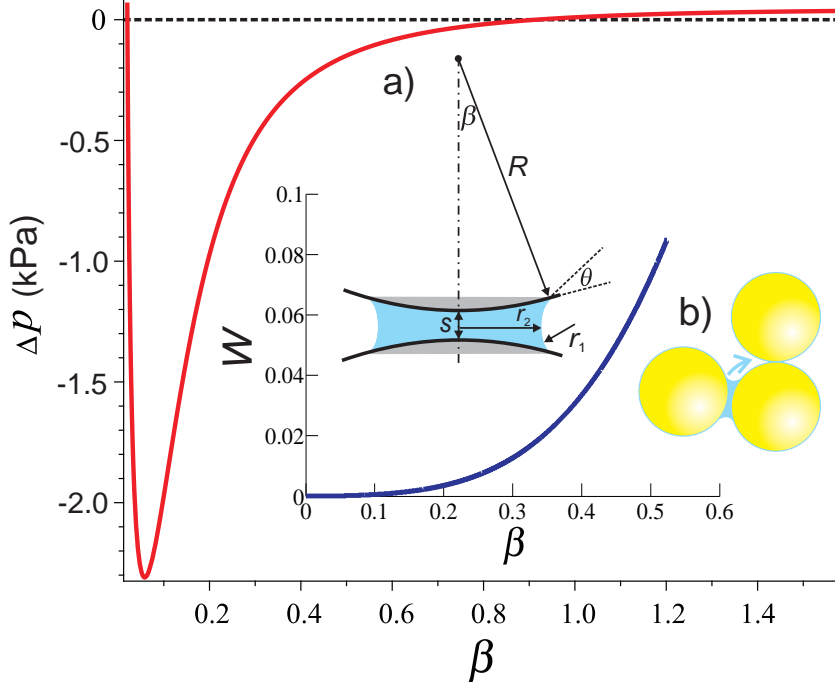


**Figure 2.9:** Laplace pressure of capillary bridges with the half opening angle  $\beta$  of the liquid bridge. Inset figure shows the liquid content  $W$  as a function of  $\beta$ . Sketch a) illustrates liquid transport from one capillary bridge to the other. Sketch b) shows a capillary bridge with definitions of various variables (see text for details).

critical angle  $\beta_c$  acts as an attractor for equilibration of the volume of liquid bridges (see Fig. 2.9 b) for a sketch). Such kind of equilibration is indeed found in computer tomography measurements of wet glass beads after shaking [Scheel *et al.*, 2008]. Note that the positive  $\Delta p$  at  $\beta > 0.9$ , suggesting the sign change of the curvature of the liquid bridge, is not realistic because merging of liquid bridges starts already at  $\beta = \pi/6$  for the ideal case of a triangular configuration.

Experimentally, the half opening angle is not a well accessible parameter. Since the change of  $\beta$  arises predominately from change of bridge volume, we can use bridge volume  $V_b$ , or liquid content  $W$  associated as control parameters. Simplified estimation of  $V_b = \pi s R^2 \sin^2 \beta$  considering the bridge as a cylinders is typically used in literature (see e.g. Willett *et al.* [2000]). Taking one step further, we remove the volume from the spherical caps (regions shielded with gray in Fig. 2.9 a) and estimate the bridge volume with

$$V_b = \pi R^2 \sin^2 \beta (s + 2h) - \frac{2}{3} \pi h^2 (3R - h), \quad (2.14)$$

with the height of the spherical cap  $h = R(1 - \cos \beta)$ . According to such an estimation (shown in the inset of Fig. 2.9), the valley of Laplace pressure occurs at relatively small liquid content,  $W \approx 0.15\%$ . Although the actual flow of wetting liquid relies on the local vapor pressure, which related to the local curvature by the Kelvin equation, the qualitative trend for the capillary bridges to exchange their volumes toward an equilibrium state should be justified.

From the capillary force-distance relation shown in Fig. 2.8, we integrate for the rupture energy required for the breaking of a capillary bridge. Ignoring the higher order term in Eq. 2.13 and assuming relatively small  $V_b$ , we have

$$E_{cb} \approx 5.2\sigma\sqrt{V_b R} \cos \theta. \quad (2.15)$$

Note that it is independent on the velocity of impact and thus acts as an offset to the energy dissipation associated with the wet impact.

### 2.2.2 Influence from viscosity

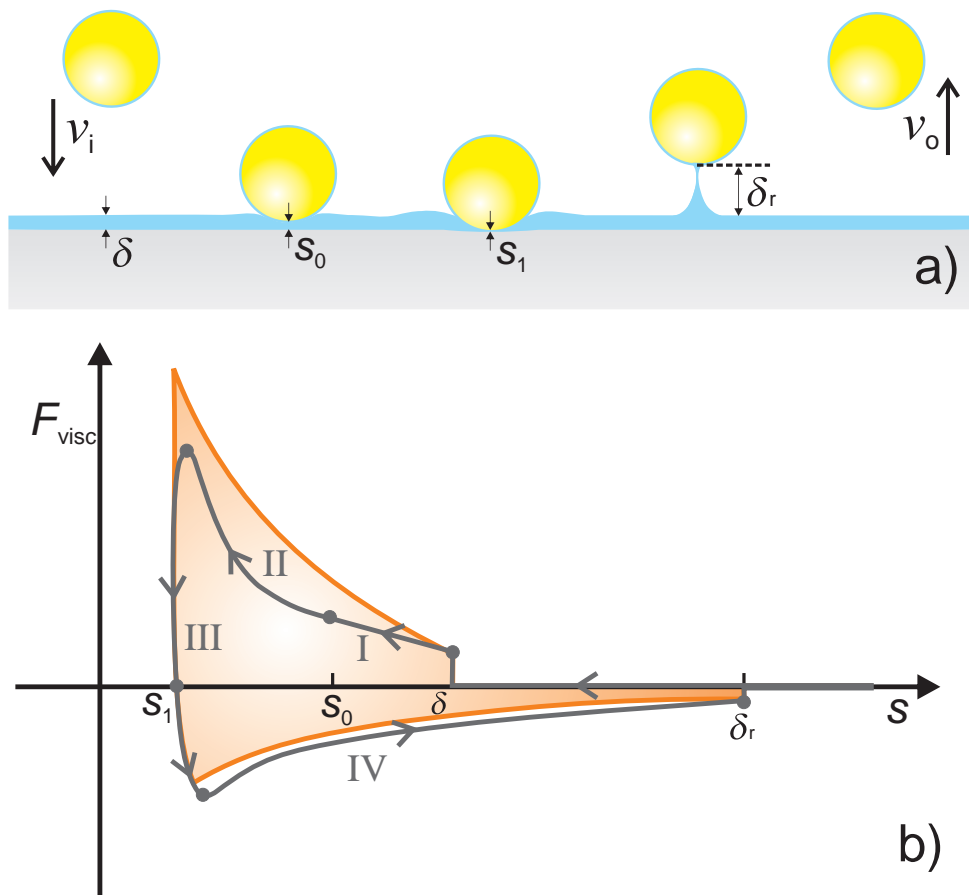


**Figure 2.10:** a) A sketch of a wet impact, where  $v_i$  and  $v_o$  correspond to the impact and rebound velocities,  $\delta$  and  $\delta_r$  are the liquid film thickness and the rupture distance,  $s_0$  is the distance between the particle and the plate as lubrication theory starts to apply, and  $s_1$  is the shortest distance.

As illustrated in Fig. 2.10, the influence from viscous force differs at various stages of the impact. In stage I, from separation distance  $s = \delta$  to the critical distance for the lubrication theory to be valid  $s = s_0$ , we assume Stokes's law for the sake of simplicity,

$$F_{\text{visc}} = 6\pi\mu R\dot{s}, \quad (2.16)$$

with  $\dot{s}$  the velocity of the particle at impact. Note that this is a crude assumption since the coalescence between the liquid film covering the particle and that covering the plate may occur at  $s < \delta$ , owing to the air film in between. As described above, it’s also possible that those liquid surfaces never touch, provided that the time scale of bouncing is shorter than that for the air to escape from the gap. Thus the assumption taken here is expected to be an overestimation. Nevertheless, for liquid with low surface energy that favours coalescence, such an assumption is appropriate.

Stage II starts from  $s = s_0$  to the shortest distance between the particle and the plate  $s_1$ . The starting position  $s_0$  and the corresponding velocity  $v_0$  are used in former literature as free parameters [Davis *et al.*, 1986]. Sometimes  $s_0$  is also chosen as a fixed fraction of the film thickness  $2\delta/3$  [Barnocky & Davis, 1988; Davis *et al.*, 2002], and consequently the velocity  $v_0$  can be derived assuming Eq. 2.16 to be the only dissipative force. In this region, the lubrication theory predicts an enhanced viscous damping force as the two surfaces are close enough to each other

$$F_{\text{visc}} = 6\pi\mu R\dot{s} \cdot \lambda. \quad (2.17)$$

Various empirical forms of the factor  $\lambda$  had been used in literature [Mazzone *et al.*, 1987], such as  $R/s$ ,  $1 + 2R/s$  or  $(1 - \cos(2\beta))/2$ . In comparison to the Stokes’ law (Eq. 2.16), the additional factor states that the viscous damping force diverges as the two surfaces are infinitely close to each other. Thus the viscous force reaches its maximum at  $s = s_1$ . For the sake of simplicity, we take  $\lambda = R/s$  for the calculations below. In reality, the two surfaces cannot be infinitely close to each other due to the surface roughness, which endows the other integration limit for an estimation of the energy loss in this region.

In stage III,  $F_{\text{visc}}$  decays until a negative peak value is reached, where the velocity and the viscous force change the sign. Suppose the change of  $s$  in this region is small, the valley corresponds to the largest rebound velocity during the impact.

In stage IV, the lubrication theory is still considered to be valid, thus the same force law as in Eq. 2.17 applies. Additionally,  $F_b$  starts to play a role in this region since a capillary bridge is developing.

With the viscous force-distance relations described above, one could proceed to estimate the total viscous damping during the whole impact. The four stages described above are illustrated in Fig. 2.10 as the closed solid curve, the area of which corresponds to the energy dissipated. For relatively thin films, the factor  $R/\delta$  is sufficiently large so that the viscous damping from stage I much less than II, thus we can ignore stage I and consider stage II to start at  $s = \delta$ . Moreover, for relatively hard impacts, the velocity turnover takes place in a rather narrow region roughly two orders of magnitude smaller than the film thickness [Marston *et al.*, 2010], thus we can skip the energy dissipation in region III. Based on the above assumptions, the solid curve could be further simplified into the orange one considering only the lubrication forces. Consequently, the energy dissipation during the whole impact from viscosity can be estimated with the integrations of Eq. 2.17 for both approaching and rebounding phases,

$$\Delta E_{\text{visc}} = 6\pi\mu R^2 v_i \left( \ln \frac{\delta}{\epsilon} + e_n \ln \frac{\delta_r}{\epsilon} \right), \quad (2.18)$$

with the roughness of the sphere  $\epsilon$  taken as the integration limit. Note that constant velocities are assumed through the impact and rebound regions. For relatively hard im-

pact, e.g., the glass beads used here, this assumption is appropriate, since the measurements by Marston *et al.* [2010] show that velocity change takes place predominately in a rather narrow region, roughly two orders of magnitude smaller than the film thickness .

### 2.2.3 Influence from inertia

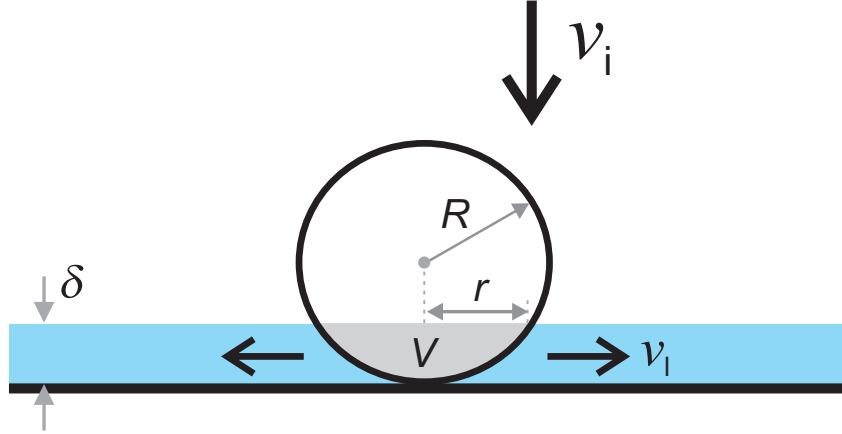


**Figure 2.11:** A simplified view on the momentum transfer from the particle to the liquid being pushed aside, based on which a model (see text for details) is derived to account for the energy dissipation from the inertia effect.

As described at the beginning of this section, hydrodynamics of the liquid film induced by the bouncing sphere, particularly in association with the air film trapped in between, can be complex. As a starting point, we skip all those complex influences and discuss only the energy loss due to the repelled volume from the sphere penetrating into the liquid film (sketched in Fig. 2.11). In such a case, the time scale required for the sphere to travel from the surface of liquid film to the glass plate can be estimated with  $t = \delta/v_i$ , assuming  $v_i$  to be constant during the penetration period. In the quasi-static limit, the volume of the liquid being pushed aside equals to the spherical cap volume  $V = \pi\delta(3r^2 + \delta^2)/6$ . Here it is assumed that the film thickness is constant, and  $r = \sqrt{\delta(2R - \delta)}$  is the radius of the base of the spherical cap, which can be treated as the length scale for the squeezed liquid to travel. Combining the length and time scales gives rise to a velocity  $v_l = l/t$ , which could be approximately considered as the average velocity of the liquid being squeezed aside. Therefore, the kinetic energy taken by the liquid can be estimated with

$$\Delta E_{\text{int}} = \frac{1}{2}\rho_l V v_l^2 = 3\tilde{\rho} \left( \tilde{\delta} - \frac{5}{3}\tilde{\delta}^2 + \frac{2}{3}\tilde{\delta}^3 \right) E_i, \quad (2.19)$$

where  $\tilde{\delta} = \delta/2R$  and  $\tilde{\rho} = \rho_l/\rho_p$  are defined as the dimensionless film thickness and liquid density.

Note that this part of energy dissipation scales linearly with the kinetic energy at impact  $E_i$ , different from the viscous and the capillary effects discussed above.

## 2.3 Scaling

Based on the above analysis on various energy dissipation mechanisms, we proceed in this section to estimate the COR for wet impacts. Based on the definition of the COR, we have

$$e_n = \sqrt{1 - \Delta E_{\text{diss}}/E_i} \quad (2.20)$$

with  $E_{\text{diss}}$  the total energy dissipation. Note that it is not the energy dissipated into heat, but the energy loss of the particle during the impact here. Such a total energy dissipation could be attributed to the inelastic deformation of the particles as in the case of dry impact, as well as the inertia, viscous and capillary forces arising from the presence of the wetting liquid. Suppose the effect from the inelastic deformation of the solid phase is independent from the other mechanisms associated with the wetting liquid, we have  $\Delta E_{\text{diss}} = \Delta E_{\text{dry}} + \Delta E_{\text{wet}}$ . Further assuming that the energy dissipation from such inelastic deformation is identical to the impact without the wetting liquid, i.e.,  $e_{\text{dry}} = \sqrt{1 - \Delta E_{\text{dry}}/E_i}$ , and taking into account the three possible mechanisms discussed above, we have

$$e_n = \sqrt{e_{\text{dry}}^2 - \frac{\Delta E_{\text{int}}}{E_i} - \frac{\Delta E_{\text{visc}}}{E_i} - \frac{\Delta E_{\text{cb}}}{E_i}}. \quad (2.21)$$

Before start to discuss the analytical solution of  $e_n$ , we first analyze the scaling of the wet COR with the impact velocity. Based on Equations (2.15), (2.18) and (2.19), we find that the inertia term leads to a constant offset to the COR with respect to  $e_{\text{dry}}$ , the viscous effect leads to a term  $\propto 1/v_i$ , and the influence from capillary forces gives rise to a term  $\propto 1/v_i^2$ . Thus, Eq. 2.21 predicts a monotonic growth of  $e_n$  with  $v_i$ . Moreover, it also predicts that no real COR value for  $v_i$  below a critical value  $v_c$ , since a negative value in the square root is not realistic. Experimentally,  $v_c$  corresponds to the case of no rebound, i.e. the kinetic energy completely damped in the one impact. This is in contrast to the case of dry impact (Eq. 2.7), where the COR decays as impact velocity grows. A comparison between the predicted dry and wet impacts is illustrated in the upper panel of Fig. 2.12. Finally, Eq. 2.21 suggests that the wet COR saturates as  $v_i \rightarrow \infty$ , and this limiting value  $e_{\text{inf}}$  is smaller than the corresponding dry COR, owing to the inertia effect. Analytically, it can be estimated with

$$e_{\text{inf}} = \sqrt{e_{\text{dry}}^2 - 3\tilde{\rho} \left( \tilde{\delta} - \frac{5}{3}\tilde{\delta}^2 + \frac{2}{3}\tilde{\delta}^3 \right)}. \quad (2.22)$$

The above relation suggests the important role that two dimensionless numbers,  $\tilde{\delta}$  and  $\tilde{\rho}$ , play: Relatively larger density or thicker liquid film with respect to the particle size leads to more energy taken by the inertia effect, and hence smaller  $e_{\text{inf}}$ .

Accordingly, we may rewrite Eq. 2.21 in terms of impact velocity  $v_i$  as

$$e_n = \sqrt{e_{\text{inf}}^2 - \frac{\alpha}{v_i} - \frac{\beta}{v_i^2}}, \quad (2.23)$$

where factors  $\alpha$  and  $\beta$  arise from the influence from viscous and capillary forces.

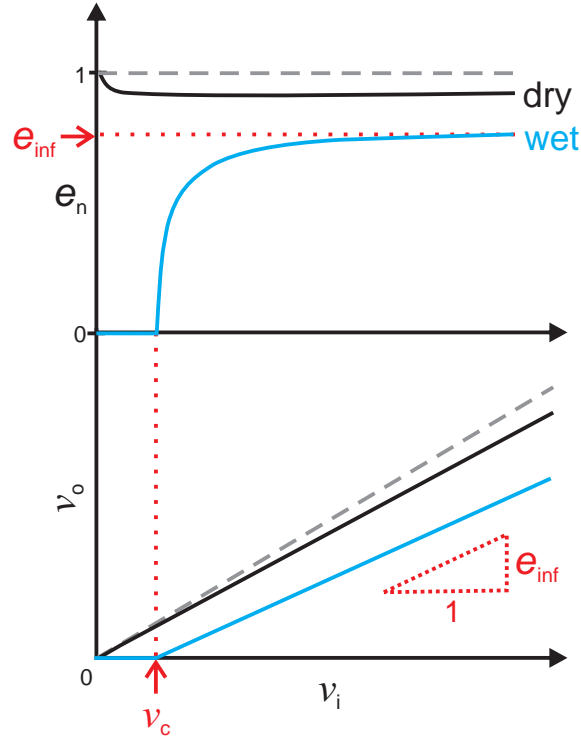


**Figure 2.12:** Normal coefficient of restitution (upper panel) and the rebound velocity  $v_r$  (lower panel) as a function of the impact velocity  $v_i$  for both dry and wet impacts.  $e_{\text{inf}}$  and  $v_c$  correspond to the wet COR at infinitely large  $v_i$  and the threshold impact velocity below which no rebound occurs.

The lower panel of Fig. 2.12 shows that the growth of  $e_n$  with  $v_i$  can be characterized, in the plane of  $v_r$  and  $v_i$ , with a linear fit. The critical impact velocity  $v_c$  and the saturated coefficient of restitution  $e_{\text{inf}}$ , correspond to the offset and the slope of the fit. Such a simplification is based on a recent experimental investigation [R4: Gollwitzer *et al.*, 2012]. In the following part of this subsection, we will discuss in detail how such a linear fit is justified, and the dominating factors determining  $v_c$ .

As the experimental results show in Fig. 2.13 (a), the COR for wet impacts grows monotonically with  $v_i$ , which is suggested qualitatively by Eq. 2.21. Moreover, the growth rate of  $e_n$  relies on the viscosity of the wetting liquid  $\mu$  and the liquid film thickness  $\delta$ , which manifest the influence from  $E_{\text{visc}}$ . Plotting in the plane of rebound  $v_r$  as a function of impact velocity  $v_i$ , it is found that the data fall into lines with various slopes and offsets. From  $v_c$ , one could estimate the critical energy scale  $E_c = mv_c^2/2$  for a rebound to occur, where  $m$  is the mass of the sphere. Note that rebound here is not defined as the turnover of the particle velocity, but as the detachment of the sphere from the wetting liquid, i.e. the rupture of the capillary bridge. The demonstrated possibility to use only two parameters  $E_c$  and  $e_{\text{inf}}$  to describe the impact velocity dependency of the wet COR provides a convenient way to model particle-particle interactions. However, such an approach has to be justified from the perspective of the above prediction (Eq. 2.23).

Assuming the linear fit is a first order approximation of Eq. 2.23, we can ignore higher order term of  $1/v_i$ , i.e., the influence from the capillary force  $E_{\text{cb}}/E_i$ , and expand

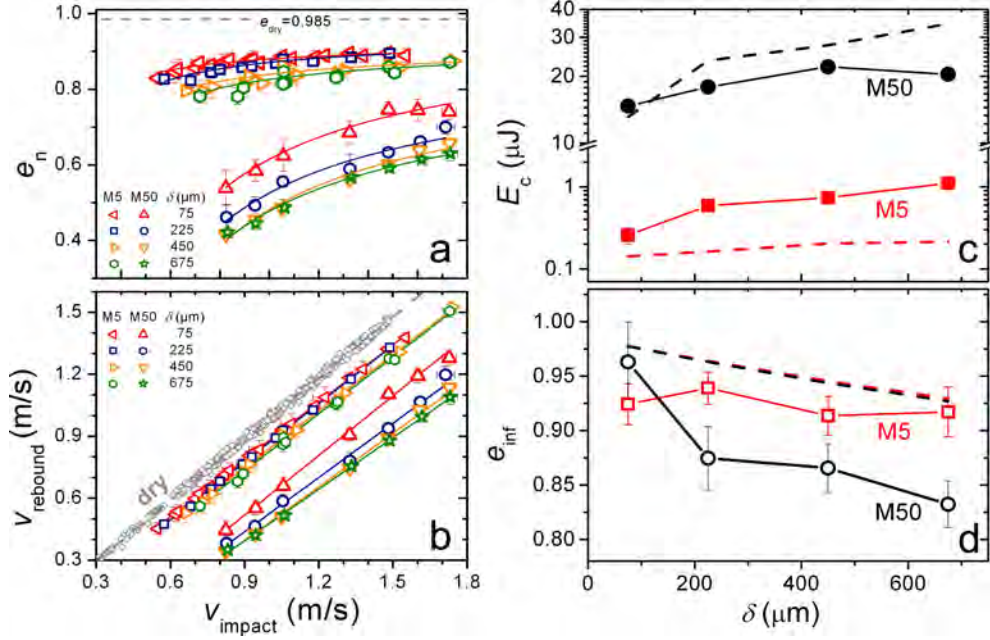


**Figure 2.13:** Normal coefficient of restitution (a) and the rebound velocity  $v_o$  (b) as a function of the impact velocity  $v_i$  obtained experimentally from various liquid film thickness  $\delta$  and two different liquids. The threshold kinetic energy for a wet particle to rebound  $E_c$  and the limiting wet COR  $e_{\text{inf}}$ , both obtained through linear fits of the  $v_o$  vs  $v_i$  data, as a function of the liquid film thickness. Dash lines are predictions from the model described in the text.

$e_n$  into Taylor series in the limit of  $v_i \rightarrow \infty$ ,

$$e_n = e_{\text{inf}} \left( 1 + \frac{\alpha'}{2v_i} - \frac{\beta'}{8v_i^2} + \dots \right) \approx e_{\text{inf}} \left( 1 + \frac{\alpha'}{2v_i} \right), \quad (2.24)$$

where  $\alpha' \equiv \alpha/e_{\text{inf}}^2$  with

$$\alpha = \frac{-9\mu(\ln \frac{\delta}{\epsilon} + \ln \frac{\delta_r}{\epsilon})}{\rho_p R} \quad (2.25)$$

arises from the viscous damping term. Because the factor  $\delta/\epsilon$  for the spheres used in the experiments is large owing to the smooth surface, the influence from the factor  $e_n$  in Eq. 2.18 is presumably small. For the sake of simplicity, it is ignored in the estimation of  $\alpha$ . From a comparison of the first order approximation of Eq. 2.24 to the linear fits used in characterizing the experimental data, we can estimate the critical energy scale,

$$E_c = \left( \frac{\frac{3}{2}\mu(\ln \frac{\delta}{\epsilon} + \ln \frac{\delta_r}{\epsilon})}{e_{\text{inf}}^2} \right)^2 \frac{6\pi R}{\rho_p}, \quad (2.26)$$

which relies mainly on the viscous damping. At first glance, it might be surprising to see that the rupture energy of the liquid bridges does not play a role since the snapshots shown in Fig. 2.6 demonstrate such a rupture event. However, an estimation of the rupture energy yields  $E_{\text{cb}} \approx 0.7\mu\text{J}$ , which is far less than the kinetic energy of the impacting particles. Note that the various scaling of  $E_{\text{int}} \propto R^3$  and  $E_{\text{cb}} \propto \sqrt{R}$ , the rupture energy will take effect as the particle size and impact velocity are small enough.

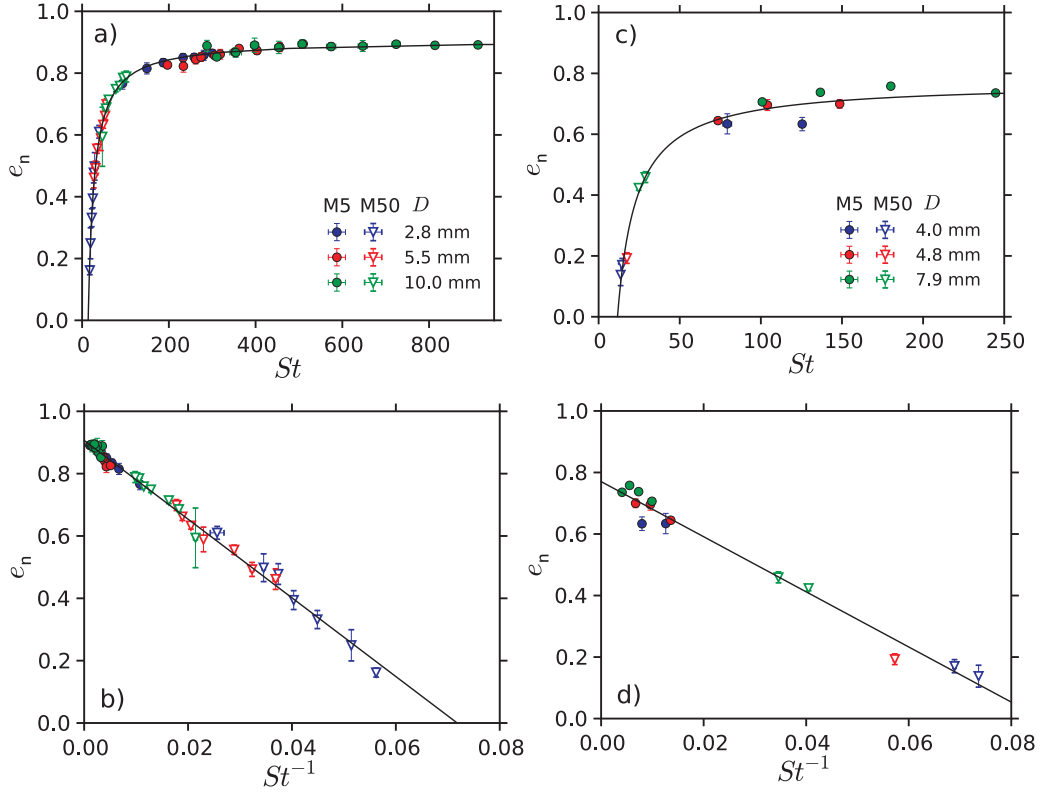


**Figure 2.14:** Scaling of the wet COR with the Stokes number with fixed dimensionless film thickness  $\delta \approx 0.04$  for both glass (a) and PE (b) particles. Figures (a) and (b) adapted from [R4: Gollwitzer *et al.*, 2012] and [R2: Mueller *et al.*, 2013] correspondingly.

Based on the above linear approximation, a comparison of the predicted  $E_c$  and  $e_{\text{inf}}$  to experiments are shown in Fig. 2.13 (c) and (d). Qualitatively, the trend of  $E_c$  and  $e_{\text{inf}}$  are well predicted by the model. Quantitatively, the model gives overestimated  $e_{\text{inf}}$  values in comparison to the experiments. It strongly suggests that a refined model with a proper consideration of the hydrodynamics is needed, because Eq. 2.22 shows that  $e_{\text{inf}}$  relies on the energy dissipation due to the inertia of the liquid. For the comparison of  $E_c$ , a better agreement is found for more viscous M50 wetting case than the order of magnitude less viscous M5 case, suggesting the prediction of  $E_{\text{visc}}$  is more appropriate for more viscous wetting liquid. Considering the simplification applied to the model, such comparison results provide evidence for the approach used here. Further investigations with more detailed description of the inertia part of the energy dissipation will presumably yield better predictions of the fit parameters, thus facilitate a better analytical prediction of the wet COR.

Moreover, after inserting the factor  $\alpha'$  into the above Eq. 2.24, one finds that the approximated  $e_n$  can be written in terms of the Stokes number defined above in Eq. 2.8,

$$e_n = e_{\text{inf}} \left( 1 - \frac{\ln \frac{\delta}{\epsilon} + \ln \frac{\delta_r}{\epsilon}}{e_{\text{inf}}^2} \cdot \frac{1}{St} \right). \quad (2.27)$$

It demonstrates that the dependency of  $e_n$  on the density and size of particles, viscos-

ity of the wetting liquid, and the impact velocity can be replaced by the dimensionless Stokes number that characterizes the inertia of the particle over the viscous force of the wetting liquid. Rescaling of the wet COR with  $St$  has been discussed by several authors (see e.g. Davis *et al.* [1986, 2002]) for the case of highly viscous liquids, i.e. low  $Re$ . For the case of Reynolds number  $Re \gg 1$  focused here, inertia effect associated with  $e_{\text{inf}}$  has to be considered in addition, which suggests scaling with the two additional dimensionless numbers: relative density  $\tilde{\rho}$  and dimensionless film thickness  $\tilde{\delta}$  (see Eq. 2.22).

Experimentally, wet COR for various liquid and particle properties have been measured systematically for glass and polyethylene (PE) particles. As shown in Fig. 2.14, the collapse of data demonstrate that the scaling of  $e_n$  with  $St$  is justified provided that  $\tilde{\delta}$  is fixed [R4: Gollwitzer *et al.*, 2012; R2: Mueller *et al.*, 2013]. Further experiments on various density ratio  $\tilde{\rho}$  are being carried out in order to refine the theory described here for wet COR and figure out how the COR scales with the two additional parameters:  $\tilde{\rho}$  and  $\tilde{\delta}$ .

## 2.4 Wetting

While characterizing the capillary force and the associated energy scale between spherical particles, one typically assumes a constant contact angle  $\theta$ , which is small for typical combinations of wetting liquids and particles used in the lab, such as water or silicone oil on glass. However, in real life applications, the contact angle, which arises from the balance of surface energy at the three phase contact line, will be influenced by a number of factors including surface roughness and chemical impurities of the substance [de Gennes, 1985]. As a consequence, the measured contact angle is typically within a certain range between the advancing  $\theta_{\text{adv}}$  and receding  $\theta_{\text{rec}}$  contact angles. Thus, experimentally measured values scatter and the exact contact angle is typically hard to predict. Moreover, the equilibrium condition (i.e. the Young condition) assumed in many literature is rarely achieved for agitated wet granular matter. Before the system relax to its equilibrium state, another event causing a morphological change of the liquid structure will most likely to occur, leading to a dynamic contact angle. For example, a perfectly wetting liquid evaporating on a perfectly smooth solid substance such as mica may lead to a finite contact angle [Elbaum & Lipson, 1994].

Moreover, contaminations in forms of small dirt particles inside the droplet are found to form rings along the rim of the droplet, i.e. the coffee stain effect [Deegan *et al.*, 1997]. Such a robust effect influences substantially the product quality in various industries, such as printing and coating. Due to the ubiquity of such a non-equilibrium process, the ‘coffee stain effect’ has been a topic of intensive investigations in the past decades, including a characterization of patterns formed by the dirt particles after drying [Deegan, 2000], various methods to reduce such an effect [Eral *et al.*, 2011; Yunker *et al.*, 2011], as well as possible applications on the self-organization of particles [Marín *et al.*, 2012]. For a recent review, the reader may refer to Bonn *et al.* [2009].

For agitated wet granular matter focused here, wetting and non-wetting play an important role as well. Liquid transport inside a wet pile of sand, due to the structure change or inhomogeneous distribution of the wetting liquid, will presumably lead to a distribution of the contact angle between  $\theta_{\text{adv}}$  and  $\theta_{\text{rec}}$ . Therefore, measuring the static contact angle by one set of experiments is not sufficient. Recently, an intjet

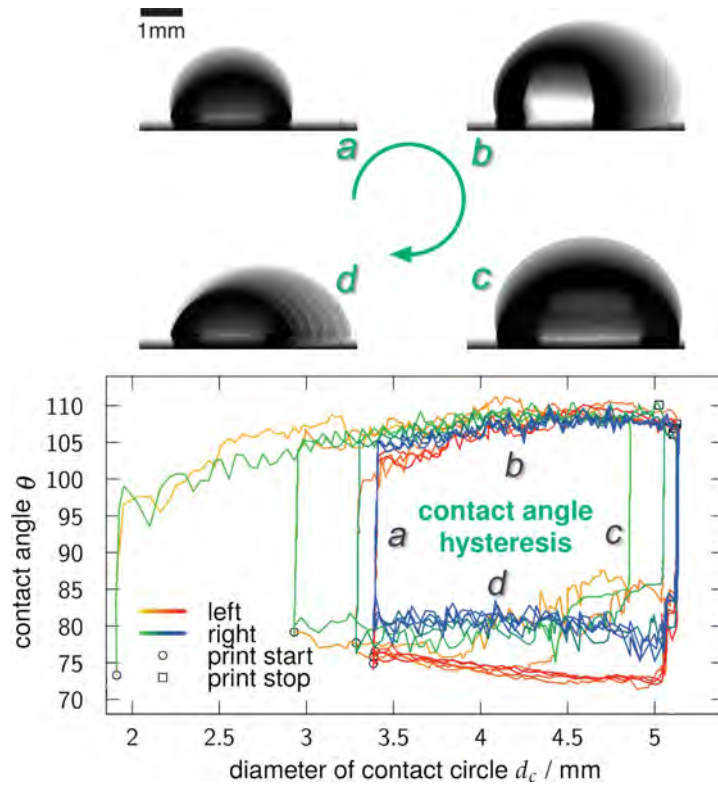


**Figure 2.15:** Contact angle hysteresis represented by a water droplet on a polytetrafluoroethylene (PTFE) surface. Upper panel shows overlaid snapshots of the droplets in the following 4 stages: a. increasing volume with pinned interface, b. advancing after de-pinning, c. decreasing volume with pinned interface, d. receding after de-pinning. The volume increase is controlled with an intjet printing setup [Völkel, 2014], and the volume decrease is caused by evaporation. Lower panel presents the contact angle for both sides of the droplet as a function of the mean diameter of the contact line. The color coding of the curves represents time evolution of the angles. Figure adapted from Völkel [2014].

printing device for the measurement the contact angle hysteresis has been built up [Völkel, 2014], which employs a intjet printer head to add liquid into the droplet in a well controlled and accurate manner. Thanks to the tiny size of its nozzles, such a device provides droplets with a size down to  $\approx 33$  pL.

Figure 2.15 shows the contact angle hysteresis of a water droplet on a polytetrafluoroethylene (PTFE) substance. It contains four phases: From the initial growth of the droplet while printing (a, b), to the following shrinking of the droplet during evaporation (c, d). As the contact line is pinned, the droplet may have any contact angle in between the limiting  $\theta_{adv}$  and  $\theta_{rec}$ . As de-pinning starts as the limiting contact angles are achieved. From the overlaid snapshots shown in the upper panel, it is obvious that such a process may not be homogeneous: De-pinning may occur at one edge of the rim, a manifestation of the surface inhomogeneity. In total, 6 runs of printing-evaporating cycles are performed. Printing starts initially on a small droplet of  $\approx 1.8$  mm, leading to a symmetrically growing contact angle, as shown in overlaid snapshot Fig. 2.15 (a). As  $\theta_{adv}$  is achieved, contact line de-pins and the contact angle grows slightly as well. After a certain amount of water is printed, the shrinking of the droplet starts due to

evaporation. Contact angle reduces until  $\theta_{\text{rec}}$  is reached. In stage d, the droplet shrinks at the receding angle  $\approx \theta_{\text{rec}}$  until the given evaporating time is reached.

Continuous 6 experimental runs yield a similar behaviour. After 2 cycles, the sizes of the droplets in region a and c start to be fixed, demonstrating the reproducibility of the experiment. In region d, the contact angle from either side differs, which can be attributed to the surface inhomogeneity arising from the ‘coffee stain effect’. Indeed, ring patterns are observed in the region of the evaporating droplet at the end of the experiment. This preliminary experiment indicates the existence of a ‘limiting cycle’ for the contact angle hysteresis, within which both advancing and receding contact angles could be determined accurately. Further experiments on how the contact angle depends on the experimental details such as the droplet printing rate, or the time for printing and evaporation will help to check the robustness of the measured contact angles.

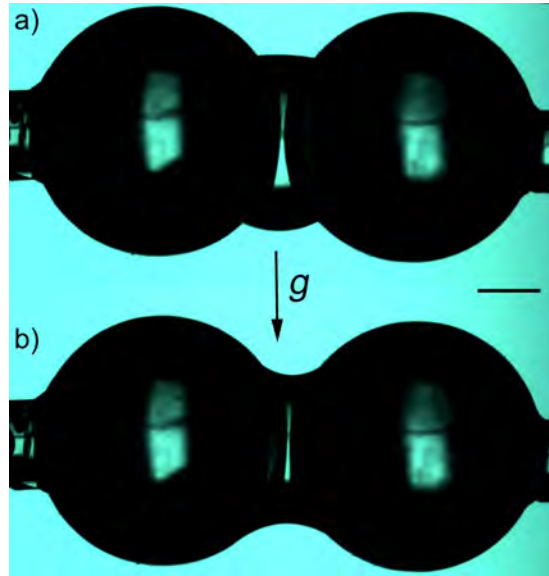


**Figure 2.16:** Snapshots showing the dynamics of a capillary bridge between two glass spheres with a diameter of 4 mm during advancing (a) and receding (b) stages. The scale bar corresponds to 1 mm.

Within the geometry of a liquid bridge between two equal-sized spheres, as shown in Fig. 2.16, the contact angle hysteresis will presumably be influenced by other factors such as gravity. Further experiments on such a geometry, aiming at finding the ‘limiting cycle’ for the measurements of  $\theta_{\text{adv}}$  and  $\theta_{\text{rec}}$  in such a geometry will be a topic of further investigations. From the snapshot shown here, one could clearly see the influence from pinning as well as gravity on the contact angle: During the printing period, advancing contact angle can be as large as  $71^\circ$  for the case of water wetting on glass. Such a large contact angle will presumably lead to a weakened cohesive force in such a period. Thus, the contact angle hysteresis can be an essential factor to be considered for the investigations of wet granular dynamics.

In Chapter 2, the dissipative nature of granular particle interactions, especially with wetting liquid mediated, is demonstrated. It is because of this nature that the collective behaviour of agitated granular particles is characterized as far from thermodynamic equilibrium. In such non-equilibrium systems, many counter-intuitive phenomena have been discovered, such as clustering of granular gases [Goldhirsch & Zanetti, 1993; Olafsen & Urbach, 1998] that is claimed to be associated with the formation of planetary rings [Spahn & Schmidt, 2006], high energy tail of the velocity distributions [Brey *et al.*, 1999; Brilliantov & Pöschel, 2004], shock wave propagation [Losert *et al.*, 1999; Bougie *et al.*, 2002; Huang *et al.*, 2006], heap formation, transport and associated migration of sand dunes in nature [Faraday, 1831; Bagnold, 1941; Clément *et al.*, 1992; Falcon *et al.*, 1999; Miao *et al.*, 2006], an analogue of Maxwell’s Demon [Eggers, 1999; Reimann, 2002; Eshuis *et al.*, 2010], Reynolds dilatancy [Reynolds, 1885; Onoda & Liniger, 1990; Schröter *et al.*, 2007; Métayer *et al.*, 2011], size (Brazil nut effect) or density segregations [Rosato *et al.*, 1987; Hong *et al.*, 2001; Reis & Mullin, 2002; Burtally *et al.*, 2002; Breu *et al.*, 2003; Schnautz *et al.*, 2005; Schröter *et al.*, 2006], as well as localized excitations [Umbanhowar *et al.*, 1996]. In comparison to the states of matter in thermodynamic equilibrium, granular matter may also behave like a solid, a liquid or a gas [Jaeger *et al.*, 1996], depending on the balance between the energy injection and the dissipation. Thus, a straightforward question is: How well can we extend existing knowledge on equilibrium systems to such a non-equilibrium model system, and how well can such extensions shed light on our understanding of the omnipresent non-equilibrium systems in nature, from active particles such as bacteria colonies [Zhang *et al.*, 2010], or actin filaments [Schaller *et al.*, 2010] to animal groups [Buhl, 2006; Couzin *et al.*, 2005; Liu *et al.*, 2013].

To address these questions, collective behaviour of agitated wet granular matter, which can be treated as a non-equilibrium model system, will be discussed in this chapter. In Section 3.1, I will demonstrate with a ‘quantum paste’, i.e. granular particles wetted by liquid helium, that a few atomic layers of liquid coverage are sufficient to influence the rigidity of the sample. After a brief review on the dynamics of dry granular matter in Section 3.2, the collective behaviour of wet granular matter under vertical (Section 3.4) and horizontal (Section 3.3) agitations will be presented, including phase transitions, pattern formation and clustering. Finally in Section 3.5, recent progresses on the influence from shape on the ordering transitions of granular particles will be summarized in short.

### 3.1 How wet is wet?

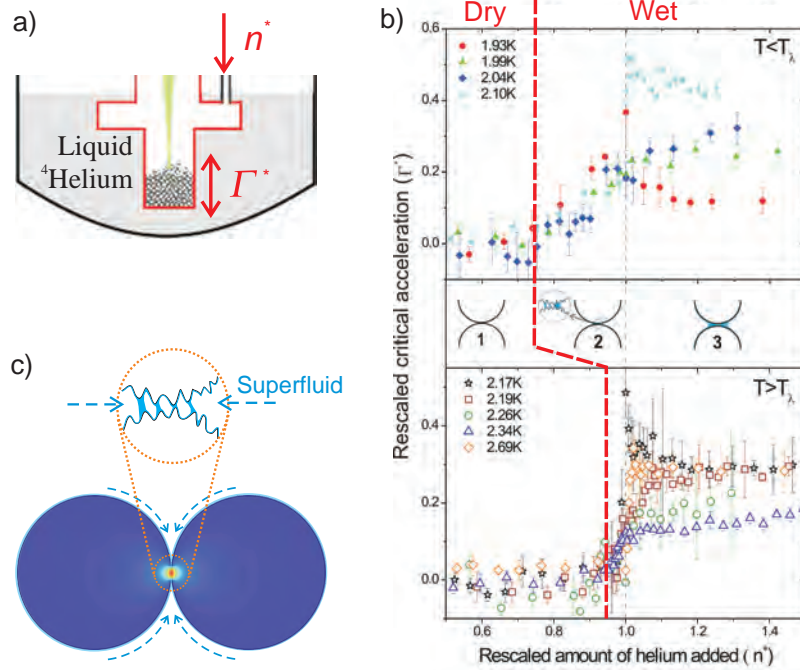


**Figure 3.1:** The liquid  ${}^4\text{Helium}$  wetting experiment to probe the threshold between dry and wet granular matter. a) A sketch of the sample cell with the control and order parameters illustrated. Here the control parameter  $n^*$  is the rescaled amount of helium added, and the order parameter  $\Gamma^*$  is the rescaled critical acceleration for the granular sample to fluidize. b) The rigidity enhancement represented by  $\Gamma^*$ , as a function of  $n^*$  at temperature below (upper panel) and above (lower panel) the  $T_\lambda$ , the transition temperature between normal and superfluid helium. Various wetting regimes are sketched in the middle panel, where 1, 2 and 3 correspond to dry, asperity wetting and completely wetting regimes. c) An illustration on the energy dissipation induced enhancement of the capillary bridges formed at the asperity level for superfluid wetting. The colors represent local temperature gradient close to the contact point (warmer color corresponds to higher temperature). Figures adapted from R8: Huang *et al.*, [2009a].

As shown in Section 1.1, wet granular matter can be classified with the amount of wetting liquid added. In contrast to the boundary between the asperity and complete wetting regimes that can be estimated from the roughness  $\epsilon$  and size of the particles (more specifically from  $\sqrt{\epsilon^2 R}$ ) [Halsey & Levine, 1998], the threshold for the cohesion to start, i.e. the boundary between dry and the asperity wetting regime, is still unclear. This is a non-trivial question to be addressed experimentally since wetting is typically not considered as homogeneous in a granular packing, as discussed in Section 2.4. Moreover, the amount of wetting liquid added can not be precisely controlled and distributed homogeneously. In a recent work [R8: Huang *et al.*, 2009a], liquid  ${}^4\text{Helium}$  has been used as wetting liquid to address this question. The use of such a special liquid has the following advantages: (i) A low surface energy that facilitates wetting of

almost all surfaces; (ii) A well controllable volume down to an atomic level owing to the well calibrated isotherms; (iii) A superfluid phase without the influence from viscosity.

As sketched in Fig. 3.1 (a), the amount of liquid helium is controlled by the amount of helium gas added. Above the saturated vapor pressure, all the amount of gas added is expected to condense on the sample. Below the saturated vapor pressure, the liquid film thickness can be estimated from the vapor pressure measured in the sample cell. For a better comparison of the results from various temperatures, the amount of wetting liquid added  $n^*$  is rescaled by the amount of helium for the saturated vapor pressure to be reached. To check the rigidity enhancement due to wetting, vertically sinusoidal vibrations are applied to the sample. The order parameter is chosen to be  $\Gamma^* = \Gamma_{\text{wet}}/\Gamma_{\text{dry}} - 1$ , where  $\Gamma_{\text{wet}}$  corresponds to the critical peak acceleration for the particles on the top layers to move, and  $\Gamma_{\text{dry}}$  is the corresponding critical value obtained without any helium added. To visualize the mobility of particles, a green laser beam is used to illuminate the sample, and a sensitive camera is employed to visualize the variations of the speckle patterns reflected from the sample. As demonstrated in Fig. 3.1 (b), the transition from dry to asperity wetting regimes may start well below the saturated vapor pressure is reached at  $n^* = 1$ . Based on the isotherms measured for  $^4\text{He}$  at various temperature [Bower, 1953], this transition corresponds to  $\approx 5$  atomic layers of liquid helium coverage.

Moreover, a comparison between temperature below and above  $T_\lambda$  suggests enhanced rigidity starts at a smaller  $n^*$  for superfluid than for normal fluid wetting. This can be attributed to the ‘fountain effect’: As illustrated in Fig. 3.1 (c), collisions between particles generate local heat gradient in the vicinity of the contact point, owing to the energy dissipated. Such a heat gradient effectively drives the flow of superfluid helium toward the contact point, which facilitates the formation of capillary bridges at a ‘microscopic’ level as well as the enhanced rigidity of the sample at a ‘macroscopic’ level.

In a former experiment [Hornbaker *et al.*, 1997] using the angle of repose of oil wetting polystyrene beads to address this question, a threshold liquid film thickness was found to be  $\approx 20$  nm. Here we demonstrate that this threshold can be as low as a few atomic layers, suggesting that the influence from humidity is ubiquitous and hence needs to be considered carefully in real life applications.

## 3.2 Dry granular dynamics: A brief review

After the threshold between dry and wet granular matter is distinguished, let’s start with a brief review on the dynamics of dry granular matter, particularly the transition from a solidlike to a liquidlike state and the collective behaviour associated. It serves as a basis for further comparisons to the dynamics of wet granular matter.

In the helium wetting experiment, the fluidization threshold of vertically agitated granular matter is used as the order parameter. More specifically, it corresponds to the critical acceleration, or force, applied to mobilize particles on the top layers. The melting process of dry granular matter, due to its wide applications in the industries, has been a topic of interest over the past two decades. The important questions are the thresholds for the melting to start and to complete, and the key control parameters or scaling associated. More specifically for agitated monolayer systems, the question of whether the two stage melting scenario predicted by the KTHNY theory [Halperin &

Nelson, 1978; Strandburg, 1988] applies for such a non-equilibrium system or not arises. For a monolayer of particles both confined and agitated in the direction parallel to the gravitational acceleration  $\vec{g}$ , such a two stage continuous melting scenario predicted by KTHNY theory for equilibrium systems applies [Olafsen & Urbach, 2005]. However, for a monolayer of particles confined in the direction perpendicular but driven parallel to  $\vec{g}$ , a layer by layer granular meltdown, as well as discontinuous transitions are found [Götzendorfer *et al.*, 2006]. The peak vibration velocity was found to be the critical parameter determining the fully fluidized state, suggesting an energy driven phase transition. This is in contrast to former investigations on the start of melting in a similar system, where  $\Gamma$  was used to characterize the transition threshold, and a typical threshold  $\Gamma \approx 1.2$  was found [Clement & Rajchenbach, 1991].

Dating back to the investigations on the heap formation by M. Faraday [Faraday, 1831], the convection in agitated granular layers has been found to be an ubiquitous phenomenon, which may arise from interstitial air [Laroche *et al.*, 1989] or container walls [Clément *et al.*, 1992; Knight *et al.*, 1993]. Moreover, at a larger agitation strength, more pairs of convection rolls, typically with particles close to the wall flowing upwards, were detected [Aoki *et al.*, 1996]. This behaviour is drastically different from the wall induced convection where typically two convection rolls with downward particle motions close to the walls are present [Clément *et al.*, 1992; Knight *et al.*, 1993]. In a recent work [Eshuis *et al.*, 2007], a phase diagram of agitated dry granular matter is presented, where the convection pattern is found to be a robust behaviour covering a wide parameter range. Indeed it is found to be a ubiquitous phenomenon widely existing in various industries, and triggering undesired mixing and segregation effects [Rosato *et al.*, 1987; Duran *et al.*, 1993, 1994; Shinbrot & Muzzio, 1998; Hong *et al.*, 2001; Reis & Mullin, 2002; Burtally *et al.*, 2002; Breu *et al.*, 2003; Schnautz *et al.*, 2005; Khan & Morris, 2005; Schröter *et al.*, 2006]. More recently, single convection roll has also been found in a slowly rotating quasi-two-dimensional sand box on the rim of jamming, suggesting that temporal and local heterogeneous motion of particles is sufficient to generate convective motion [Rietz, 2013]. Despite of the long history of investigations and wide applications in the industries, the emerging counter-intuitive behaviour of convective motions in agitated granular matter indicate that a comprehensive understanding on the origin of convection has not yet been accomplished.

Utilizing experiments and molecular dynamics (MD) simulations, we have recently addressed the question of how defects play the role in triggering the convective motion [P1: Fortini & Huang, 2014]. Fig. 3.2 shows a sequence of snapshots taken from the experiments. As the displacements of the tracer particles marked with blue suggest, mobilized particles in a very narrow region (2 columns in this case) close to the wall, where defects are most likely to be generated, are sufficient to induce the convective motion. While in the bulk region, the particles stay in a crystalline phase and move upward collectively step by step (see tracer particles marked in red). In some occasions, the regions close to the wall are not symmetric, owing to the configurations of the initial defects. Consequently, the downward flow velocity differs from the left to the right sides. In extreme cases, single convection roll can also be detected. Thus, we conclude that the onset of convection is associated with the generation of defects upon agitations. Therefore, strong dependency on the initial configurations of the defects should be expected.

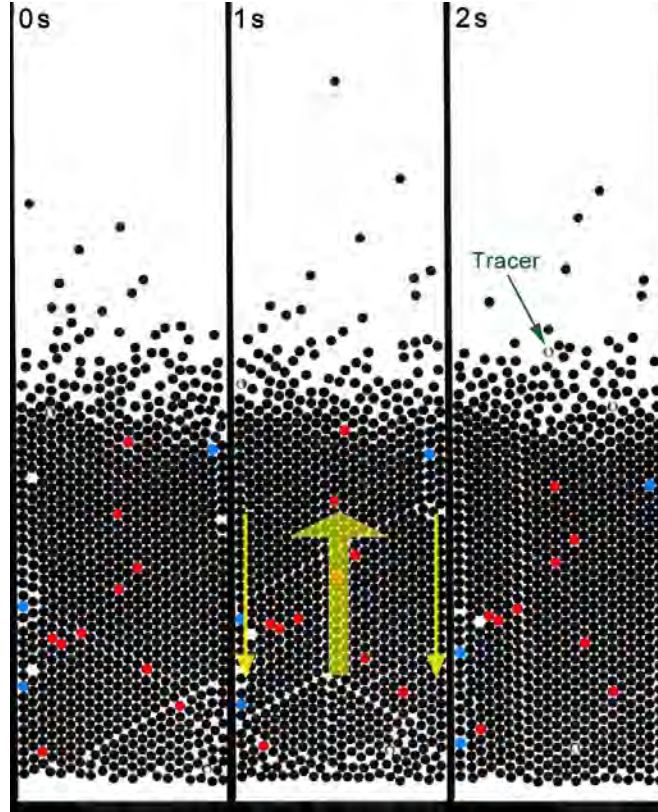


**Figure 3.2:** Sequence of snapshots showing the convection in a monolayer of glass spheres under sinusoidal agitations against gravity. The vibration frequency  $f = 10$  Hz and the dimensionless acceleration  $\Gamma = 4.53$ . Red and blue dots mark the tracer particles that are moving up and down correspondingly, as illustrated with the yellow arrow overlaid on the middle snapshot. Note that the download motion occurs in a very narrow region ( 2 columns) next to the walls, while the upward motion is manifested by the collective motion of hexagonally packed particles in the bulk.

Good agreements between experiments and MD simulations with defects initiated are found for the onset of convection. MD simulations for a crystal initialized without defects predict a larger agitation strength for the onset of convection, because defects have to be generated first. As the agitation strength increases, one can distinguish three regimes: A bouncing bed regime with all particles move collectively, a defects generating regime where sharp growth of the slip probability<sup>1</sup> can be detected, and a convective regime.

Moreover, the slip probability  $p_s$  is found to follow Arrhenius type law  $p_s \propto e^{-\frac{E_b}{K_m}}$ , which suggests the existence of activation events, where  $E_b$  and  $K_m$  correspond to the activation and injected energy scale. Thus, we reach to the conclusion that sufficient energy injection to overcome the activation energy for a particle to move out of its cage determines whether a convection starts or not.

Beside vertical agitations against gravity that have been frequently employed to investigate granular dynamics, horizontal agitations or a combination between horizon-

<sup>1</sup>A slip event is defined as a displacement of a particle with respect to two nearest neighbours greater than  $0.4R$  after one oscillation.

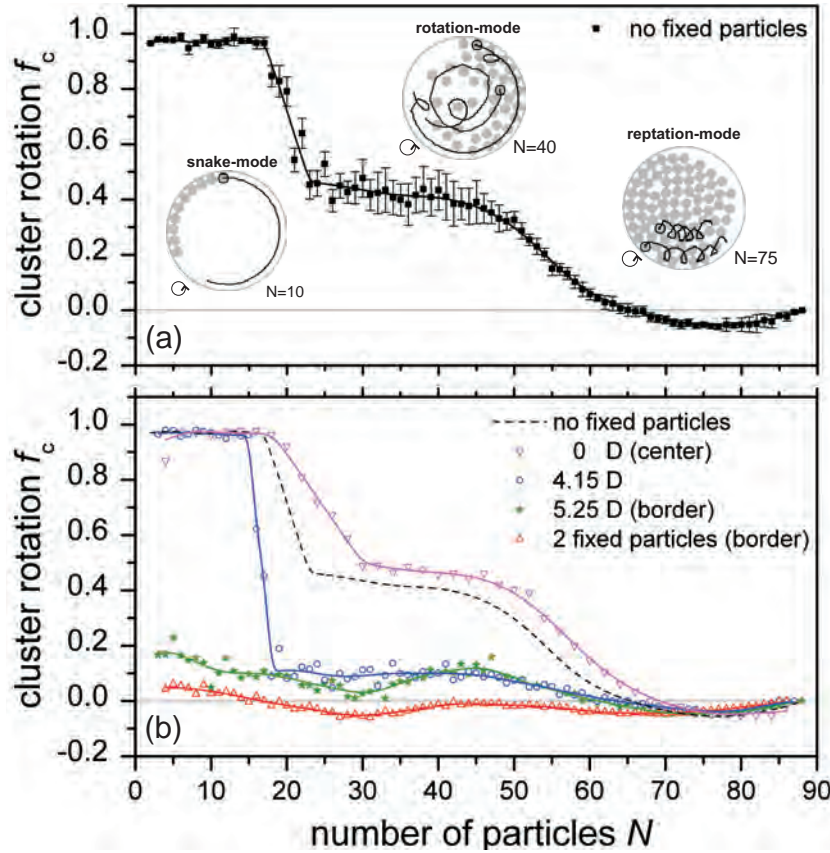


**Figure 3.3:** Rescaled rotation frequency of a dry granular cluster under horizontal swirling motion  $f_c$  as a function of number of particles added without (a) and with (b) intruders at various distances to the center of the container. Three modes, namely snake-mode ( $f_c = 1$ ), rotation-mode ( $f_c > 0$ ) and reptation-mode ( $f_c < 0$ ) can be distinguished. Insets are snapshots from various modes with the trajectories of tracer particles presented as solid lines.

tal and vertical agitations have also been used to check the universality of the phase behaviour of agitated granular matter (see e.g. R7: Huang *et al.*, [2010] for a review). With agitations perpendicular to the gravitational force, the influence from gravity can be minimized. Alternatively, the rolling friction of spheres on the plate [Kondic, 1999] is found to play an important role [Ristow *et al.*, 1997; Tennakoon *et al.*, 1999; Straßburger & Rehberg, 2000; Aumaître *et al.*, 2003].

By combining two horizontal vibrations that are perpendicular with each other, one generates a swirling motion for energy injection. This type of driving is isotropic, since all the points of the container perform the same type of orbit motion and the energy injection through collisions between particles and the container wall is independent on the phase when impacts occur. In Fig. 3.3 (a), collective behaviour of cohesionless particles in such an apparatus is presented [R10: Feltrup *et al.*, 2009]. As shown in the insets, three modes can be distinguished: (i) A snake-mode with all particles line up at the boundary layer and move collectively with the same direction and collectively rotational frequency  $f_c$  as the swirling container. (ii) A rotation-mode with randomness generated through particle-particle collisions and a reduced but still positive  $f_c$ . (iii) A reptation mode with a negative  $f_c$ . The rotation-reptation transition suggests a

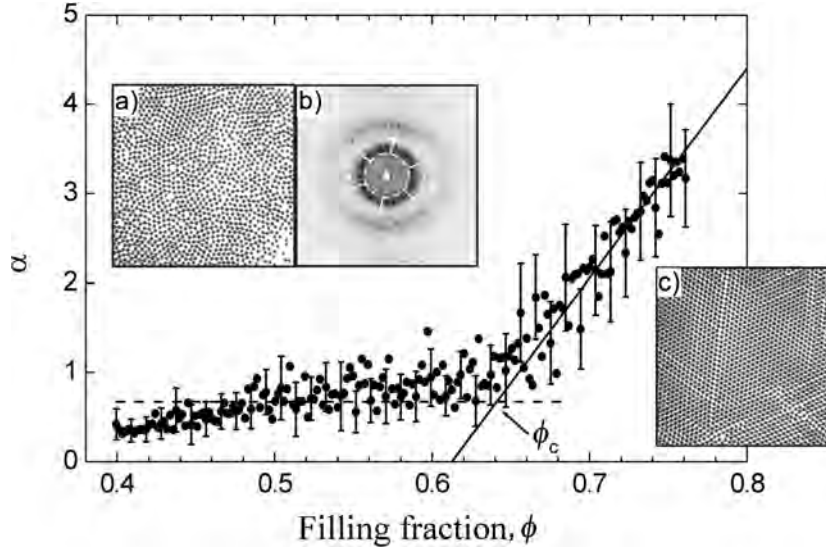


**Figure 3.4:** Ordering transition of spherical particles under horizontal swirling motion. a) and c) are snapshots of a liquidlike (area fraction  $\phi=0.46$ ) and a crystalline ( $\phi=0.76$ ) state correspondingly. b) 2D power spectrum of snapshot a). The order parameter  $\alpha$  is chosen as the normalized intensity variation in azimuth direction in the power spectrum. The critical area fraction  $\phi_c$  is found to be  $0.64 \pm 0.01$ . Adapted from Aumaître *et al.* [2003].

threshold area fraction where the cluster does not rotate. Such a change of the rotation direction may cause problems in applications such as the vibrational mills for grinding feed materials [Yokoyama *et al.*, 1994; Inoue & Okaya, 1994].

To shed light on possible ways to control or to avoid such a transition, intruders are placed inside the swirling table to disturb the dynamics of the cluster. As shown in Fig. 3.3 (b), the rotation frequency can actually be enhanced with the presence of the intruder in the middle of the container. A broken symmetry with the intruder placed away from the center leads to a suppressed rotation, demonstrating the possibility to control the cluster rotation through intruders added inside. Such an effect may have potential applications in the industries to improve mixing or transport processes. Moreover, it is demonstrate that  $f_c$  is directly linked to the number of particles staying at the border of the container, indicating that the rotation and reptation motion is mainly driven by the wall [R10: Feltrup *et al.*, 2009].

Beside the collective motion of the clusters, there exists as well a transition from a liquidlike to a solidlike state, as revealed by the snapshots shown in Fig. 3.4(a) and (c). Such a transition has been investigated in details by several authors [Scherer *et al.*, 2000; Aumaître *et al.*, 2003]. Using an order parameter derived from the two dimensional Fourier transformation of the snapshots taken with various filling fractions, the transition threshold if found to be  $\phi_c = 0.64 \pm 0.01$  (Fig. 3.4).

### 3.3 Wet granular dynamics under horizontal agitations

In contrast to the critical area fraction of  $\approx 0.64$  for dry granular monolayers shown above (Section 3.2), a dramatically different behaviour arises if the particles are slightly wet.

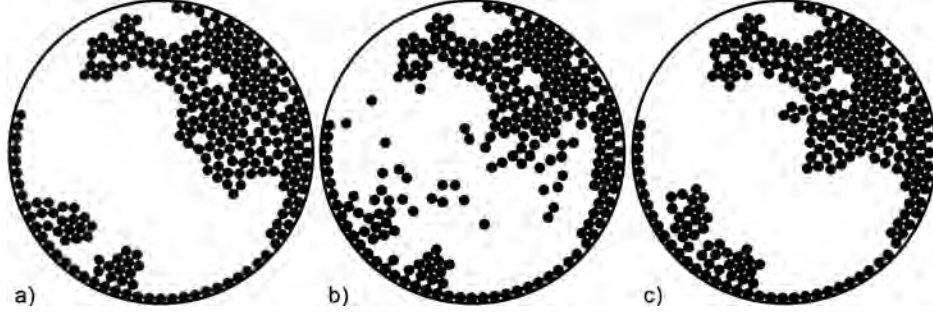


**Figure 3.5:** Sequential snapshots showing an intermittent sublimation event of wet spheres with a liquid content  $W = 1\%$  under horizontal swirling motion with  $f = 1.67$  Hz and  $a = 1.59$  cm. a), b) and c) are taken before, during and after the event correspondingly. The swirling motion is in the clockwise direction. Note that wet particles self-assemble themselves into a crystalline state already at the area fraction of 28%, owing to the strong cohesive force. Images adapted from [R7: Huang *et al.*, 2010].

As shown in Fig. 3.5, hexagonal lattice readily appears at a global area fraction of 28% under a similar driving condition to the dry case shown in Fig. 3.4, owing to the cohesive force stemming from the capillary bridges formed between adjacent particles. Moreover, the clusters formed are driven to the boundary of the container by the inertial force and tend to be attached there. Such a condensed state can be stable over many periods of swirling motions, with occasional sublimation processes. As shown in Fig. 3.5 (b), the ‘gasified’ particles during the sublimation process effectively reshape the resting solidlike phase via impacts. This behaviour differs from the corresponding dry granular matter, where energy injection through collisions with the container walls is comparably well distributed and dissipated through collisions everywhere in the sample. Here, the energy injected is much more localized to a few particles capable of overcoming the energy scale set by the capillary bridges.

#### 3.3.1 Surface melting under swirling motion

In this section, I will show that a different dynamical behaviour, namely surface melting, arises if the cohesion from the container wall is suppressed. Technically, this is done by replacing the glass container with PTFE. Because the contact angle of water on PTFE is larger than  $90^\circ$  (see Section 2.4), the cohesive force between the particles and the container wall is dramatically reduced. Consequently, the formation of free standing wet granular crystals is favoured.

As demonstrated in Fig. 3.6, wet spheres tend to organize themselves into a crystalline state with a perfectly hexagonal packing. Depending on the ramping rate of the agitation strength, states with defects may also arise. There are two time scales associated with such a ‘crystallization’ process: In a rather short time scale (few seconds), initially isolated particles merge with each other into small assemblies. The percent-

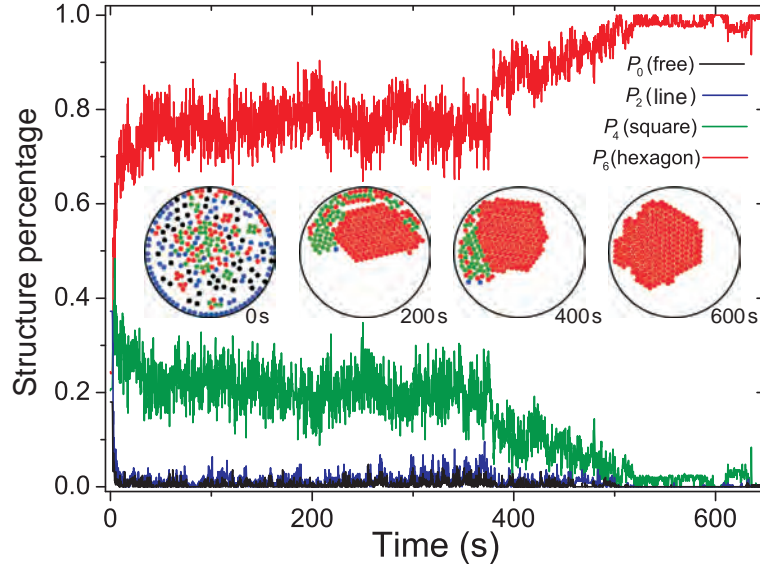


**Figure 3.6:** Initialization process of a wet granular crystal, represented by the time evolution of the percentage for a particle to be free ( $P_0$ ), or in a hexagonal ( $P_6$ ), square ( $P_4$ ), line ( $P_2$ ) structure. Insets are sample images with particles color coded according to their local structures: Free particles with black; Line, square, hexagonal structures with blue, olive and red correspondingly.

age of particles being free or in a line structure drops dramatically to 0, indicating a strong tendency of clustering. As a consequence, the percentage of particles falling into a hexagonal structure ( $P_6$ ) grows substantially to more than 60%. Here the local structures of the particles are characterized with bond orientational order parameters (see R1: May *et al.*, [2013] and references therein for details). In a relatively longer time scale (hundreds of seconds), those assemblies merge into a single cluster deforming continuously under swirling, accompanied with large fluctuations of various structure factors. The final crystalline state (see snapshot taken at 600 s) formed is considered to be a steady state in such a non-equilibrium system, as further collisions with the container do not lead to structure changes.

Melting of such a wet granular ‘crystal’ (Fig. 3.7) with the growth of  $f$  demonstrates an abrupt transition from an amorphous to a surface melting state with a *premelting* ‘liquid’ film covering the ‘crystalline’ core [R1: May *et al.*, 2013]. Such a striking similarity to surface melting observed frequently in equilibrium systems such as the melting of ice [Dash *et al.*, 2006] triggers again the question of how well can our knowledge on equilibrium systems be extended to the widespread non-equilibrium systems. Moreover, the threshold is found to be insensitive to the step size (down to  $6.2 \cdot 10^{-4}$  Hz) and the waiting time (down to 1 minute) of the control parameter  $f$  variations, thus one can speculate that the steady state of such a dissipative system is independent on the time scale imposed by the way of driving.

Four states, including the abrupt transition into the surface melting state, can be identified in the melting process [R1: May *et al.*, 2013]: (i) A state with a perfectly hexagonal structure at low agitation strength. Note that the ‘crystal’ moves around collectively in the co-moving frame with its internal structure kept stable. (ii) An amorphous state with ‘cracks’ or voids formed inside, leading to reduced area fraction

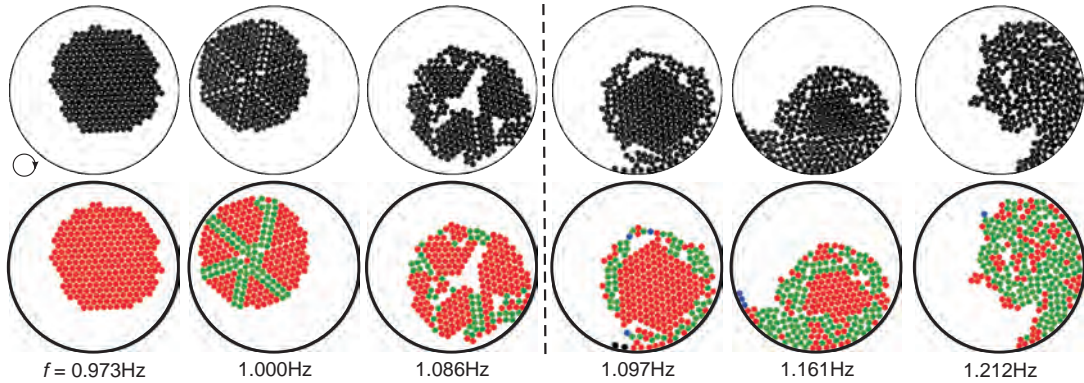


**Figure 3.7:** Melting process of a wet granular crystal as the swirling frequency increases, represented by the snapshots (upper panel) and local structures (lower panel). The particles in the lower panel are color coded according to their local structures as in Fig. 3.6. The gray dash line corresponds to the start of surface melting. The container swirls in the clockwise direction. Figure adapted from [R1: May *et al.*, 2013].

and associated plastic deformation upon impacts with the container wall. Note that the enhanced energy dissipation at those defects effectively increases the susceptibility for the cluster to deform under normal stress applied by the container. Meanwhile, the shear stress drives the rotation of the cluster along the swirling direction. (iii) A surface melting state with a perfectly hexagonal core surrounded by few liquidlike layers, after the collapse of all voids inside the cluster at a threshold  $f_{th}$ . Further increase of the agitation strength leads to an increase of molten layers, reminiscent to the melting of an ice crystal upon the growth of temperature. An interesting feature associated is the circular shape, which suggests a tendency to reduce its surface energy, i.e., a signature for the existence of an interfacial tension. (iv) A completely molten state where no stable crystalline structure can be found. The cluster evolves into a comma shaped ‘droplet’ moving along the rim of the container in the co-moving frame, evocative of a glass of wine being swirled.

Utilizing bond orientational order parameters, the deviation of the local structure of edge particles can be characterized. It serves as the order parameter to determine the melting transitions. A comparison between increasing and decreasing  $f$  reveals small hysteresis for such a transition, which has been discussed in [R1: May *et al.*, 2013]. Systematic investigations reveal that the surface melting threshold  $f_{th}$  depends on the agitation amplitude  $a$  and the liquid content  $W$ , which can be understood quantitatively with a model based on the balance between the energy injection  $E_{inj}$  and dissipation  $E_{cb}$  at a single particle level.

The energy injection is considered to be a two step process: Colliding with the container wall provides ‘macroscopic’ collective motion of the cluster, followed by a transfer into the ‘microscopic’ thermal energy through particle-particle interactions inside. As illustrated in Fig. 3.8 (a), a particle on the edge of a cluster has more freedom to roll compared with those in the bulk, due to less restrictions from its neighbours. This difference provides the ‘thermal’ energy for the edge particle  $m(2\pi fak)^2/2$ , with  $m$  its mass and  $k = 1 - v_s/v_b$  the relative velocity difference. The latter is 5/7 for the case that only edge particles roll, and roll without sliding and rolling frictions [Kondic, 1999]. As the second step only occurs without interruptions from the wall, we introduce

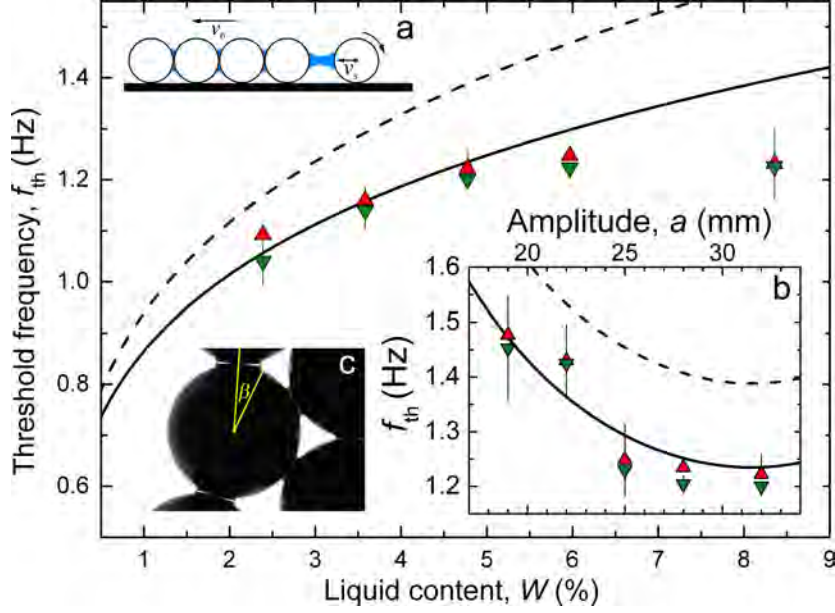


**Figure 3.8:** Dependency of the threshold frequency on the liquid content and the swirling amplitude (inset b).  $f_{th}$  is measured with the bond orientational order parameter of edge particles. The upper and lower triangles correspond to increasing and decreasing  $f$ .  $a$  and  $W$  are fixed at 31.8 mm and at  $W = 4.77\%$  in the main panel and in b, correspondingly. The dash and solid lines are estimations from the model. Inset a: A sketch illustrating an edge particle rolling away from the bulk.  $v_s$  and  $v_b$  are the velocity of edge, and of the bulk particles in the lab frame. Inset c: A close view of the edge of a crystal with  $W = 2.39\%$ , captured with a microscope.  $\beta$  denotes the half opening angle of a capillary bridge. Figure taken from R1: May *et al.*, [2013].

an additional factor  $\alpha = (D_c - 2a)/(D_c + 2a)$ , the length scale for a particle to move without disturbance from the wall over that for the swirling table (diameter of the container  $D_c$ ) to reach. Thus, the energy injection can be estimated with

$$E_i = \frac{\alpha m}{2} (2\pi f a k)^2. \quad (3.1)$$

On the other hand, the energy dissipation can be estimated with the rupture energy of a capillary bridge  $E_{cb}$  (see Eq. 2.15 in Section 2.2.1). Since the relative velocity of the edge particles rolling away from the bulk is relatively small, the viscous damping term can be neglected here. A balance of the two energy scales gives rise to an analytical form for the melting threshold

$$f_{th} = \frac{0.60}{ka} \left( \frac{\sigma \cos \theta}{2\rho_p R} \cdot \frac{D + 2a}{D - 2a} \right)^{1/2} \left( \frac{W}{N} \right)^{1/4}, \quad (3.2)$$

where  $N$  is the mean coordination number of the particles.

Predictions from this formula are shown as dash lines in Fig. 3.8, with parameters measured experimentally. It demonstrates qualitatively the trend of  $f_{th}$  and quantitatively the correct order of magnitude. Quantitative disagreement to the experimental data is not surprising, because, as discussed in Section 2.2.1, Eq. 2.15 is an approximation that has an error growing with  $W$ . A more accurate estimation of  $E_{cb}$  from

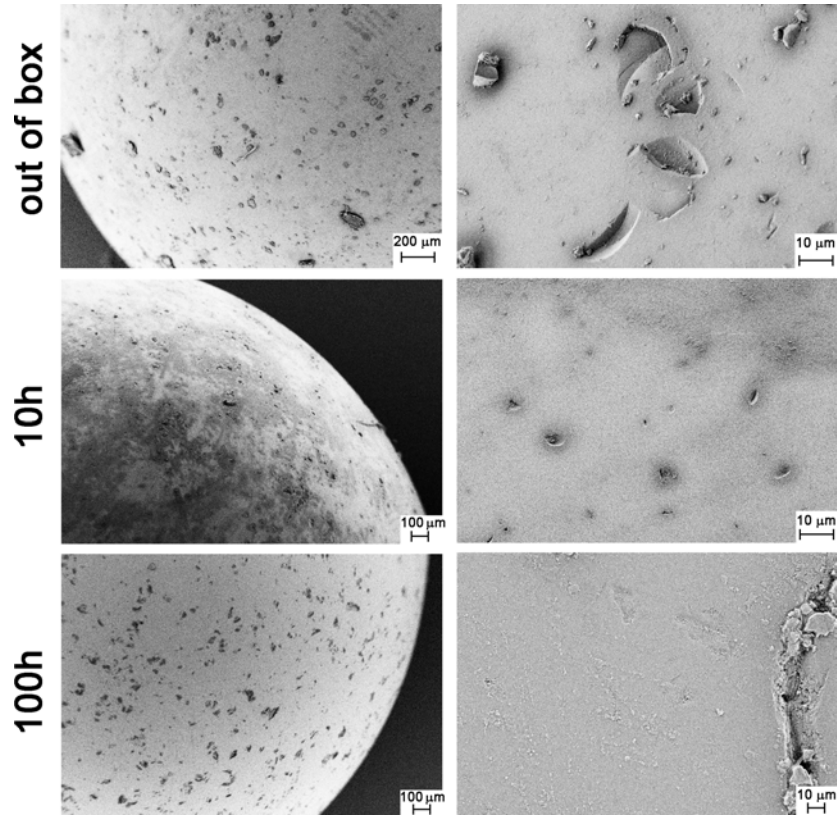


**Figure 3.9:** Scanning electron microscope (Leo 1530) images of a glass bead (Sili beads, type P) used in the experiment. Upper, middle and lower panels correspond to beads directly out of the box, and after 10 or 100 hours of continuous swirling. Left and right columns are from different resolution.

a numerical integration of a more exact force law (appendix of Willett *et al.* [2000]), which is accurate within 3% for  $W$  up to 6.58%, yields a much better comparison to the experimental results, as the solid curves demonstrate. The limit for such a more accurate estimation corresponds to the merge of capillary bridges at  $\beta = \pi/6$ . Thus, without any fit parameter, the model proposed here can describe fairly well the melting threshold, provided that the system is in a pendular state [R1: May *et al.*, 2013].

Such a success in characterizing the melting threshold demonstrates that a detailed knowledge on the interactions between particles at a ‘microscopic’ level is essential. Actually not only the wetting liquid, but also the surface properties of the particles will influence the collective behaviour. As the scanning electron microscope (SEM) images show in Fig. 3.9, particles become more and more smooth after swirling, owing to the frequent polishing between adjacent particles that are closely bound with each other on the merits of capillary bridges formed. Such a smoothing process is found to influence the melting threshold: It decays systematically with experimental runs and becomes stable only after at least 80 hours of continuous swirling. Moreover, the condensation of liquid on the container lid has to be minimized in order to obtain reproducible results, because it influences the liquid content  $W$ . This is achieved through keeping the container lid slightly warmer than the rest part of the container [Wild, 2013]. These examples on the care one has to take for the investigations of granular matter manifest

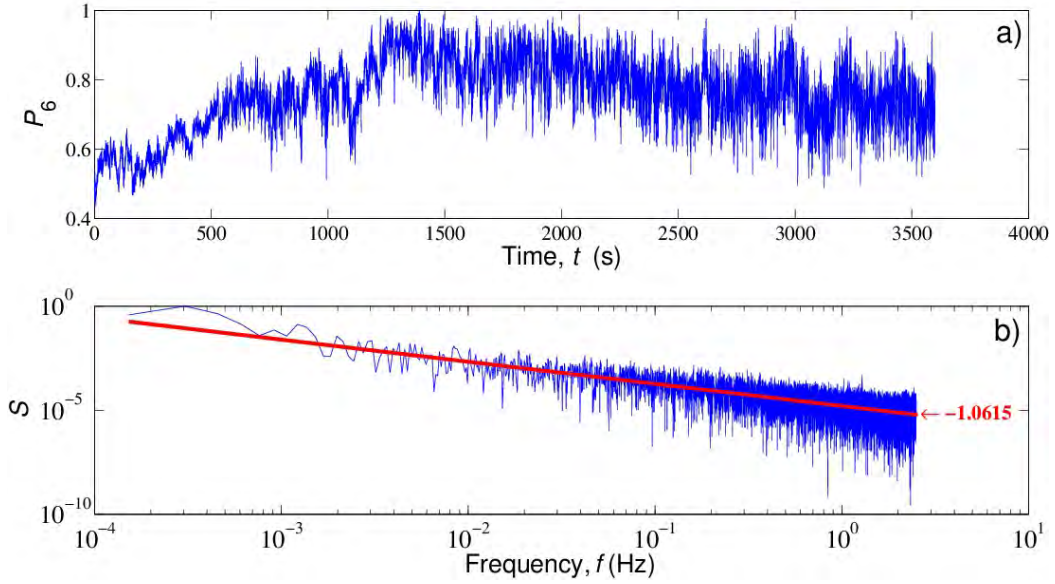


**Figure 3.10:** a) Fluctuations of  $P_6$  at a frequency close to  $f_{\text{th}}$ , where switching between the amorphous and surface melting states can be observed. b) A representation of such fluctuations demonstrate a  $1/f$  noise, a characteristic feature of systems with self-organized criticality [Bak, 1999].

what P. G. deGennes, a pioneer of soft matter physics, mentioned [Duran, 2000],

“The physics of granulars may not require costly hardware,  
but it demands enormous care.”

As melting starts, strong fluctuations of the structure factor  $P_6$  are observed (Fig. 3.10). Such a behaviour corresponds to a frequent switching between a more ‘fragile’ state with loose accumulation of small rigid clusters, and the surface melting state. This strong fluctuations presumably arise from the non-equilibrium nature of the system: The balance between the energy injection and dissipation, which determines its steady state, is not homogeneous in both time and space. An interesting feature, namely a  $1/f$  decay, arises if the fluctuation is viewed from the frequency domain. Such a  $1/f$  noise is a robust and still mysterious phenomenon widely existing in nature, ranging from the blinking of stars to the occurrence of earthquakes as well as avalanches of a pile of sand at a much smaller length scale [Bak, 1999; Mandelbrot, 2002; Milotti, 2002]. In 1987, Bak *et al.* proposed that such a noise can be explained with self-organized criticality: A critical state that a system naturally evolves into without detailed specifications of the initial condition, and such a critical state (attractor) is very susceptible to small perturbations, i.e. small events may trigger large events. Consider a pile of sand: It has a certain angle of repose that the particles will evolve into, and small rearrangements of particles or even force connections in between may trigger larger events, i.e. avalanches. From this perspective, the onset of avalanches for a pile of sand has been extensively investigated in the past [Bak *et al.*, 1987, 1988; Jaeger *et al.*, 1989; Held *et al.*, 1990; Nagel, 1992; Frette *et al.*, 1996; Buchholtz & Poeschel, 1996]. The observation here for the structure fluctuations of a wet granular ‘crystal’ demonstrates again such a

ubiquity. More preliminary experimental runs suggest that this type of noise starts to occur already in the ‘crack’ forming region at a relatively weak agitation strength. It indicates that large events such as avalanches or voids collapse associated with the melting transitions may originate from critical states at a more ‘microscopic’ level, such as the local density or structure changes. Further investigations on the scaling laws and possible mechanisms behind are being carried out presently.

### 3.3.2 Clustering under steady shear flow



**Figure 3.11:** Dark polyethylene (PE) spheres at the air-water interface to reduce the level of bromate in Ivanhoe clean water reservoir. Image taken from [Ivanhoe, 2011].

With a different type of driving, namely a steady shear flow, I will demonstrate again in this section that the collective behaviour of a two dimensional wet granular cluster can be traced down to the particle-particle interactions at a ‘microscopic’ level.

Agglomerations of particles or foams trapped at an air-liquid interface are ubiquitous phenomena frequently observed in our daily lives, e.g. cornflakes floating on milk, mosquito eggs floating on a pond or in a glass of champagne, and in various industries such as mining or waste water treatment [Whitesides & Grzybowski, 2002; Wills, 1997]. As an example, Figure 3.11 shows how a layer of dark particles is used to avoid the formation of bromate, a carcinogen that forms when bromide and chlorine react with sunlight, in Ivanhoe reservoir that serves over half a million inhabitants in Los Angeles Ivanhoe [2011].

For colloidal particles at the interface, interactions with each other through van der Waals interactions and surface charges in the presence of electrolytes in the bulk liquid will dominate [Robinson & Earnshaw, 1992; Pieranski, 1980; Nikolaidis *et al.*, 2002; Manoharan *et al.*, 2003; Lu *et al.*, 2006]. For particles with a diameter larger than tens of microns, i.e. within the granular realm, the capillary force induced by the distorted air-liquid interface starts to take effect [Stamou *et al.*, 2000; Hoekstra *et al.*, 2003; Vassileva

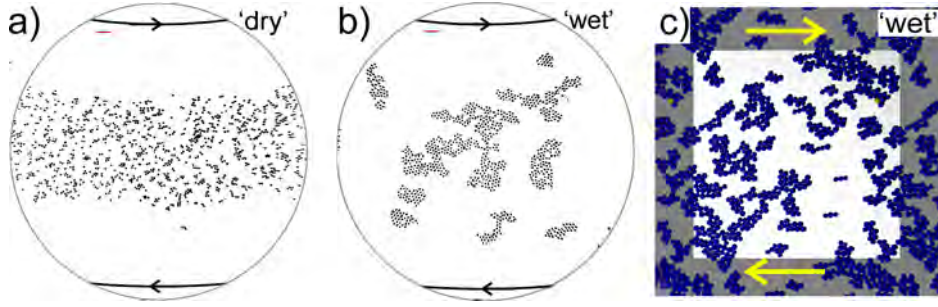


**Figure 3.12:** A comparison between particles trapped at the air-glycerol interface without (a) and with (b) the additional oil phase, i.e., a comparison between ‘dry’ and ‘wet’ granular clusters. The dark curves correspond to the inner and outer cells of the Couette device, and arrows denote the rotation direction. Scale bar length is 1 mm. (c) A snapshot taken from discrete element method (DEM) simulations for wet particles (see text for a short description of the model, image courtesy of M. Brinkmann). Experimental snapshots are adapted from R5: Huang *et al.*, [2012].

*et al.*, 2005]. As an example, particles with a diameter around  $100 \mu\text{m}$  will experience an attractive force of this type on the level of  $nN$ , sufficient to drive aggregations.

Here, I will show that the strength of capillary interactions can drastically be enhanced by adding a second immiscible liquid to the particles [R5: Huang *et al.*, 2012], which is believed to be an analogue of the gelation described for pickering emulsions by Koos & Willenbacher [2011], and to shed light on the stability mechanism of bi-continuous interfacially jammed emulsion gels (bijels) [Stratford *et al.*, 2005; Cates & Clegg, 2008].

To prepare wet granular clusters at an air-liquid interface, glass beads employed are treated initially to allow their centers of mass slightly above the air-liquid interface. This will consequently facilitate the formation of capillary bridges. In order to create a monolayer of ‘wet’ particles, a solution of silicone oil in hexane is then applied to the interface. Initially particles rearrange themselves into a monolayer owing to the lubrication of the additional oil phase. Driven by the evaporation front of hexane, a compact ‘wet’ granular cluster is formed. By control the amount of oil added, one can assemble compact ‘wet’ granular crystals with particles interact mutually through the formation of capillary bridges (see R5: Huang *et al.*, [2012] for more details).

Due to the high viscosity of the subphase, thermal energy will not influence the dynamics of the clusters. Instead, steady shear flow is employed to drive the wet granular clusters. As the snapshots in Fig. 3.12 indicate, dramatically different behaviour is found for ‘wet’ particles in comparison to the ‘dry’ ones. Starting from the evaporation driven compact state, ‘dry’ particles interact with each other through hard core repulsions, leading to a slight dilation from the central region where the initial ‘crystalline’ structures are formed. After that stage, the particles will follow the steady shear profile and no more interactions could be observed within the observation period. For the ‘wet’ case, large, persisting clusters are formed under continuous shear flow, which rotate around their center of mass, collide, merge, deform or break into several parts. Such a difference calls a detailed understanding on how cohesion plays the role here.

To explore the essential role that cohesion takes, the dynamics of ‘wet’ particles in a linear shear profile was also numerically simulated applying a two dimensional

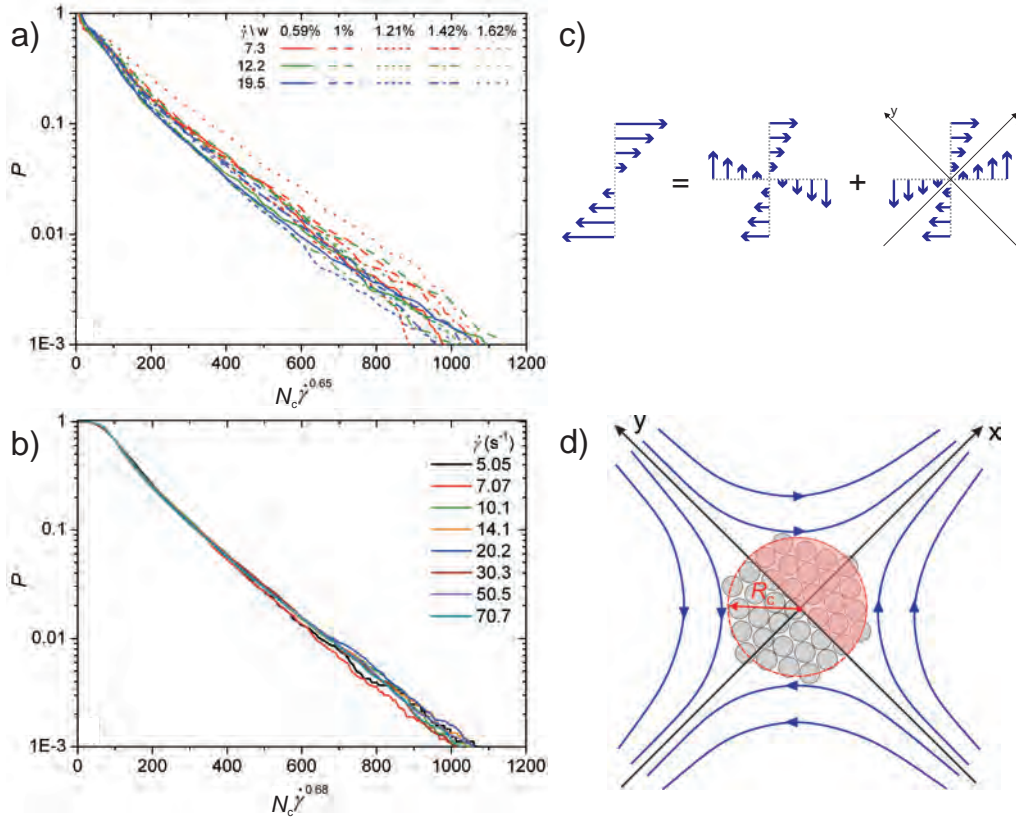


**Figure 3.13:** Cumulative cluster size distribution  $P$ , the probability to find a cluster out of  $N_c$  or more particles, as a function of the rescaled cluster size  $N_c \dot{\gamma}^j$  from experiments (a) and DEM simulations (b). The exponent  $j$  arises from the scaling of the characteristic size of the cluster  $N_c$  with the shear rate  $\dot{\gamma}$ . (c) shows that any linear shear profile can be decomposed into a rotating and a hyperbolic straining flow field. (d) illustrates the model used to describe the critical exponent  $j$  (see text for more details). The hyperbolic stream lines tend to compress the cluster with an effective radius  $R_c$  along the  $y$  axis and stretch it along the  $x$  axis. Figures taken from R5: Huang *et al.*, [2012].

discrete-element model (DEM) [R5: Huang *et al.*, 2012]. The model considers three forces acting on the particle: Elastically repulsive force, capillary and viscous drag forces. After solve the Newton's equation of motion, the mobility of the particles can be obtained. As shown in Fig. 3.12 (c), such a simplified model leads to the clustering of particles reminiscent to the experiments. As the cluster size distributions shown in Fig. 3.13 (a) and (b) suggest, such a model is capable of reproducing the cumulative cluster size distribution: It decays exponentially with the rescaled cluster size  $N_c \dot{\gamma}^j$ . Such a scaling suggests that the larger the shear rate, the faster the decay rate. This could be understood since the viscous drag force grows with the shear rate. Step further, I will show that the balance between the viscous drag force and the capillary force determines the scaling exponent  $j$ .

As shown in Fig. 3.13 (c), any linear shear profile can be decomposed into a hyperbolic strain flow and a rotation. It is the stretching component from the former part contribute to the break of the cluster, as sketched in Fig. 3.13 (d). For such a

cluster shape, integrating the Stokes' drag force acting on each particles in the region shaded with red, one could obtain the total drag force  $F^{(d)}$  exerted on the cluster along the central cutting line  $x = 0$ :

$$F^{(d)} \propto \mu \phi \dot{\gamma} R_g^3 / R, \quad (3.3)$$

where  $\phi \equiv N_c R^2 / R_g^2 \propto N_c^{1-2/D_f}$  is the area fraction of particles in the cluster, and  $R_g$  corresponds to the gyration radius of the cluster. Here  $D_f$  is the fractal dimension of the cluster.

On the other hand, the total capillary force  $F^{(c)}$  acting along a cut  $x = 0$  into the direction of the  $x$  axis can be estimated, as a first approximation 2.11 with

$$F^{(c)} \propto n \sigma R, \quad (3.4)$$

where  $n$  is the number of capillary bridges in a cut along the line  $x = 0$ . There are two limiting cases for the breaking of clusters: (i) A compact disk like cluster as illustrated in Fig. 3.13 (d), with a corresponding  $n \propto \phi R_g R$ , (ii) A more fractal structure built with a hierarchy of rigid sub-clusters with a characteristic size, i.e. constant  $n$ . Consequently, the scaling of the cumulative cluster size with the shear rate is expected to be

$$\frac{D_f}{1 + D_f} \leq j \leq \frac{D_f}{2}, \quad (3.5)$$

where the fractal dimension of the cluster  $D_f$  is found to be  $\approx 1.6$  for both experiments and DEM simulations [R5: Huang *et al.*, 2012]. Therefore, we can predict the exponent to be  $0.6 \leq j \leq 0.8$ , which captures the measured value from both experiments  $0.65 \pm 0.06$  and DEM simulations  $0.68 \pm 0.02$ . Moreover, it is remarkable that the values of both experiments and the DEM simulations lie closer to the lower bound that corresponds to the hierarchical structure, which agrees with the qualitative analysis based on the snapshot shown in Fig. 3.12 (b). Note that the model for cluster size distribution is based on the force balance, which differs from the melting transition shown in the above Section 3.3.1, this could be attribute to the fact that both viscous drag force and the capillary force are acting at the same time during the rupture event.

At a larger area fraction  $\phi = 23\%$ , Fig. 3.14 demonstrates the percolation of the clusters after a quench of the shear rate. Such a tendency for the particle network to percolate, i.e. 'gelation', with the presence of the secondary wetting liquid is a robust phenomena found in vast number of liquid-particle systems [Koos & Willenbacher,

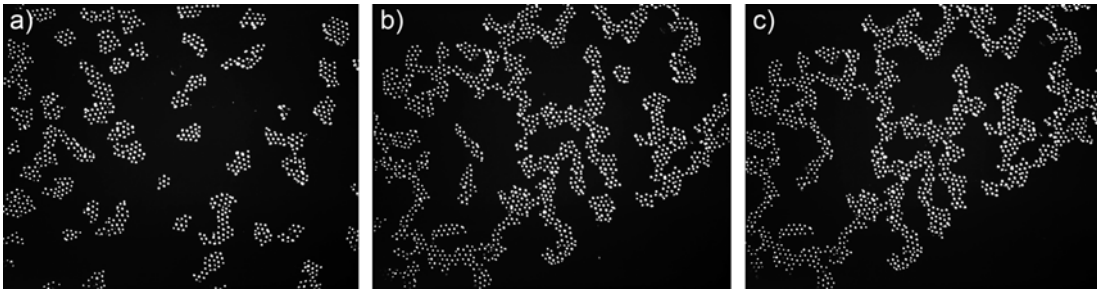


**Figure 3.14:** Time sequence ( $t=0, 20, 40$  min) of the aggregation of clusters after switching off the shear rate from  $\dot{\gamma} = 48.8 \text{ s}^{-1}$ . The global area fraction is  $\phi = 23\%$ .

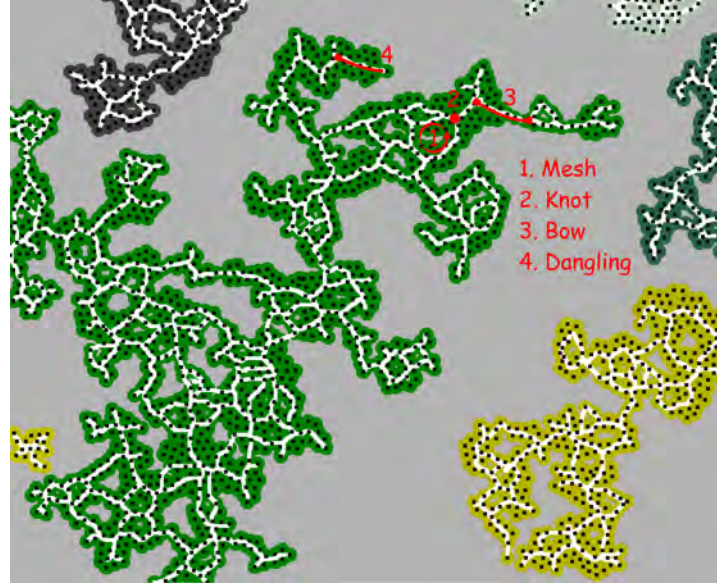


**Figure 3.15:** Network representative of shearing ‘wet’ granular clusters at an area fraction close to percolation transition. Based on the positions of particles detected (black dots), the network structure of the clusters formed (white lines) can be obtained. Various clusters are coded with different colors. How does the collective behaviour of the clusters close to the percolation transition depend on the dynamics of the network morphology is a question to be addressed in such a ‘wet’ granular model system.

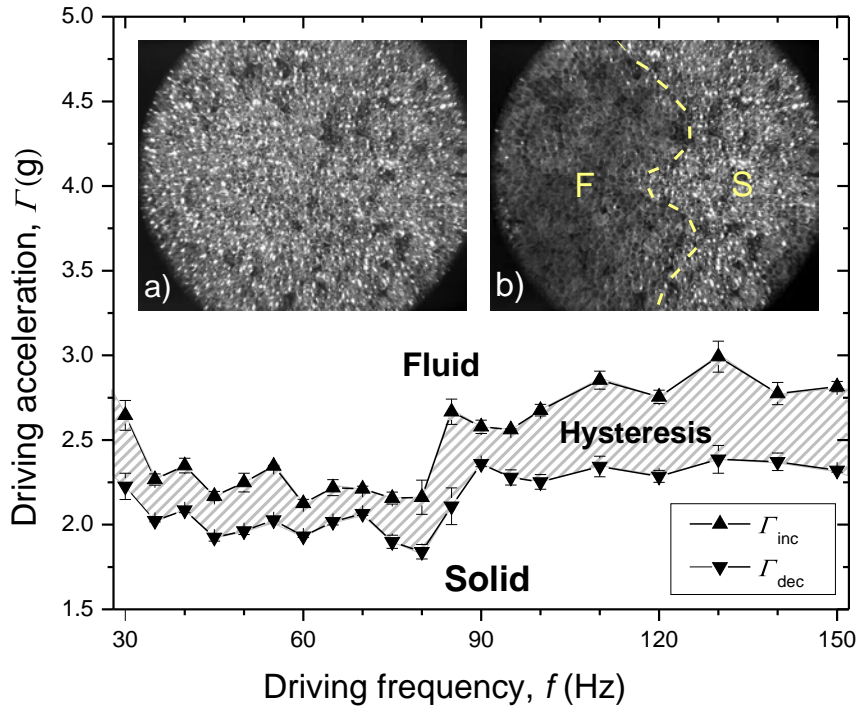
2011]. The two dimensional system focusing here has the advantage that not only the bulk properties such as percolation transition threshold, or rheological behaviour [Edwards & Brenner, 1991], can be measured quantitatively, but also the dynamics of the ‘microscopic’ structure can be characterized in real time with the positions of particles found. More importantly, as the above analysis of the clustering of particles has already demonstrated, the connections between ‘macro-’ and ‘microscopic’ worlds will help to elucidate crucial properties that dominate the rheological behaviour. Therefore, further investigations on such a system will focus on the percolation transition, rheology of two dimensional ‘wet’ granular gels, and the dynamics of network structure close to the percolation transition.

Figure 3.15 corresponds to one possible way to characterize the structures formed by ‘wet’ particles at the interface: By a ‘thinning’ process, the rigid backbone of the clusters can be distinguished as the white lines. As the clusters deform under the shear flow, a frequent change of the network structure is expected. One important question we can address with such a characterization is: From a statistical point of view, what type of bonds dominates the rigidity of the ‘gels’ formed? The rigidity of such cohesive network structure could be a counterpart for the force chains network in a dry pile of sand that determines when and where avalanches happen [Vanel *et al.*, 1999; Howell *et al.*, 1999; Geng *et al.*, 2001; Bi *et al.*, 2011], thus shed light on the jamming phase diagram proposed to unify thermal and athermal systems [Liu & Nagel, 1998].

### 3.4 Wet granular dynamics under vertical agitations

As the most direct way to overcome gravity, vertical agitations are frequently used to drive granular matter (see e.g. Iveson *et al.* [2001]). In this section, we focus on the dynamical behaviour of wet granular matter under vertical agitations. Due to the additional cohesive force arising from the formation of capillary bridges, typically being orders of magnitude larger than the gravity of particles (see Chap. 1), strong agitations with a dimensionless acceleration  $\Gamma$  up to 80 are necessary to effectively ‘thermalize’ multiple layers of wet granular matter into a gaslike state. In this section, phase behaviour as well as the associated scaling laws in such a quasi-two-dimensional system will be presented. In particular, I will demonstrate again how ‘microscopic’ time, length and energy scales influence the collective behaviour of agitated wet granular matter.

#### 3.4.1 Melting



**Figure 3.16:** Melting transition for 3~4 layers of wet transparent glass beads under vertical agitations measured through visual inspections on the mobility of particles on the top layers. Insets are obtained through a minimization of consequent 500 synchronized snapshots below a) and above b) the melting threshold, where the bright spots correspond to the reflections of the illuminating light by the glass beads. Note that the fluidized region (F) in b) is darker and blurrier in comparison to the solidlike (S) region, because of the particle movements.

As learned from monolayer systems, agitated wet granular ‘crystals’ tend to melt from the surface layers, therefore we can determine the melting threshold via visual inspections on the mobility of particles on the top layers as the agitation strength varies experimentally. A closer view of such a transition, as shown in the insets (a) and (b) of Fig. 3.16, suggests that melting in the top layers is heterogeneous, with

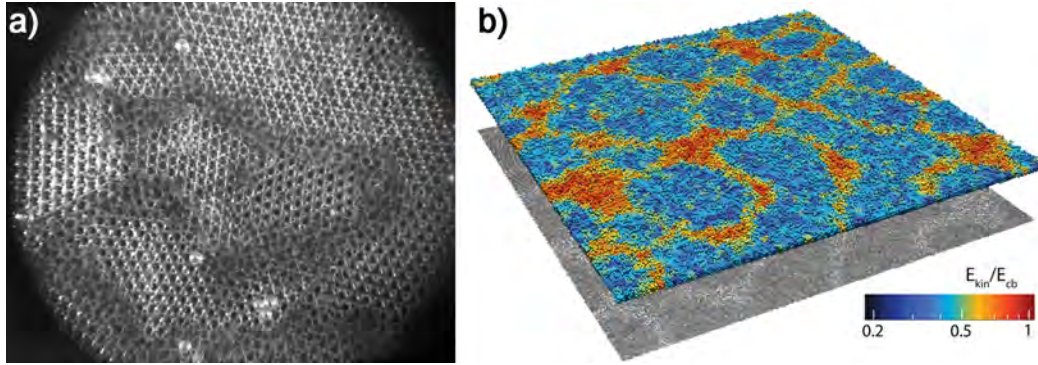


**Figure 3.17:** a) Melting of 3~4 layers of slightly wet glass beads of diameter 1.2 mm under vertical agitations with  $f = 150$  Hz and  $\Gamma = 7.42$ . The image is obtained by minimizing continuous 50 snapshots taken at a fixed phase of each vibration cycle, thus particles mobilized are blurred. b) A snapshot from MD simulations [Roeller, 2010] for a comparable configurations, with particles color coded by their kinetic energy  $E_{\text{kin}}$  rescaled by the rupture energy of a single capillary bridge  $E_{\text{cb}}$ , the intensity of the shadow indicates the local density of particles. Simulation performed by K. Röller.

the possibility of having part of the layer in a molten state while the other part still being rigid. Moreover, visual inspections also show that the mobility of particles in the molten region can be dramatically different: (i) A few particles, which have only single bonds with the solidlike phase below, may swing around the contact points with their neighbours rapidly. (ii) The threshold detected exhibits hysteresis for all frequencies used, a manifestation of the influence from the hysteretic nature of a single bridge forming and rupturing. (iii) The threshold  $\Gamma$  value exhibits a jump of  $\approx 0.5$  as a threshold frequency  $f_c \approx 80$  Hz is reached.

At a vibration frequency larger than  $f_c$ , a different melting scenario arises: Melting tends to be initiated at the ‘grain’ boundaries, stemming from the formation of ‘crystalline’ structures in this frequency region. The molten regimes coexist with blocks of particles with ‘crystalline’ structures. This observation suggests that the jump of the melting threshold could be due to additional force needed to create defects in a crystal for the system to melt, reminiscent to the convection threshold in the dry system discussed above in Section 3.2. Furthermore, one could understand why the threshold frequency occurs at  $\approx 80$  Hz: It corresponds to a match between the peak-peak agitation amplitude ( $a_{\text{p-p}} = 2\Gamma g / (2\pi f_c^2) \approx 213 \mu\text{m}$ ) and the rupture distance of a capillary bridge ( $s_c \cdot R \approx V_b^{1/3} \approx 210 \mu\text{m}$ ). Such an explanation indicates that smaller enough agitation amplitude will lead to an ordering transition. This type of melting is also found to be in agreement with MD simulations (Fig. 3.17 b). From the energy level of particles provided by the simulations, one clearly distinguishes a different kinetic temperature level between crystalline and molten regions. The kinetic energy level for most particles, even for those in the molten region, is smaller than the rupture energy of single capillary bridge, suggesting that a rupture of capillary bridge is not a precondition for melting.

For such a 3D system, it is helpful to explore the melting process along the agitation direction. Here we use ruby fluorescence to have a qualitative view on the mobility of particles below the top layers. As illustrated in Fig. 3.18, ruby tracers are placed initially at the bottom layer. After shined with green Light-emitting diode (LED) light source, they emit red light, reminiscent to a ruby laser. By putting a proper filter

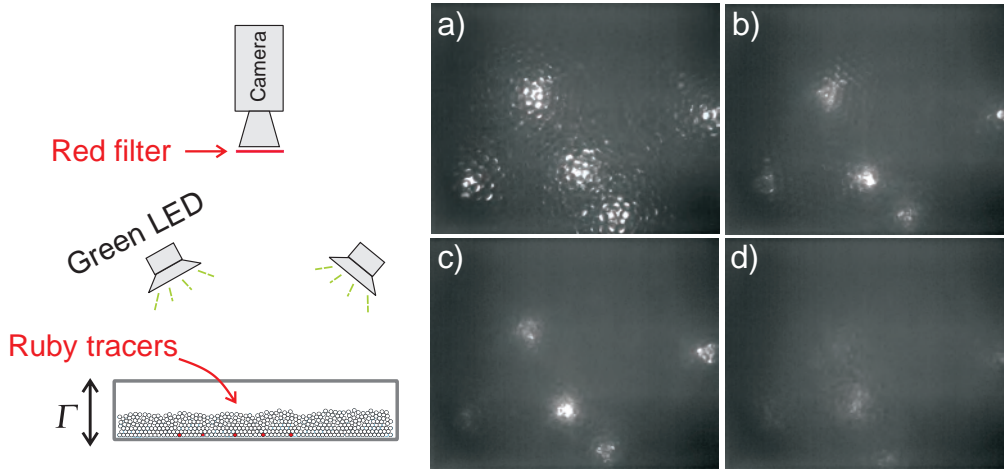


**Figure 3.18:** Surface melting demonstrated by ruby fluorescence. The sketch illustrates the experimental set-up that enables a qualitative characterization of particle mobility below the top layer. Images a) - d) are obtained through the same minimization process as used for Fig. 3.16 in order to identify various molten levels. Corresponding accelerations are  $\Gamma = 2.91$ , 3.56, 4.08 and 4.87. Here only 10 frames are used for each  $\Gamma$  due to the frequent fluctuations of the patterns.

in front of the camera, one obtains only the light emitted from the tracer particles. In another word, those tracers serve as lamps embedded in the granular layer. As a consequence, patterns such as the ones shown in Fig. 3.18 (a) can be detected, which show the positions of the ruby tracers as well as the organizations of particles on top. Qualitatively the mobility of particles above the tracer can be detected from the local variations of the pattern, while that of the tracer can be determined from the collective movement of the pattern.

By varying the driving acceleration step by step and observe the patterns observed, we can qualitatively demonstrate that melting in such a 3D system also starts from the free surface. Utilizing the same minimization process, the mobility of particles at various layers can be distinguished. At  $\Gamma = 2.91$ , particles on top layers are only weakly fluidized, as the sharpness of the minimized image shown in Fig. 3.18 (a) indicates. As  $\Gamma$  increases further to 3.56 (Fig. 3.18 b), particles on the top layers move locally, leading to a slightly blurry top layers. However, the overall position of each pattern is not changing, suggesting that particles at the bottom layers are still immobile. Such a process continues as  $\Gamma$  increases to 4.08 (Fig. 3.18 c), where the particles in the top layers become more mobile. Until finally at  $\Gamma = 4.87$ , the whole image is dark and blurry. Visual inspections on the consequent snapshots taken indicate the patterns are mobile, which indicate that the system melts completely. Such a surface melting scenario has also been confirmed with numerical simulations [Roeller & Herminghaus, 2011]. Moreover, the transition into the completely molten state measured by ruby fluorescence is found to grow linearly with the driving frequency, indicating a threshold agitation velocity and a certain energy scale associated. This agrees with the melting scenario found for agitated dry granular matter discussed in the above Sec. 3.2.

### 3.4.2 Granular ‘gas bubbles’

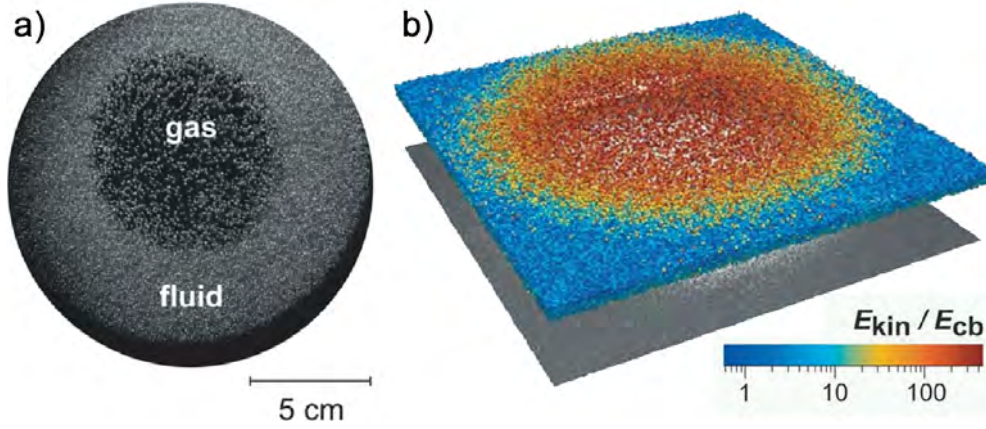


**Figure 3.19:** Snapshots of a wet granular ‘gas bubble’ surrounded by a liquidlike phase from both experiments (a) and MD simulations (b). Such a phase separation is observed in a thin wet granular layer (3~4 layers) under vertical agitations against gravity. In (a), bright spots arise from the light reflected from the glass beads. In (b), the particles are logarithmically color coded by their kinetic energy  $E_{\text{kin}}$  rescaled by the rupture energy of a single capillary bridge  $E_{\text{cb}}$ . It demonstrates the sharp temperature gradient across the phase boundary. Images from R11: Fingerle *et al.*, [2008].

The melting process described above shows the possibility of having lateral inhomogeneities. Such a behaviour is as well true if the acceleration increases further: Wet granular ‘gas bubbles’ tend to nucleate from the surrounding liquid phase, i.e., a phase separation into a coexistence of a liquidlike and a gaslike phases [R11: Fingerle *et al.*, 2008]. Fig. 3.19 shows such an example with a single ‘gas bubble’: The number density of particles in the gaslike region is much less dilute than that in the liquidlike region. Moreover, MD simulations reveal that the kinetic temperature in the gaslike phase is orders of magnitude larger than that in the liquid phase, demonstrating that this system is driven far from thermodynamic equilibrium. Note that MD simulations consider only the energy dissipation from the rupture of capillary bridges (inelastic collisions between particles are ignored). That means only the rupture energy and the rupture distance are parameters controlling the particle-particle interactions. This striking similarity between experiments and the MD simulations based on such a simplified model suggests that the rupture of single capillary bridges plays an important role in the phase separation. For thermally driven molecular or colloidal systems, phase separations in the metastable region of the phase diagram have been extensively discussed in terms of spinodal decompositions (see e.g. Cahn [1965]; Zaccarelli [2007]. In agitated dry granular matter, phase separation has also been found and discussed in detail from a similar perspective [Roeller *et al.*, 2011; Clewett *et al.*, 2012]. Such a similarity across thermal and athermal systems again triggers the question of how well can existing knowledge on thermal system be extended to athermal systems.

Figure 3.20 shows the nucleation and merging dynamics of wet granular ‘gas bubbles’. As a certain threshold acceleration  $\Gamma_{\text{fc}}$  is reached, a ‘gas bubble’ may nucleate from the center or the boundary region of the container. It is found that the former case has a slightly larger threshold than the latter case. After nucleation, it grows with

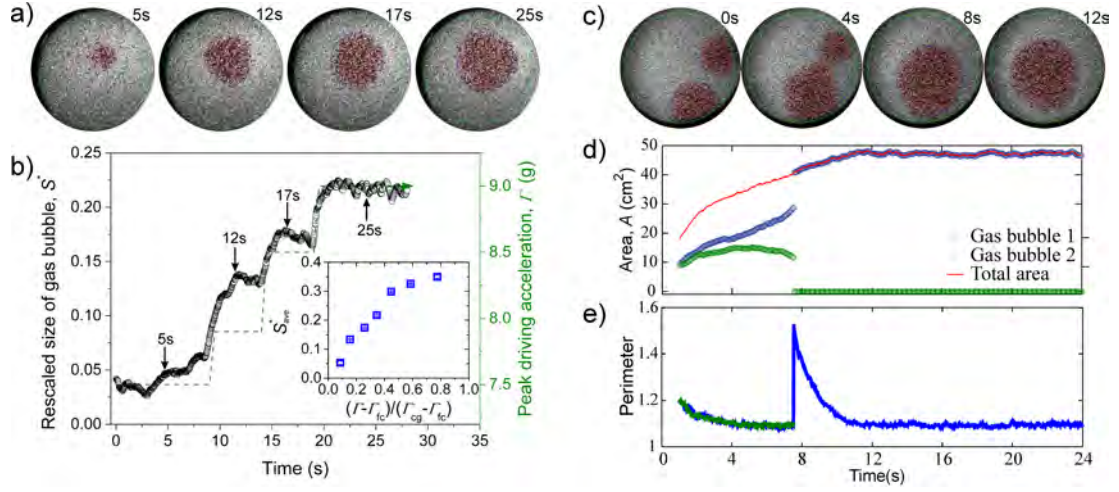


**Figure 3.20:** Left panels: Nucleation of a wet granular ‘gas bubble’ in a thin wet granular layer driven vertically with fixed  $f$  and peak vibration acceleration  $\Gamma$  increasing step by step (dash line in b). a) Images taken at various  $\Gamma$  to demonstrate the growth of the ‘gas bubble’ (highlighted in red). b) The size of the ‘gas bubble’, rescaled by the total area of the container, as a function of time. Inset of b) shows the averaged size  $s_{\text{ave}}^*$  of the ‘gas bubble’ as a function of  $\Gamma$ . The size of a gas bubble  $S^*$  is rescaled by the total area of the container.  $\Gamma_{\text{fc}}$  and  $\Gamma_{\text{cg}}$  are the critical accelerations for the transitions from a fluidlike to the fluid-gas coexistence, and from the fluid-gas coexistence to a gaslike phase correspondingly. Right panels: Merging of two ‘gas bubbles’ at fixed  $f = 50$  Hz and  $\Gamma = 9.45$ . d) and e) correspond to the evolution of the areas and perimeters of the gas bubbles with time. To illustrate the deformation of the phase boundary from a circular shape, the perimeter in e) is rescaled by that of a circle with the same area as the ‘gas bubble’ region found.

fluctuations to a certain size. As  $\Gamma$  increases step by step, the size of the ‘gas bubble’ follows with fluctuations until a saturated  $s^*$  is reached (see inset of Fig. 3.20 b). This is mainly due to the enhanced resistance from the thickening of surrounding fluid phase as ‘gas bubble’ grows. In the limiting case of the layer thickness reaches the top of the container,  $s^*$  saturates. From the snapshots taken at various  $\Gamma$ , the ‘gas bubble’ always tends to have a circular shape, despite of the fluctuations of its size. This behaviour suggests the existence of an interfacial tension, a feature already demonstrated by the surface molten state of a wet granular crystal in 2D (Section 3.3.1). Such a feature is also demonstrated from the merging of two ‘gas bubbles’ (Fig. 3.20 c).

Interestingly, the size evolutions of ‘gas bubbles’ during the merging process also suggest a transport of particles from the smaller to the bigger ‘gas bubbles’ as they are approaching each other. Considering an effective surface tension at the interface, smaller ‘gas bubbles’ will presumably have larger effective ‘Laplace pressure’, which suggests a higher pressure in the small ‘gas bubble’ assuming the same pressure in the liquidlike phase. Thus, as two ‘gas bubbles’ with different sizes are closer enough, transfer of particles from the smaller to the larger ‘gas bubble’ is expected occur. Such a transport arises from the frequent exchange of particles between the gaslike and surrounding liquidlike phases. The effective interfacial tension is as well demonstrated by the rescaled perimeter shown in Fig. 3.20 (e): Merged ‘gas bubble’ tends to relax into a circular shape in a few seconds.

A natural question following the existence of an effective interface tension is wet-

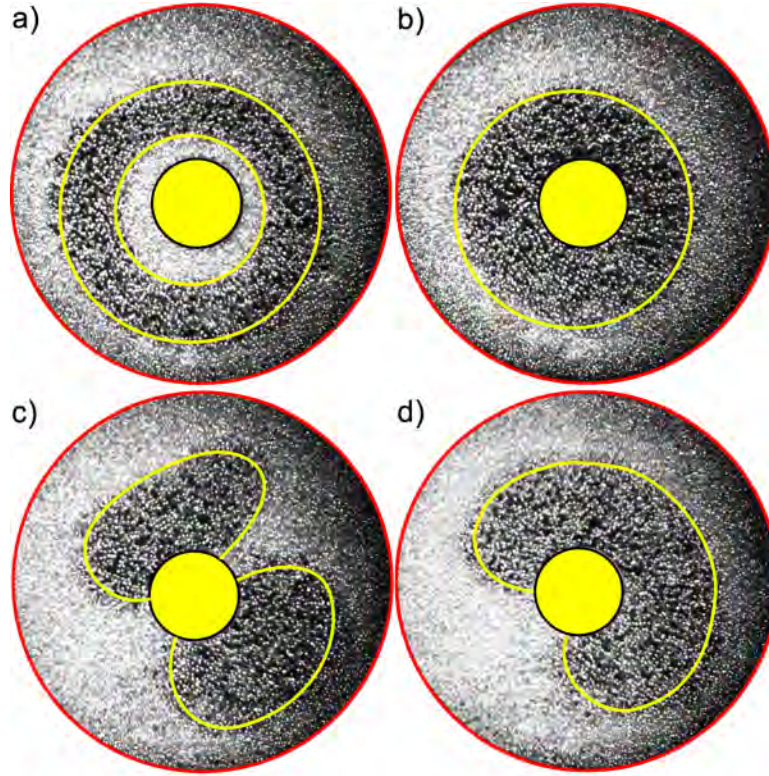


**Figure 3.21:** Interactions between a ‘gas bubble’ and a cylindrical intruder (area covered with yellow) with a diameter of 3 cm placed in the center of the container, which demonstrate an effective ‘contact angle’ for wet granular fluid. Upper panels: A ‘gas bubble’ formed by a quench from a gaslike phase into the phase separation region with  $f = 50$  Hz and  $\Gamma = 12.5$ . a) and b) correspond to snapshots taken at 80 and 220 vibration cycles after the quench. Lower panels: ‘Gas bubbles’ formed by a jump of  $\Gamma$  from a liquidlike phase to the coexistence phase  $\Gamma = 11.6$ . c) and d) correspond to 90 and 160 vibration cycles after the jump. The yellow curves, which highlight the phase boundaries, are guide to the eyes.

tability. With a cylindrical intruder added into the container, the effective wetting properties are explored. The question of whether a wet granular liquid wets or not the intruder turns out to be not trivial and strongly relies on the initial states of the experiments: A quench from a gaslike state into the coexistence phase leads to the shrinking of an initially large ‘gas bubble’ to a steady state with the intruder embedded (Fig. 3.21 b). In the initial stage, a liquidlike region tends to ‘wet’ the intruder (Fig. 3.21 a). However, it vaporizes away in the steady state (Fig. 3.21 b). According to the Kelvin equation, such a behaviour can be understood from the vapor pressure gradient in the intermediate gaslike region along the radial direction [Herminghaus, 2013]. On the contrary, a jump from a liquidlike into a coexistence state leads to the nucleation of multiple ‘gas bubbles’ (Fig. 3.21 c), preferably close to the intruder. They will eventually merge into a single one attached to the intruder with a contact angle close to  $90^\circ$  (Fig. 3.21 d).

Figure 3.22 (a) shows the change of the gas bubble size with  $\Gamma$ . In contrast to the sudden jump of  $s^*$  as  $\Gamma$  goes beyond  $\Gamma_{fc}$ , a continuous decrease of the ‘gas bubble’ size is found as  $\Gamma$  decreases. Such a hysteretic behaviour can be treated as a magnification of the hysteresis from the rupture of single capillary bridges. Thus the fact that the

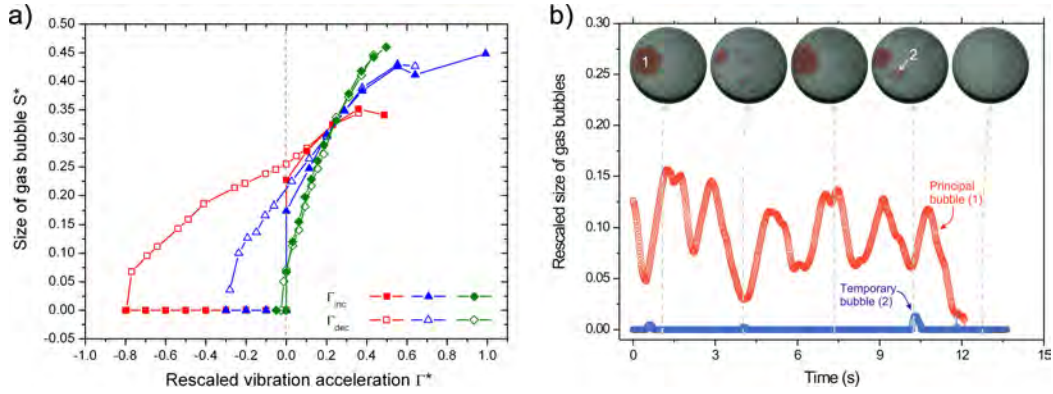


**Figure 3.22:** a) Hysteresis of the size of ‘gas bubbles’ across the transition from a fluidlike to a fluid-gas coexistence region. The size of the ‘gas bubble’  $S^*$  and  $\Gamma^*$  are defined the same as in Fig. 3.20 with  $\Gamma_{fc}$  and  $\Gamma_{cg}$  measured by increasing  $\Gamma$  step by step. Data obtained by increasing and decreasing  $\Gamma$  are shown by solid and open symbols separately. Square, upper triangle and diamond correspond to  $d = 1$  mm,  $f = 50$  Hz;  $d = 1.2$  mm,  $f = 100$  Hz and  $d = 1.5$  mm,  $f = 100$  Hz. b) Size fluctuation of a ‘gas bubble’ with  $f = 85$  Hz and  $\Gamma = 24.1$ , which is close to  $\Gamma_{fc} = 27$  above which a stable ‘gas bubble’ is observed. As time evolves, size of the principle ‘gas bubble 1’ decreases with strong fluctuations until vanishes. Sometimes temporary ‘gas bubble 2’ nucleates as the size of the principal ‘gas bubble’ fluctuates to its minimum.

hysteresis region being larger for small particles could be attributed to the enhanced total rupture energy for the nucleation of the ‘gas bubble’. Note that although the rupture energy decreases with particle radius ( $\propto \sqrt{R}$ ), the total number of bridges to break for the nucleation of a ‘gas bubble’ ( $\propto R^{-3}$ ) increases as  $R$  decreases.

In the hysteretic regime of 1 mm particles and  $f > 85$  Hz, the size of ‘gas bubble’ fluctuates strongly. Fig. 3.22 (b) shows such fluctuations for transient ‘gas bubbles’ observed in the hysteresis region, together with snapshots taken at various time. The principle ‘gas bubble’ fluctuates at an amplitude of around half of its mean value and a frequency of about 0.5 Hz. The shrinking of the principle ‘gas bubble’ is normally accompanied with nucleation of one or more small temporary ‘gas bubbles’ at other locations in the surrounding granular fluid. The competition between newly nucleated ‘gas bubbles’ and the principle ‘gas bubble’ leads to the strong fluctuations. The fluctuation region is not in a steady state, because normally after tens of seconds, all the ‘gas bubbles’ vanish and the system enters a complete liquidlike state. Such fluctuations are found to be much stronger for small particles in comparison to larger ones, which can be speculated from the level of energy barrier generated after phase separation. The nucleation of a ‘gas bubble’ can be considered as a symmetry breaking process [R11: Fingerle *et al.*, 2008]. In the metastable region, the net power injection has two stable zero points: Either strongly dissipated through the rapid collisions (high  $E_{diss}$ ) in the dilute gaslike phase, or weakly dissipated through particle-particle interactions without frequent rupture of capillary bridges. One can speculate that the barrier in between determines the level of fluctuations, i.e. smaller particles with larger number of layers give rise to stronger fluctuations.

### 3.4.3 Phase diagram and scaling laws

In order to have an overview of the phase behaviour of agitated wet granular matter, transitions between the solidlike, liquidlike and gaslike states of agitated wet spheres are measured systematically through a variation of the agitation acceleration at fixed frequencies [R9: Huang *et al.*, 2009b].

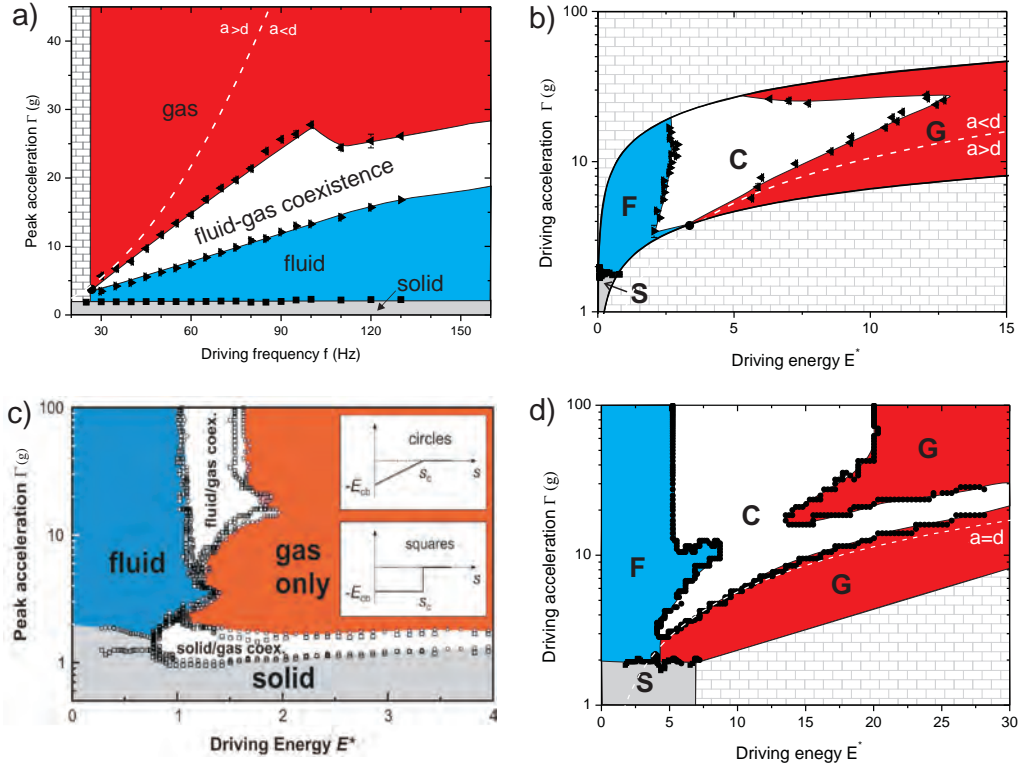


**Figure 3.23:** Phase diagrams of water wetting glass spheres with diameter  $d = 1.5$  mm and liquid content  $W = 1\%$  in  $\Gamma - f$  (a) and  $\Gamma - E^*$  (b) planes, where  $E^* = mv_p^2/(2E_{cb})$  corresponds to the maximum kinetic energy a particle with mass  $m$  can obtain from the vibration plate ( $v_p$  being the peak vibration velocity) rescaled by the rupture energy of a single capillary bridge  $E_{cb}$ . The regions covered with brick patterns are unexplored due to the limitation of the apparatus. The solid black dot corresponds to the converging point of the F-C and C-G transition lines. Dash line indicates  $a = d = 1.5$  mm, where  $a$  is the vibration amplitude. c) and d) correspond to phase diagrams from MD simulations with 1200 particles in two dimensions for the elastic and inelastic cases, respectively. The restitution coefficient is fixed at  $e_{pp} = 0.8$  for particle-particle collisions, and  $e_{pw} = 1$  for particle-wall collisions. Insets of c) show the hysteretic interaction potentials chosen (dotted: approach and solid: retract). Regions color coded with gray, blue, white and red correspond to solidlik (S), fluidlik (F), fluid-gas coexistence (C) and gaslike (G) phases. Figures a), b), d) adapted from R9: Huang *et al.*, [2009b], and c) from R11: Fingerle *et al.*, [2008].

As the phase diagram presented in Fig. 3.23 (a) shows, the transition from a solidlike (S) phase to a fluidlike (F) phase occurs at a constant  $\Gamma \approx 2$ , slightly larger than the typical value 1.2 found for dry granular matter (see Section 3.2), demonstrating the influence from the capillary force [Scheel *et al.*, 2004]. Because  $\Gamma$  determines the mean

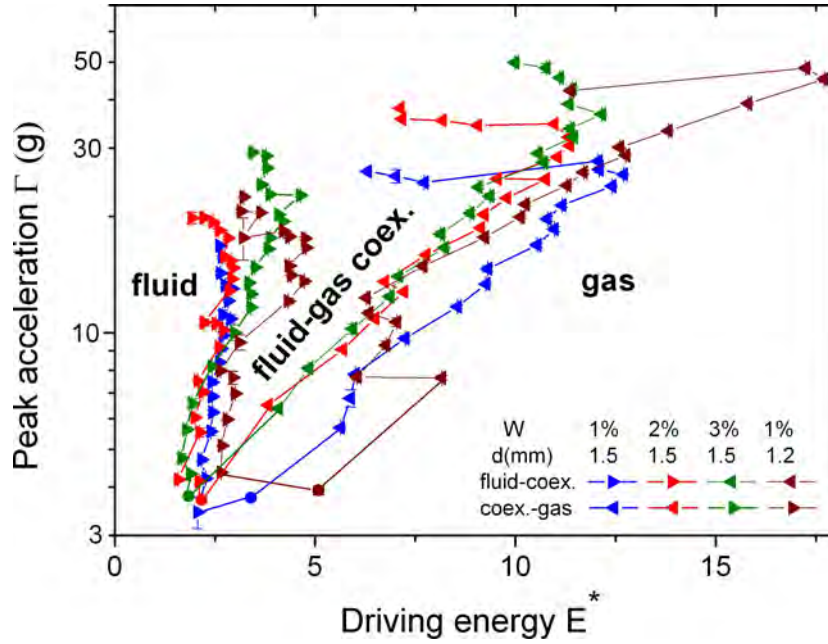


**Figure 3.24:** Phase diagram for water wetting glass spheres at different liquid content  $W$  and particle diameters  $d$  in the  $\Gamma - E^*$  plane. Figure from [R9: Huang *et al.*, 2009b].

driving force acting on the granular layer, a constant  $\Gamma$  for such a transition suggests that this transition is force driven. Here, only the threshold value for decreasing  $\Gamma$  is shown in the phase diagram because starting from a fluidlike phase lead to a more reproducible result. According to the above analysis on the hysteretic nature of this transition (see Sec. 3.4.1), the threshold for surface melting will be slightly larger.

A different behaviour is found for the transition from a fluidlike to a fluid-gas coexistence region: The transition line grows linearly with  $f$ , suggesting that the agitation velocity ( $v_p \propto \Gamma/a$ ), plays the dominating role. Here,  $\Gamma_{fc}$  is determined by the nucleation of ‘gas bubbles’, which is conveniently accessible in the experiments. Former discussions on the hysteretic nature of such a transition suggest a smaller  $\Gamma_{fc}$  for the vanishing of ‘gas bubbles’, but the difference for  $d = 1.5$  mm particles used here is negligible. The dependency of F-C transition on the driving velocity suggests a certain energy scale to overcome for a ‘gas bubble’ to nucleate. This is indeed the case since the phase diagram measured by MD simulations of a 2D system (Fig. 3.23 c) clearly shows that F-C transition corresponds to a vertical line ( $E^* \approx 1$  in the  $\Gamma - E^*$  plane, i.e. rupture energy of a single capillary bridge). A rescale of experimental data with the rupture energy scale estimated with Eq. 2.15 demonstrates as well the presence of such an energy scale, despite of being  $E^* \approx 2.5$ . Such a difference arises from the additional energy dissipation from the inelasticity of particles. This is confirmed with an implementation of a constant normal COR in the MD simulations, which leads to a shift of  $E^*$  to  $\approx 5$  (Fig. 3.23 d). Moreover, MD simulations also suggest that the detailed nature of how energy dissipated plays a minor role in phase transitions, since a change of the force laws (insets of Fig. 3.23 c) for the rupture of a capillary bridge leads to almost the same transition threshold (Fig. 3.23 c).

As shown in both experiments Fig. 3.23 (b) and MD simulations Fig. 3.23 (d), the transition from the coexistence (C) phase to the gaslike phase (G) doesn’t rely on the

energy injection  $E^*$ . Instead, it shows a tendency to follow the curve of  $a = d$ , which indicates the influence from the geometry of the system.

In Fig. 3.24, scaling of the F-C transition line with the rupture energy is further demonstrated through a variation of liquid content and particle diameter. The collapse of data in the  $\Gamma - E^*$  plane demonstrates the universal aspect of such a transition: For a ‘gas bubble’ to nucleate, sufficient energy to overcome locally the energy dissipation from inelastic collisions as well as the rupture energy of single capillary bridges is needed. Thus, we can again conclude that understanding the ‘microscopic’ energy dissipation is the key to elucidate ‘macroscopically’ collective behaviour.

Moreover, there are non-universal aspects in the phase diagram, as the C-G transition line and the kink close to the F-C-G ‘tri-critical’ point (Fig. 3.23 c and d) indicate. Those features are found to be related to the geometrical parameters including the height of the granular layer  $h$ , container height  $H$  as well as particle diameter  $d$ . For more extensive discussions on the universal and non-universal aspects of the phase diagram, the reader may refer to R11: Fingerle *et al.*, [2008] and R9: Huang *et al.*, [2009b].

### 3.4.4 Pattern formation

“Why is the universe not boring?”

An answer to the above question raised by Cross and Greenside in their book on pattern formation [Cross & Greenside, 2009] is far from trivial. However, as they suggested, one should consider the universe as an evolving non-equilibrium system as a starting point. As an equilibrium system is perturbed, or driven out of equilibrium, one ubiquitous feature is the formation of patterns, which may range from the atomic scale magnetic ordering [Ferriani *et al.*, 2008] to the growing surface of a single cell [Wada, 1966], from stirring milk on the coffee to the galaxy formation (e.g. Messier 74 is named as a perfect spiral galaxy [Messier, 2014]). One peculiar example of pattern formation is solitary waves through which energy can be kept and transferred to a long distance without dissipation. It was discovered by J. S. Russell in the 19th century [Russell, 1844] and further elaborated by mathematicians to be a balance between the nonlinearity and dispersion (see e.g. Craik [2004]). Such a localized pattern finds

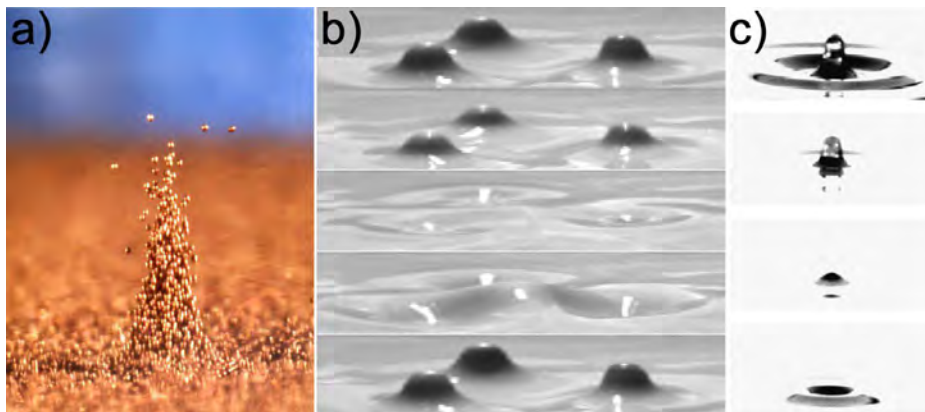


**Figure 3.25:** Localized excitations observed in (a) agitated granular media [Umbanhowar *et al.*, 1996], (b) clay suspensions [Lioubashevski *et al.*, 1999] and (c) Newtonian fluid [Arbell & Fineberg, 2000].

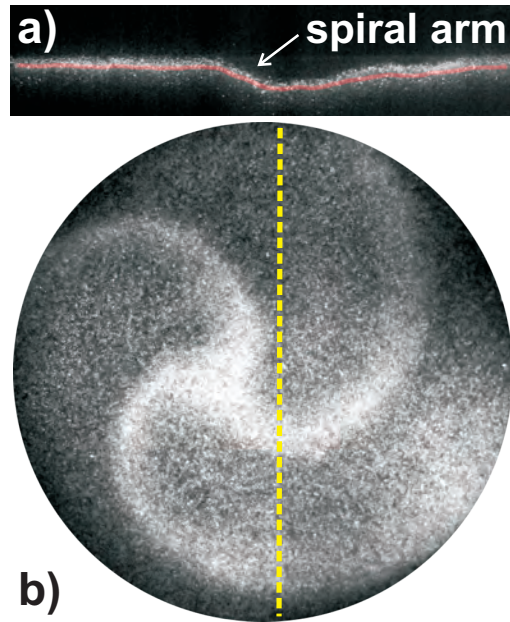


**Figure 3.26:** Snapshots of a typical 3-armed spiral pattern observed in vertically agitated thin wet granular layers: (a) is captured with the laser sheet illumination. The red half transparent line is a surface profile determined by an image processing procedure. The spiral arm corresponds to a kink between regions with different heights. (b) is obtained from the top view of the pattern (averaged over three synchronized images to enhance the contrast). The yellow line marks the region shined by the laser sheet. Images adapted from R6: Huang & Rehberg, [2011].

applications, for example, in optics [Chen *et al.*, 2012; Renninger & Wise, 2013] to transport information efficiently.

More recently, localized excitations, named as ‘oscillons’, in dissipative granular systems under vertical vibrations have been discovered in the vicinity of period doubling bifurcation [Umbanhowar *et al.*, 1996]. Figure 3.25 (a) shows a closer view of an oscillon composed of bronze particles. It is a subharmonic pattern with the peak turning into a crater in the next vibration cycle. Although oscillons arise from the highly dissipative granular systems, they persist for a long time under continuous vibrations. They can also interact with each other and form pairs, or even lattices. Later on, similar patterns are discovered in vertical agitated clay suspensions and temporarily in Newtonian fluid (Fig. 3.25 b and c), suggesting the ubiquity of such type of localized patterns.

For vertically agitated wet granular matter, a dramatically different pattern formation scenario has been found [R6: Huang & Rehberg, 2011]: 3-armed rotating spirals, as shown in Fig. 3.26 (b), are the dominating pattern. Such a pattern arises from a peculiar period tripling bifurcation that leads to the spatiotemporal chirality. With the help of laser profilometry, it is found that the spiral arms, which appear brighter in Fig. 3.26 (b), correspond to kinks separating regions with different height (Fig. 3.26 a). The existence of kinks actually indicates as well energy localization, since most of the injected energy is dissipated in the kink region where interactions between particles most frequently occur. Due to the strong cohesion from the formation of capillary bridges, the wet granular layer tends to move collectively upon agitations. At a certain

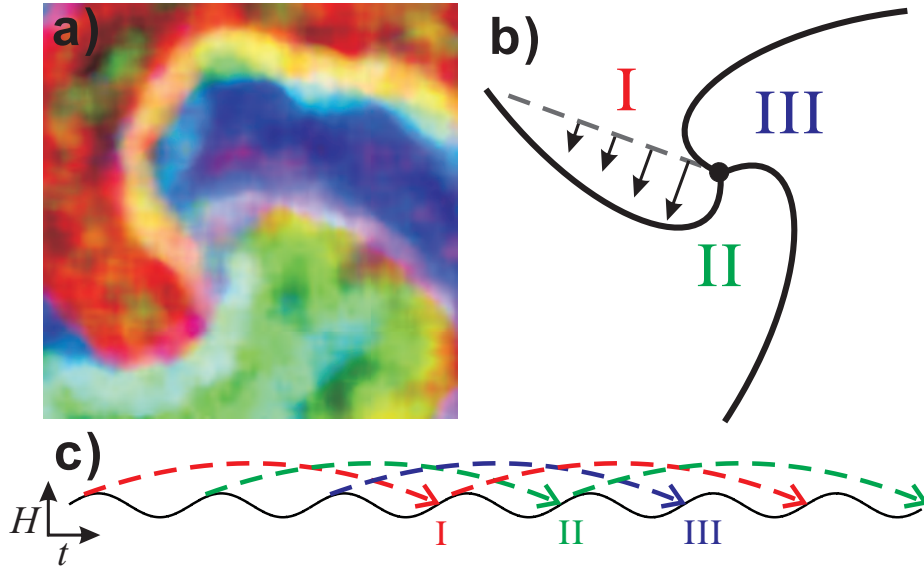


**Figure 3.27:** (a) Spatially resolved covariance between two subsequent images taken as the collision with the container occurs. They are color coded by various regions (red for I, green for II, and blue for III) separated by the spiral arms. The brightness of each color corresponds to the mobility of particles. Sketches (b) and (c) indicate the spatiotemporal chirality of the pattern (see text for detailed explanations). The black line in (c) indicates the positions of the vibrating bottom, the dash lines correspond to the center of mass in regions I, II and III.  $H$  denotes the height. Images adapted from [R6: Huang & Rehberg, 2011].

point, the energy dissipation through particle-particle interactions within the granular fluid<sup>2</sup> is not sufficient to balance the energy injection. Consequently, new forms of energy dissipation must take place: One possibility is the nucleation of ‘gas bubbles’ as discussed in Section 3.4.2, and the other possibility is the kink waves shown here.

As discussed in detail elsewhere [R6: Huang & Rehberg, 2011], period tripling actually leads to three possible phases for the agitated granular layer to choose (illustrated with various colors in Fig. 3.27). From the time evolution of the spatially resolved covariance (representing the mobility of particles) in various regions, one can find a clue for the rotation mechanism. As interpreted in Fig. 3.27 (b) and (c), the collision of region I with the container leads to a higher mobility of particles (granular temperature) there in comparison to the other two regions. Suppose energy is injected through collisions with the container bottom and dissipated through the free flying period, the kinetic temperature will have a gradient  $T_I > T_{III} > T_{II}$  at the moment region I collides with the container. Such a gradient effectively drives the expansion of region I into region III, i.e., along the highest temperature gradient. Such an expansion will typically lead to a propagating front. However, the presence of the other two kink waves, i.e. the other two spiral arms, gives rise to a central region (spiral core) within which the mobility of particles is dramatically reduced. Consequently, it is plausible to guess that the pinned spiral core region leads to a distortion of the front initially formed in a way that the particles closest to the core region obtain the highest rotation

<sup>2</sup>Note that such interactions won’t necessarily include a frequent breaking of capillary bridges, since particles within the liquidlike layer are still bound with each other via capillary bridges.

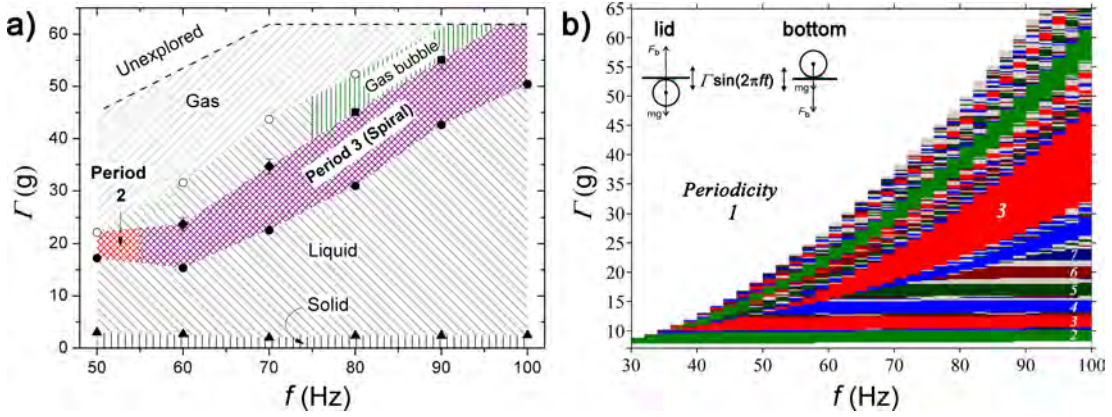


**Figure 3.28:** a) Phase diagram for 113 g (corresponding to 4~5 particle layers) water wetting glass beads ( $d \approx 780 \pm 70 \mu\text{m}$ ) with  $W = 1.6\%$  under vertical agitations [Butzhammer, 2012]. It demonstrates the dominating period tripling pattern, i.e. three armed rotating spirals. In a narrow region at  $f \approx 50$  Hz, period doubling pattern can also be observed. See Fig. 3.29 below for sample snapshots. b) Periodicity diagram from a simple model considering the whole granular layer as a single particle colliding completely inelastic with the container. Inset shows interacting forces between the granular layer and the lid or the container bottom, considered in the model. As indicated by the periodicity number overlaid on the diagram, periodicity is represented with colors. Regions painted with gray correspond to a periodicity  $\geq 7$ .

speed (see sketch in Fig. 3.27 a), and hence spiral shaped fronts are formed.

Figure 3.28 (a) shows a phase diagram for the pattern formation of agitated wet granular layers. It demonstrates that period tripling spiral is the preferred pattern, covering a wide range of  $f$  and  $\Gamma$ . Transition lines shown here correspond to an average of thresholds measured for both increasing and decreasing  $\Gamma$ , since no hysteresis is observed for the pattern to appear. As  $\Gamma$  grows above the threshold, spiral patterns spontaneously appear with a certain rotation speed and an Archimedean shape, which grows linearly with  $\Gamma$  in the pattern forming region [R3: Huang *et al.*, 2013]. It is still unclear what determines the emerging time, length scales as well as their dependency on  $\Gamma$ . Moreover, a ‘gas bubble’ region is also found in the phase diagram, which triggers the question of why one or the other dissipation mechanisms appear in the system. A comparison of phase diagrams measured with various combinations of granular layer thickness  $h$  and container height  $H$  indicates that the filling fraction  $h/H$  is the dominating factor [Butzhammer, 2012]: ‘Gas bubbles’ are more favoured for small  $h/H$ , while spiral/kink patterns are more favoured for larger  $h/H$ .

In a former work [R6: Huang & Rehberg, 2011], a simplified model was introduced to explain the favoured period tripling behaviour in the system for one certain frequency. It considers the granular layer as a single particle bouncing with  $\text{COR} = 0$  in the container. After colliding with the container wall, the particle may detach immediately or move together with the container, depending on whether the driving force is sufficiently large to overcome the sum of the capillary and gravitational forces (see the sketch in Fig. 3.28 b). Here in Fig. 3.28 (b), a diagram of periodicity from such a model for the specific experimental condition used in Fig. 3.28 (a) is presented. Qualitatively, the model predicts a dominating period tripling region (red) with its boundaries growing with  $f$ . Quantitatively, the starting  $f \approx 55$  Hz and the boundaries for  $f$  up to 80 Hz agree with the rotating spiral region formed in the experiments. For

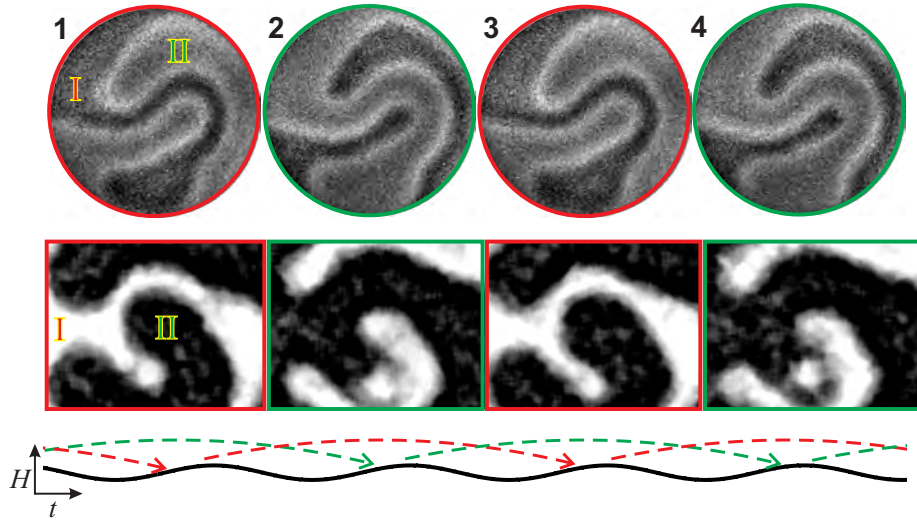


**Figure 3.29:** Upper row: Snapshots of the period doubling pattern taken at a fixed phase of 4 consequent vibration cycles. Middle row: Corresponding spatially resolved covariance at the colliding phase in the center region of the container, where the mobility of the particles are represented by the brightness of the image. Lower row: Height of the center of mass of the two anti-phase regions (marked with I and II) as a function of time. The snapshots used in the upper rows correspond to the time when region I (cycle 1 and 3, red border) or II (cycle 2 and 4, green border) collide with the vibrating bottom (black line). Collisions with the lid of the container are found to be less prominent for the period doubling pattern.

higher frequencies, the threshold for spiral pattern is underestimated by the model. This can be attributed to the enhanced energy transfer into the local vibrational degrees of freedom, i.e. the effective ‘thermal’ energy, which weakens the single particle assumption. In addition, the diagram exhibits horizontal strips with periodicity growing with  $\Gamma$ . Those regions correspond to the situation that only collisions with the container bottom occur. In those regions, we speculate that the energy injection can be well dissipated through the particle-particle interactions in the liquidlike phase, thus no additional energy dissipation mechanisms, e.g. patterns or ‘gas bubbles’, are needed.

In short, despite of the simplicity of the model, it can to some extent quantitatively predict the dominating periodicity of the pattern. More specifically, it indicates that the collisions with the lid, or to say the distance  $H - h$  for the granular layer to travel play an important role. Thus the system could in principle generate patterns with a controlled number of periodicity, e.g., four-phase patterns [Elphick *et al.*, 1998; Lin *et al.*, 2000; Meron, 1999; Marts *et al.*, 2004].

Period doubling pattern is also observed in a relatively small frequency region of the phase diagram shown in Fig. 3.28 (a). It corresponds as well to kink waves, but non-propagating. As the sequence of snapshots in Fig. 3.29 shows, the kink fronts swing back and forth as one (I) or the other (II) region collides with the container. This fact can be clearly illustrated in the same manner as the rotation of spiral arms. As the spatially resolved covariance images shown in the middle panel indicate, collisions of region I with the container bottom lead to a granular temperature gradient towards region II, thus push the kink front along the same direction. As region II collides with the container in the next vibration cycle, a reversed temperature gradient leads

to a counter-flow. Note that the curved kink fronts shown here are not the steady state, they will slowly evolve into a target pattern. Further investigations are necessary to characterize such a relaxation process, in order to shed light on the emerging line tension in such a non-equilibrium model system.

### 3.5 How does shape matter?

Most of the investigations on the dynamics of granular matter, including the ones described above, use spherical particles or circular disks as granular particles for the sake of simplicity. Despite of such simplicity, I have demonstrated above that the collective behaviour of dry as well as wet granular matter driven far from thermodynamic equilibrium is far from trivial and deserves deeper understandings. However, as shown in Fig. 2.2(a), grains picking up arbitrarily from the world outside of the lab will have a certain shape. Moreover, as demonstrated by Fig. 3.9 in Section 3.3.1, spherical particles typically used in the lab, despite of how well being polished during the manufacturing process, will exhibit time evolving surface morphologies that influence the collective behaviour such as phase transitions. Therefore, one has to bear in mind that *shape matters* while dealing with real life applications such as predictions of landslides or debris flows.

Stepping further, we can ask the follow-up question: How does shape matter? Due to the large variety of possibilities, including changes into regular or irregular shapes as well as changes at a surface or a global level, it is logic to consider the key factors that a variation of shape will deliver. One of the factors is the aspect ratio of ellipsoidal particles: It determines, as discussed in Section 1.1, how many candies can be fit into a jar. Another factor is considered to be the coordination number, i.e. how many neighbours a particle can have. It is an essential parameter accompanying with any ordered state of any particle systems, despite of being thermally or athermally driven. It is also closely related to the mechanical properties of such order states. Preliminary investigations for both parameters are presented below with dry granular rods (Subsection 3.5.1) [P2: Mueller *et al.*, 2014] and wet granular hexagons (Subsection 3.5.2) as model systems.

#### 3.5.1 Granular rods

Beside the well known example of molecules with a rod-like shape organizing into various liquid crystalline phases [Gennes & Prost, 1995], the self-organization of rod-like particles into ordered states is a universal phenomenon appearing widely in nature. Examples range from thermally driven molecules, colloids or polymers [Stephen & Straley, 1974; Onsager, 1949; Vroege & Lekkerkerker, 1992] to granular particles such as a pile of rice [Frette *et al.*, 1996] and active particles such as bacteria colonies [Zhang *et al.*, 2010], actin filaments [Schaller *et al.*, 2010], as well as animal groups [Buhl, 2006; Couzin *et al.*, 2005; Liu *et al.*, 2013]. Theoretically, considering purely hard rods with excluded volume interactions is found to be sufficient to drive the transition from an isotropic to an uniaxial nematic state [Vroege & Lekkerkerker, 1992; de las Heras *et al.*, 2013], thus triggering, again, the question of how well can those theories be applied to non-equilibrium systems.

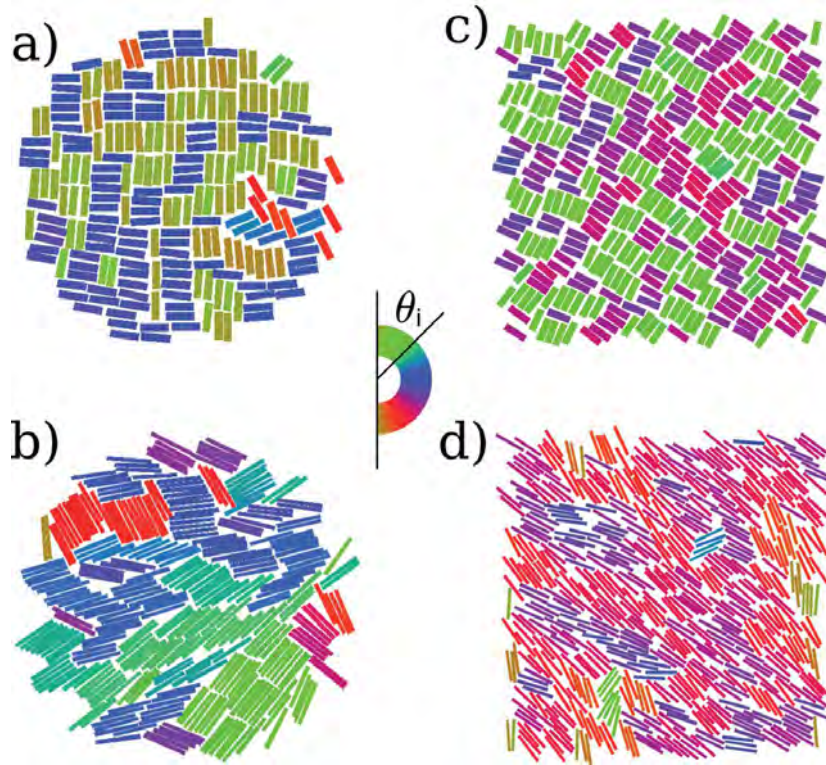


**Figure 3.30:** Typical snapshots of tetratic (upper row, aspect ratio  $l/d = 3.3$ ) and uniaxial nematic (lower row,  $l/d = 10.0$ ) ordering in the bulk. a) and b) are reconstructed from the positions and orientations of particles detected experimentally in the center region of the container. c) and d) are from Monte Carlo (MC) simulations with periodical boundary conditions. The rods are painted with various colors according to their orientations. Images adapted from P2: Mueller *et al.*, [2014].

With vertically agitated rod-shaped particles in a quasi-two-dimensional configurations as a model system, it is demonstrated that the aspect ratio and area fraction  $\phi$  are the key parameters determining the ordering transitions [P2: Mueller *et al.*, 2014]. Moreover, as presented in Fig. 3.30, the ordered states (tetratic and uniaxial nematic) from both experiments and MC simulations exhibit certain similarities. Such a striking similarity across the two dramatically different systems reveals the universality of such a transition: As long as particles are sufficiently mobilized, confinement will lead to the transition into a tetratic at low aspect ratios or a uniaxial nematic state at large aspect ratios. This finding suggests that the exact way of energy injection is not essential for the transitions, which is confirmed with a variation of  $\Gamma$  in the experiments. Quantitatively, both experiments and MC simulations suggest the same critical aspect ratio  $\approx 8.3 \pm 1.7$  separating tetratic and uniaxial nematic states. The critical area fractions measured experimentally for the ordering transitions to occur are slightly larger than those from MC simulations. Such a difference can be attributed to the fact that granular rods continuously collect energy from the vibrating plate, which may generate temporal disorder to a system that could in principle relax into an ordered state. Further experiments are being carried out presently to distinguish further universal and non-universal factors dominating the transitions.

### 3.5.2 Hexagonal disks and more

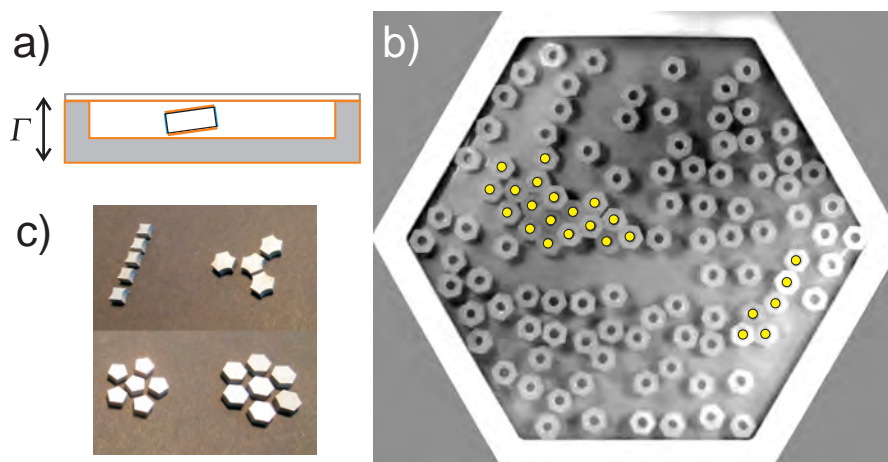


**Figure 3.31:** Clustering of wet hexagonal disks under vertical agitations. a) A sketch of the experimental set-up. The disks are treated in a way that only their side walls are hydrophilic (blue), all other surfaces are hydrophobic (orange). b) Top view of clusters formed (marked with yellow dots) by hexagonal disks in a hexagonal confinement. c) A systematic tuning of the particle shape is planned to investigate the influence from the maximum coordination number  $N_{\text{COR}}$  on the collective behaviour. Sample disks with shape designed: Upper and lower rows correspond to  $N_{\text{COR}} = 2, 3$  and  $5, 6$ .

For thermal systems, Damasceno *et al.* [2012] has analysed systematically the ordering transition of 145 various types of polyhedra. Particularly, they showed that the coordination number and the isoperimetric quotient, which measures how close to a spherical shape a particle is, are the key parameters dominating the ordered state. For particles close to spheres and with coordination number close to 12, FCC packings are preferred. While for strongly anisotropic rod-like or disk-like particles with coordination number  $\approx 2$ , as suggested in the above Section 3.5.1, liquid crystalline phases arise. Thus, the task for our athermal model system is to find out whether such a diagram applies as well to non-equilibrium systems or not.

As a starting point, hexagonal disks are used because they have the same coordination number as spherical particles confined in a quasi-two-dimensional conditions. Due to the possibility of having a much larger contact area, clusters formed by the wet disks are expected to have much stronger rigidity. To avoid such kind of rigidity enhancement at other surfaces of the disks, special efforts have been taken to allow hydrophilic surfaces only at the side walls of the disks (Fig. 3.31 a). Figure 3.31 (b) demonstrates the collective behaviour of such a model system: Different from isolated disks that move vigorously upon agitation, the rigid blocks formed by the disks (marked with yellow dots) are much less mobile: They tend to stay on the bottom of the container without any movements. In addition to the currently ongoing investigations on the comparisons between spheres and hexagonal disks, it is also planned in the future to measure the collective behaviour as well as associated ‘microscopic’ particle-particle interactions for disks with designed shapes. As shown in Fig. 3.31 (c), such a shape tuning will effectively influence the maximum number of neighbours of the particles, thus

allow a systematic investigations on the influence from the other key factor, namely the maximum coordination number in the non-equilibrium model system.

## Concluding remarks

From the dissipative interactions of granular particles at a ‘microscopic’ level, to their collective behaviour at a ‘macroscopic’ level, the studies presented in the thesis are devoted to a better understanding of the following two questions:

- How well are ‘macroscopic’ and ‘microscopic’ worlds connected through the emerging time, length and energy scales?
- How well can existing knowledges on thermal systems be extended to systems driven far from thermodynamic equilibrium?

These questions are addressed with agitated granular matter, particularly with cohesive particles, as a non-equilibrium model system. In Chapter 2, a characterization of possible energy dissipation mechanisms, particularly for the case with wetting liquid mediated, provides the critical time, length and energy scales associated with ‘microscopic’ particle-particle interactions. In Chapter 3, I have shown that those critical scales, particularly the dissipative energy scale, indeed play an important role in determining collective behaviour in the ‘macroscopic’ world, ranging from surface melting (Sec.s sections 3.3.1 and 3.4.1) to clustering (Sec. 3.3.2), from phase transitions (Sec. 3.4.3) to pattern formation (Sec. 3.4.4), despite of the direction of driving and the dimensionality. Moreover, signatures of surface melting, emerging inter-facial tension, phase separations (Sec. 3.4.2), as well as ordering transitions of rod-like particles (Sec. 3.5.1) all find their counter-parts in equilibrium systems, suggesting the essential role such a model system can take for a better understanding of non-equilibrium systems in general. Such an understanding is important since the whole universe is an evolving non-equilibrium system [Cross & Greenside, 2009].

More specifically to the physics of granular matter, careful characterizations of their dynamical behaviour are essential in a large variety of industrial applications as well as in geologically disastrous events, as introduced in Chap. 1. The characterizations of wet COR at the ‘microscopic’ level in Chapter 2 provide appropriate models for large scale simulations aiming at real life applications [Yu *et al.*, 2013]. The characterizations of collective behaviour presented in Chap. 3 demonstrate the key role that ‘microscopic’ properties can play. More importantly, possible links between the those ‘microscopic’ energy scales and ‘macroscopic’ behaviour found in various experimental investigations call for a continuum description independent on the detailed nature of energy injection and dissipation. At this point, I would like to add the following statement to the one given by Roland Clift quoted at the beginning of Chap. 2:

“Before measure properties, understand their connections.”



Concerning the road ahead, I would like to continue with the following steps toward a deeper understanding of the two general questions raised above:

1. At a ‘microscopic’ level: Develop a refined model for wet impacts considering higher order approximations and contact line dynamics, based on further characterizations on the capillary bridge forming and rupturing dynamics.
2. At a ‘macroscopic’ level: Explore possible definitions for the properties of wet granular liquid, such as the interfacial tension, and discuss the possibility to generalize those definitions to non-equilibrium systems.
3. Bridging ‘macroscopic’ and ‘microscopic’ perspectives: Represent wet granular agglomerates with the connection network of particles, and develop algorithms to characterize the topology of such networks at various simplification levels, in order to explore essential control parameters at a ‘microscopic’ level that determines the mechanical properties of wet granular matter at a ‘macroscopic’ level.
4. Addressing further the influence from shapes: Adjust systematically the maximum coordination number via tuning the shape of particles, in order to discuss the universal role that this control parameter plays in the ordering transitions of particles, across both thermal and athermal systems.

## Bibliography

- AGU 2013 Bingham canyon mine landslide. URL <http://blogs.agu.org/landslideblog/2013/04/12/>.
- ANTONYUK, S., HEINRICH, S., TOMAS, J., DEEN, N. G., BUIJTENEN, M. S. & KUIPERS, J. A. M. 2010 Energy absorption during compression and impact of dry elastic-plastic spherical granules. *Granular Matter* **12** (1), 15–47.
- AOKI, K. M., AKIYAMA, T., MAKI, Y. & WATANABE, T. 1996 Convective roll patterns in vertically vibrated beds of granules. *Phys. Rev. E* **54** (1), 874–883.
- ARANSON, I. S. & TSIMRING, L. S. 2006 Patterns and collective behavior in granular media: Theoretical concepts. *Reviews of Modern Physics* **78** (2), 641.
- ARANSON, I. S. & TSIMRING, L. S. 2009 *Granular Patterns*. Oxford University Press.
- ARBELL, H. & FINEBERG, J. 2000 Temporally harmonic oscillons in newtonian fluids. *Phys. Rev. Lett.* **85** (4), 756–759.
- AUMAÎTRE, S., SCHNAUTZ, T., KRUELLE, C. A. & REHBERG, I. 2003 Granular phase transition as a precondition for segregation. *Phys. Rev. Lett.* **90** (11), 114302.
- BAGNOLD, R. A. 1941 *The physics of blown sand and desert dunes*. Mineola, N.Y.: Methuen, London.
- BAK, P. 1999 *How Nature Works: the science of self-organized criticality*, 1 edition. New York, NY, USA: Copernicus.
- BAK, P., TANG, C. & WIESENFELD, K. 1987 Self-organized criticality: An explanation of the 1/f noise. *Phys. Rev. Lett.* **59** (4), 381–384.
- BAK, P., TANG, C. & WIESENFELD, K. 1988 Self-organized criticality. *Phys. Rev. A* **38** (1), 364–374.
- BARNOCKY, G. & DAVIS, R. H. 1988 Elastohydrodynamic collision and rebound of spheres: Experimental verification. *Phys. Fluids* **31** (6), 1324.
- BECKER, K., BECKER, M. & SCHWARZ, J. H. 2006 *String Theory and M-Theory: A Modern Introduction*. Cambridge University Press.

- BI, D., ZHANG, J., CHAKRABORTY, B. & BEHRINGER, R. P. 2011 Jamming by shear. *Nature* **480** (7377), 355–358.
- BONN, D., EGGERS, J., INDEKEU, J., MEUNIER, J. & ROLLEY, E. 2009 Wetting and spreading. *Rev. Mod. Phys.* **81** (2), 739–805.
- BOUGIE, J., MOON, S. J., SWIFT, J. B. & SWINNEY, H. L. 2002 Shocks in vertically oscillated granular layers. *Phys. Rev. E* **66** (5), 051301.
- BOWER, R. 1953 The adsorption of gases at high saturations II: The thickness of the unsaturated helium film **44**, 485.
- BREU, A. P. J., ENSNER, H.-M., KRUELLE, C. A. & REHBERG, I. 2003 Reversing the brazil-nut effect: Competition between percolation and condensation. *Phys. Rev. Lett.* **90** (1), 014302.
- BREY, J. J., CUBERO, D. & RUIZ-MONTERO, M. J. 1999 High energy tail in the velocity distribution of a granular gas. *Phys. Rev. E* **59** (1), 1256–1258.
- BRIDGES, F. G., HATZES, A. & LIN, D. N. C. 1984 Structure, stability and evolution of saturn’s rings. *Nature* **309**, 333.
- BRILLIANTOV, N. & PÖSCHEL, T. 2004 *Kinetic theory of granular gases*. Oxford; New York: Oxford University Press.
- BRILLIANTOV, N. V., SPAHN, F., HERTZSCH, J.-M. & PÖSCHEL, T. 1996 Model for collisions in granular gases. *Phys. Rev. E* **53** (5), 5382–5392.
- BUCHHOLTZ, V. & POESCHEL, T. 1996 Avalanche statistics of sand heaps. *J. Stat. Phys.* **84**, 1373, vol.84, 1373 (1996).
- BUHL, J. 2006 From disorder to order in marching locusts. *Science* **312** (5778), 1402–1406.
- BURTALLY, N., KING, P. J. & SWIFT, M. R. 2002 Spontaneous air-driven separation in vertically vibrated fine granular mixtures. *Science* **295** (5561), 1877–1879.
- BUTT, H. J. & KAPPL, M. 2009 Normal capillary forces. *Advances in Colloid and Interface Science* **146** (1-2), 48–60.
- BUTZHAMMER, L. 2012 Musterbildung in kohäsivem granulat. B. S. thesis, Universität Bayreuth.
- CAHN, J. W. 1965 Phase separation by spinodal decomposition in isotropic systems. *The Journal of Chemical Physics* **42** (1), 93–99.
- CARUS, T. L. & LEONARD, W. E. 2004 *On the Nature of Things*. Mineola, N.Y: Dover Publications.
- CASSINI 2014 About saturn & its moons. URL <http://saturn.jpl.nasa.gov/science/index.cfm?SciencePageID=55>.

- CATES, M. E. & CLEGG, P. S. 2008 Bijels: a new class of soft materials. *Soft Matter* **4** (11), 2132.
- CHEN, Z., SEGEV, M. & CHRISTODOULIDES, D. N. 2012 Optical spatial solitons: historical overview and recent advances. *Rep. Prog. Phys.* **75** (8), 086401.
- CHLADNI, E. F. F. 1787 *Entdeckungen über die Theorie des Klanges*. Leipzig: Weizmanns Erben und Reih.
- CLEMENT, E. & RAJCHENBACH, J. 1991 Fluidization of a bidimensional powder. *Europhysics Letters* **16** (2), 133–138.
- CLEWETT, J. P. D., ROELLER, K., BOWLEY, R. M., HERMINGHAUS, S. & SWIFT, M. R. 2012 Emergent surface tension in vibrated, noncohesive granular media. *Phys. Rev. Lett.* **109** (22), 228002.
- CLÉMENT, E., DURAN, J. & RAJCHENBACH, J. 1992 Experimental study of heaping in a two-dimensional “sand pile”. *Phys. Rev. Lett.* **69** (8), 1189–1192.
- COLAPRETE, A., SCHULTZ, P., HELDMANN, J., WOODEN, D., SHIRLEY, M., ENNICO, K., HERMALYN, B., MARSHALL, W., RICCO, A., ELPHIC, R. C., GOLDSTEIN, D., SUMMY, D., BART, G. D., ASPHAUG, E., KORYCANSKY, D., LANDIS, D. & SOLLITT, L. 2010 Detection of water in the LCROSS ejecta plume. *Science* **330** (6003), 463–468.
- COUDER, Y., FORT, E., GAUTIER, C.-H. & BOUDAUD, A. 2005 From bouncing to floating: Noncoalescence of drops on a fluid bath. *Phys. Rev. Lett.* **94** (17), 177801.
- COULOMB, C. A. 1773 Essay on the rules of maximis and minimis applied to some problems of equilibrium related to architecture **7**, 343.
- COUZIN, I. D., KRAUSE, J., FRANKS, N. R. & LEVIN, S. A. 2005 Effective leadership and decision-making in animal groups on the move. *Nature* **433** (7025), 513–516.
- CRAIK, A. D. 2004 The origins of water wave theory. *Annual Review of Fluid Mechanics* **36** (1), 1–28.
- CRIDA, A. & CHARNOZ, S. 2012 Formation of regular satellites from ancient massive rings in the solar system. *Science* **338** (6111), 1196–1199.
- CROSS, M. & GREENSIDE, H. 2009 *Pattern Formation and Dynamics in Nonequilibrium Systems*. Cambridge University Press.
- DAMASCENO, P. F., ENGEL, M. & GLOTZER, S. C. 2012 Predictive self-assembly of polyhedra into complex structures. *Science* **337** (6093), 453–457.
- DAS, B. M. 1997 *Advanced Soil Mechanics*. Washington: Taylor & Francis.
- DASH, J. G., REMPEL, A. W. & WETTLAUFRER, J. S. 2006 The physics of premelted ice and its geophysical consequences. *Rev. Mod. Phys.* **78** (3), 695.
- DAVIS, R., SERAYSSOL, J. M. & HINCH, E. J. 1986 The elastohydrodynamic collision of two spheres. *J. Fluid Mech.* **163**, 479.

- DAVIS, R. H., RAGER, D. A. & GOOD, B. T. 2002 Elastohydrodynamic rebound of spheres from coated surfaces. *J. Fluid Mech.* **468**, 107.
- DEEGAN, R. D. 2000 Pattern formation in drying drops. *Phys. Rev. E* **61** (1), 475–485.
- DEEGAN, R. D., BAKAJIN, O., DUPONT, T. F., HUBER, G., NAGEL, S. R. & WITTEN, T. A. 1997 Capillary flow as the cause of ring stains from dried liquid drops. *Nature* **389** (6653), 827–829.
- DONAHUE, C. M., DAVIS, R. H., KANTAK, A. A. & HRENYA, C. M. 2012 Mechanisms for agglomeration and deagglomeration following oblique collisions of wet particles. *Physical Review E* **86** (2).
- DONAHUE, C. M., HRENYA, C. M. & DAVIS, R. H. 2010*a* Stokes’s cradle: Newton’s cradle with liquid coating. *Phys. Rev. Lett.* **105** (3), 034501.
- DONAHUE, C. M., HRENYA, C. M., DAVIS, R. H., NAKAGAWA, K. J., ZELINSKAYA, A. P. & JOSEPH, G. G. 2010*b* Stokes’ cradle: normal three-body collisions between wetted particles. *Journal of Fluid Mechanics* **650**, 479–504.
- DONEV, A., CISSE, I., SACHS, D., VARIANO, E. A., STILLINGER, F. H., CONNELLY, R., TORQUATO, S. & CHAIKIN, P. M. 2004 Improving the density of jammed disordered packings using ellipsoids. *Science* **303** (5660), 990–993.
- DURAN, J. 2000 *Sands, Powders and Grains (An Introduction to the Physics of Granular Materials)*, New York: Springer-Verlag.
- DURAN, J., MAZOZI, T., CLÉMENT, E. & RAJCHENBACH, J. 1994 Size segregation in a two-dimensional sandpile: Convection and arching effects. *Phys. Rev. E* **50** (6), 5138–5141.
- DURAN, J., RAJCHENBACH, J. & CLÉMENT, E. 1993 Arching effect model for particle size segregation. *Phys. Rev. Lett.* **70** (16), 2431–2434.
- EDWARDS, D. & BRENNER, H. 1991 *Interfacial Transport Processes and Rheology*. Butterworth-Heinemann.
- EGGERS, J. 1997 Nonlinear dynamics and breakup of free-surface flows. *Rev. Mod. Phys.* **69** (3), 865–930.
- EGGERS, J. 1999 Sand as Maxwell’s demon. *Phys. Rev. Lett.* **83** (25), 5322–5325.
- ELBAUM, M. & LIPSON, S. G. 1994 How does a thin wetted film dry up? *Phys. Rev. Lett.* **72** (22), 3562–3565.
- ELPHICK, C., HAGBERG, A. & MERON, E. 1998 Phase front instability in periodically forced oscillatory systems. *Phys. Rev. Lett.* **80** (22), 5007–5010.
- ERAL, H. B., AUGUSTINE, D. M., DUTS, M. H. G. & MUGELE, F. 2011 Suppressing the coffee stain effect: how to control colloidal self-assembly in evaporating drops using electrowetting. *Soft Matter* **7** (10), 4954–4958.

- ESHUIS, P., VAN DER WEELE, K., LOHSE, D. & VAN DER MEER, D. 2010 Experimental realization of a rotational ratchet in a granular gas. *Phys. Rev. Lett.* **104** (24), 248001.
- ESHUIS, P., VAN DER WEELE, K., VAN DER MEER, D., BOS, R. & LOHSE, D. 2007 Phase diagram of vertically shaken granular matter. *Phys. Fluids* **19** (12), 123301.
- FALCON, R., KUMAR, K., BAJAJ, K. M. S. & BHATTACHARJEE, J. K. 1999 Heap corrugation and hexagon formation of powder under vertical vibrations. *Phys. Rev. E* **59** (5), 5716–5720.
- FARADAY, M. 1831 On a peculiar class of acoustical figures; and on certain forms assumed by a group of particles upon vibrating elastic surfaces. *Philosophical Transactions of the Royal Society* **121**, 299–318.
- FERRIANI, P., VON BERGMANN, K., VEDMEDENKO, E. Y., HEINZE, S., BODE, M., HEIDE, M., BIHLMAYER, G., BLÜGEL, S. & WIESENDANGER, R. 2008 Atomic-scale spin spiral with a unique rotational sense: Mn monolayer on W(001). *Physical Review Letters* **101** (2), 027201.
- FINGERLE, A., ROELLER, K., HUANG, K. & HERMINGHAUS, S. 2008 Phase transitions far from equilibrium in wet granular matter. *New J. Phys.* **10** (5), 053020.
- FREDSØE, J. & DEIGAARD, R. 1992 *Mechanics of Coastal Sediment Transport*. World Scientific.
- FRETTE, V., CHRISTENSEN, K., MALTHE-SØRENSEN, A., FEDER, J., JØSSANG, T. & MEAKIN, P. 1996 Avalanche dynamics in a pile of rice. *Nature* **379** (6560), 49–52.
- GENG, J., HOWELL, D., LONGHI, E., BEHRINGER, R. P., REYDELLET, G., VANEL, L., CLÉMENT, E. & LUDING, S. 2001 Footprints in sand: The response of a granular material to local perturbations. *Phys. Rev. Lett.* **87** (3), 035506.
- DE GENNES, P. G. 1985 Wetting: statics and dynamics. *Rev. Mod. Phys.* **57** (3), 827–863.
- DE GENNES, P. G. 1999 Granular matter: a tentative view. *Rev. Mod. Phys.* **71** (2), S374.
- GENNES, P. G. D. & PROST, J. 1995 *The Physics of Liquid Crystals*. Clarendon Press.
- GOLDHIRSCH, I. 2003 Rapid granular flows. *Annu. Rev. Fluid Mech.* **35**, 267.
- GOLDHIRSCH, I. & ZANETTI, G. 1993 Clustering instability in dissipative gases. *Phys. Rev. Lett.* **70** (11), 1619–1622.
- GOUDIE, A. S. 2013 *Arid And Semi Arid Geomorphology*. Cambridge University Press.
- GREENBERG, G. 2008 *A grain of sand : nature's secret wonder*. St. Paul, MN: Voyageur Press.

- GÖTZENDORFER, A., TAI, C.-H., KRUELLE, C. A., REHBERG, I. & HSIAU, S.-S. 2006 Fluidization of a vertically vibrated two-dimensional hard sphere packing: A granular meltdown. *Phys. Rev. E* **74** (1), 011304.
- GUYON, E., ROUX, S., HANSEN, A., BIDEAU, D., TROADEC, J.-P. & CRAPO, H. 1990 Non-local and non-linear problems in the mechanics of disordered systems: application to granular media and rigidity problems. *Rep. Prog. Phys.* **53** (4), 373.
- HALES, T. 2005 A proof of the kepler conjecture. *Annals of Mathematics* **162** (3), 1065–1185.
- HALPERIN, B. I. & NELSON, D. R. 1978 Theory of two-dimensional melting. *Phys. Rev. Lett.* **41** (2), 121.
- HALSEY, T. & LEVINE, A. 1998 How sandcastles fall. *Phys. Rev. Lett.* **80** (14), 3141–3144.
- HELD, G. A., SOLINA, D. H., SOLINA, H., KEANE, D. T., HAAG, W. J., HORN, P. M. & GRINSTEIN, G. 1990 Experimental study of critical-mass fluctuations in an evolving sandpile. *Phys. Rev. Lett.* **65** (9), 1120–1123.
- DE LAS HERAS, D., MARTÍNEZ-RATÓN, Y., MEDEROS, L. & VELASCO, E. 2013 Two-dimensional nematics in bulk and confined geometries. *Journal of Molecular Liquids* **185**, 13–19.
- HERMINGHAUS, S. 2005 Dynamics of wet granular matter. *Adv. Phys.* **54** (3), 221–261.
- HERMINGHAUS, S. 2013 *Wet Granular Matter: A Truly Complex Fluid, Series in Soft Condensed Matter*, vol. 6. World Scientific.
- HERTZ, H. 1882 Über die Berührung fester elastischer Körper. *J. reine und angewandte Mathematik* **92**, 156.
- HOEKSTRA, H., VERMANT, J., MEWIS, J. & FULLER, G. G. 2003 Flow-induced anisotropy and reversible aggregation in two-dimensional suspensions. *Langmuir* **19** (22), 9134–9141.
- HONG, D. C., QUINN, P. V. & LUDING, S. 2001 Reverse brazil nut problem: Competition between percolation and condensation. *Phys. Rev. Lett.* **86** (15), 3423–3426.
- HORNBAKER, D. J., ALBERT, R., ALBERT, I., BARABASI, A. L. & SCHIFFER, P. 1997 What keeps sandcastles standing? *Nature* **387** (6635), 765.
- HOWELL, D., BEHRINGER, R. P. & VEJE, C. 1999 Stress fluctuations in a 2D granular couette experiment: A continuous transition. *Phys. Rev. Lett.* **82** (26), 5241–5244.
- HUANG, K., RÖLLER, K. & HERMINGHAUS, S. 2009 Universal and non-universal aspects of wet granular matter under vertical vibrations. *Eur. Phys. J. Spec. Top.* **179** (1), 25–32.

- HUANG, K., ZHANG, P., MIAO, G. & WEI, R. 2006 Dynamic behaviors of supersonic granular media under vertical vibration. *Ultrasonics* **44**, e1487–e1489.
- INOUE, T. & OKAYA, K. 1994 In *Proceedings of the Eighth European Symposium on Comminution* (ed. E. Forsberg), pp. 425–437.
- IVANHOE 2011 Ivanhoe reservoir covered with 400,000 black plastic balls. URL <http://www.amusingplanet.com/2011/11/ivanhoe-reservoir-covered-with-400000.html>.
- IVESON, S. M., LITSTER, J. D., HAPGOOD, K. & ENNIS, B. J. 2001 Nucleation, growth and breakage phenomena in agitated wet granulation processes: a review. *Powder Technology* **117** (1-2), 3–39.
- JAEGER, H. M., LIU, C.-H. & NAGEL, S. R. 1989 Relaxation at the angle of repose. *Phys. Rev. Lett.* **62** (1), 40–43.
- JAEGER, H. M., NAGEL, S. R. & BEHRINGER, R. P. 1996 Granular solids, liquids, and gases. *Rev. Mod. Phys.* **68** (4), 1259.
- JANSSEN, H. A. 1895 Versuche über getreidedruck in silozellen. *Zeitschrift des Vereines deutscher Ingenieure* **39** (35), 1045–1049.
- JENSEN, P. H. J. 1998 *Self-Organized Criticality: Emergent Complex Behavior in Physical and Biological Systems*. Cambridge; New York: Cambridge University Press.
- JOP, P., FORTERRE, Y. & POULIQUEN, O. 2006 A constitutive law for dense granular flows. *Nature* **441** (7094), 727–730.
- KERR, R. A. 2010 How wet the moon? Just damp enough to be interesting. *Science* **330** (6003), 434–434.
- KHAN, Z. S. & MORRIS, S. W. 2005 Subdiffusive axial transport of granular materials in a long drum mixer. *Phys. Rev. Lett.* **94** (4), 048002.
- KNIGHT, J. B., JAEGER, H. M. & NAGEL, S. R. 1993 Vibration-induced size separation in granular media: The convection connection. *Phys. Rev. Lett.* **70** (24), 3728–3731.
- KONDIC, L. 1999 Dynamics of spherical particles on a surface: Collision-induced sliding and other effects. *Phys. Rev. E* **60** (1), 751.
- KOOS, E. & WILLENBACHER, N. 2011 Capillary forces in suspension rheology. *Science* **331** (6019), 897–900.
- LAROCHE, C., DOUADY, S. & FAUVE, S. 1989 Convective flow of granular masses under vertical vibrations. *J. Phys. France* **50** (7), 699–706.
- LIN, A. L., HAGBERG, A., ARDELEA, A., BERTRAM, M., SWINNEY, H. L. & MERON, E. 2000 Four-phase patterns in forced oscillatory systems. *Phys. Rev. E* **62** (3), 3790–3798.

- LIUBASHEVSKI, O., HAMIEL, Y., AGNON, A., RECHES, Z. & FINEBERG, J. 1999 Oscillons and propagating solitary waves in a vertically vibrated colloidal suspension. *Phys. Rev. Lett.* **83** (16), 3190–3193.
- LITSTER, J., ENNIS, B. & LIAN, L. 2004 *The Science and Engineering of Granulation Processes*. Springer.
- LIU, A. J. & NAGEL, S. R. 1998 Nonlinear dynamics: Jamming is not just cool any more. *Nature* **396** (6706), 21–22.
- LIU, Q.-X., DOELMAN, A., ROTTSCHÄFER, V., JAGER, M. D., HERMAN, P. M. J., RIETKERK, M. & KOPPEL, J. V. D. 2013 Phase separation explains a new class of self-organized spatial patterns in ecological systems. *Proc. Natl. Acad. Sci.* **110** (29), 11905–11910.
- LOSERT, W., COOPER, D. G. W. & GOLLUB, J. P. 1999 Propagating front in an excited granular layer. *Phys. Rev. E* **59** (5), 5855–5861.
- LU, P. J., CONRAD, J. C., WYSS, H. M., SCHOFIELD, A. B. & WEITZ, D. A. 2006 Fluids of clusters in attractive colloids. *Phys. Rev. Lett.* **96** (2), 028306.
- MANDELBROT, B. 2002 *Gaussian Self-Affinity and Fractals: Globality, The Earth, 1/f Noise, and R/S*. Springer.
- MANOHARAN, V. N., ELSESSER, M. T. & PINE, D. J. 2003 Dense packing and symmetry in small clusters of microspheres. *Science* **301** (5632), 483–487.
- MARÍN, L. G., GELDERBLOM, H., SUSARREY-ARCE, A., HOUSELT, A. V., LEFFERTS, L., GARDENIERS, J. G. E., LOHSE, D. & SNOEIJER, J. H. 2012 Building microscopic soccer balls with evaporating colloidal fakir drops. *Proc. Natl. Acad. Sci.* .
- MARSTON, J., YONG, W., NG, W., TAN, R. & THORODDSEN, S. 2010 Cavitation structures formed during the rebound of a sphere from a wetted surface. *Experiments in fluids* p. 1–18.
- MARTS, B., HAGBERG, A., MERON, E. & LIN, A. 2004 Bloch-front turbulence in a periodically forced belousov-zhabotinsky reaction. *Physical Review Letters* **93** (10).
- MAZZONE, D., TARDOS, G. & PFEFFER, R. 1987 The behavior of liquid bridges between two relatively moving particles. *Powder technology* **51** (1), 71–83.
- MEHTA, A. 2007 *Granular Physics*. Cambridge University Press.
- MERON, E. 1999 Phase front and synchronization patterns in forced oscillatory systems .
- MESSIER 2014 URL [http://en.wikipedia.org/Messier\\_74](http://en.wikipedia.org/Messier_74) 2014-07-02.
- MIAO, G. Q., HUANG, K., YUN, Y., ZHANG, P., CHEN, W. Z. & WEI, R. J. 2006 Formation and transport of a sand heap in an inclined and vertically vibrated container. *Phys. Rev. E* **74** (2), 021304.

- MILOTTI, E. 2002 1/f noise: a pedagogical review. *Preprint* arXiv: physics/0204033.
- MITARAI, N. & NORI, F. 2006 Wet granular materials. *Advances in Physics* **55** (1-2), 1–45.
- MSL 2013 Mars science laboratory. URL <http://mars.jpl.nasa.gov:80/msl/mission>.
- MÉTAYER, J.-F., III, D. J. S., RADIN, C., SWINNEY, H. L. & SCHRÖTER, M. 2011 Shearing of frictional sphere packings. *Eur. Phys. L* **93** (6), 64003.
- NAGEL, S. R. 1992 Instabilities in a sandpile. *Rev. Mod. Phys.* **64** (1), 321–325.
- NEWITT, D. & CONWAY-JONES, J. M. 1958 Tensile strength and capillary pressure of moist agglomerates **36**, 422.
- NEWTON, S. I. 1687 *Mathematical Principles of Natural Philosophy*.
- NIKOLAIDES, M. G., BAUSCH, A. R., HSU, M. F., DINSMORE, A. D., BRENNER, M. P., GAY, C. & WEITZ, D. A. 2002 Electric-field-induced capillary attraction between like-charged particles at liquid interfaces. *Nature* **420**, 299.
- OLAFSEN, J. S. & URBACH, J. S. 1998 Clustering, order, and collapse in a driven granular monolayer. *Phys. Rev. Lett.* **81** (20), 4369–4372.
- OLAFSEN, J. S. & URBACH, J. S. 2005 Two-dimensional melting far from equilibrium in a granular monolayer. *Phys. Rev. Lett.* **95** (9), 098002.
- ONODA, G. Y. & LINIGER, E. G. 1990 Random loose packings of uniform spheres and the dilatancy onset. *Phys. Rev. Lett.* **64** (22), 2727–2730.
- ONSAGER, L. 1949 The effects of shape on the interaction of colloidal particles. *Annals of the New York Academy of Sciences* **51** (4), 627–659.
- PIERANSKI, P. 1980 Two-dimensional interfacial colloidal crystals. *Phys. Rev. Lett.* **45** (7), 569.
- PYE, K. 2009 *Aeolian sand and sand dunes*. Berlin: Springer.
- RAYLEIGH, F. R. S. 1899 XXXVI. investigations in capillarity:—the size of drops.—the liberation of gas from supersaturated solutions.—colliding jets.—the tension of contaminated water-surfaces. *Philosophical Magazine Series 5* **48** (293), 321–337.
- REIMANN, P. 2002 Brownian motors: noisy transport far from equilibrium. *Physics Reports* **361** (2–4), 57–265.
- REIS, P. M. & MULLIN, T. 2002 Granular segregation as a critical phenomenon. *Phys. Rev. Lett.* **89** (24), 244301.
- RENNINGER, W. H. & WISE, F. W. 2013 Optical solitons in graded-index multimode fibres. *Nat. Commun.* **4**, 1719.

- REYNOLDS, O. 1885 On the dilatancy of media composed of rigid particles in contact, with experimental illustrations. *Philosophical Magazine* **20**, 469–481.
- RIETZ, F. 2013 Convection and segregation of beads in a flat rotating box. PhD thesis, Otto-von-Guericke-Universität Magdeburg.
- RISTOW, G. H. 2000 *Pattern Formation in Granular Materials*. Springer.
- RISTOW, G. H., STRASSBURGER, G. & REHBERG, I. 1997 Phase diagram and scaling of granular materials under horizontal vibrations. *Phys. Rev. Lett.* **79** (5), 833–836.
- ROBINSON, D. J. & EARNSHAW, J. C. 1992 Experimental study of colloidal aggregation in two dimensions. i. structural aspects. *Phys. Rev. A* **46** (4), 2045.
- RÖLLER, K. 2010 Numerical simulations of wet granular matter. PhD thesis, Georg-August-Universität Göttingen.
- ROELLER, K., CLEWETT, J. P. D., BOWLEY, R. M., HERMINGHAUS, S. & SWIFT, M. R. 2011 Liquid-gas phase separation in confined vibrated dry granular matter. *Phys. Rev. Lett.* **107** (4), 048002.
- ROELLER, K. & HERMINGHAUS, S. 2011 Solid-fluid transition and surface melting in wet granular matter. *Eur. Phys. Lett.* **96** (2), 26003.
- ROSATO, A., STRANDBURG, K. J., PRINZ, F. & SWENDSEN, R. H. 1987 Why the brazil nuts are on top: Size segregation of particulate matter by shaking. *Phys. Rev. Lett.* **58** (10), 1038–1040.
- RUMPF, H. 1962 *Agglomeration*. New York: AIME, Interscience.
- RUSSELL, J. S. 1844 Report on waves. *Report of the 14th Meeting of the British Association for the Advancement of Science* pp. 311–390.
- SAND 2014 Sand festival. URL [http://en.wikipedia.org/wiki/Sand\\_festival](http://en.wikipedia.org/wiki/Sand_festival) 2014-05-27.
- SCHALLER, V., WEBER, C., SEMMRICH, C., FREY, E. & BAUSCH, A. R. 2010 Polar patterns of driven filaments. *Nature* **467** (7311), 73–77.
- SHEEL, M., GEROMICHALOS, D. & HERMINGHAUS, S. 2004 Wet granular matter under vertical agitation. *J. Phys.: Condens. Matter* **16** (38), S4213–S4218.
- SHEEL, M., SEEMANN, R., BRINKMANN, M., DI MICHIEL, M., SHEPPARD, A., BREIDENBACH, B. & HERMINGHAUS, S. 2008 Morphological clues to wet granular pile stability. *Nat. Mater.* **7** (3), 189–193.
- SCHERER, M. A., KÖTTER, K., MARKUS, M., GOLES, E. & REHBERG, I. 2000 Swirling granular solidlike clusters. *Phys. Rev. E* **61** (4), 4069–4077.
- SCHNAUTZ, T., BRITO, R., KRUELLE, C. A. & REHBERG, I. 2005 A horizontal brazil-nut effect and its reverse. *Phys. Rev. Lett.* **95** (2), 028001.
- SCHOFIELD, A. & WROTH, P. 1968 *Critical State Soil Mechanics*.

- SCHRÖTER, M., NÄGLE, S., RADIN, C. & SWINNEY, H. L. 2007 Phase transition in a static granular system. *Eur. Phys. Lett.* **78** (4), 44004.
- SCHRÖTER, M., ULRICH, S., KREFT, J., SWIFT, J. B. & SWINNEY, H. L. 2006 Mechanisms in the size segregation of a binary granular mixture. *Phys. Rev. E* **74** (1), 011307.
- SCOTT, G. D. 1960 Packing of spheres: Packing of equal spheres. *Nature* **188** (4754), 908–909.
- SCOTT, G. D. & KILGOUR, D. M. 1969 The density of random close packing of spheres. *Journal of Physics D: Applied Physics* **2** (6), 863–866.
- SHINBROT, T. & MUZZIO, F. J. 1998 Reverse buoyancy in shaken granular beds. *Phys. Rev. Lett.* **81** (20), 4365–4368.
- SPAHN, F. & SCHMIDT, J. 2006 Hydrodynamic description of planetary rings. *GAMM-Mitt.* **29**, 115.
- STAMOOU, D., DUSCHL, C. & JOHANNSMANN, D. 2000 Long-range attraction between colloidal spheres at the air-water interface: The consequence of an irregular meniscus. *Phys. Rev. E* **62** (4), 5263–5272.
- STEPHEN, M. J. & STRALEY, J. P. 1974 Physics of liquid crystals. *Rev. Mod. Phys.* **46** (4), 617–704.
- STRASSBURGER, G. & REHBERG, I. 2000 Crystallization in a horizontally vibrated monolayer of spheres. *Phys. Rev. E* **62** (2), 2517–2520.
- STRANDBURG, K. J. 1988 Two-dimensional melting. *Rev. Mod. Phys.* **60** (1), 161–207.
- STRATFORD, K., ADHIKARI, R., PAGONABARRAGA, I., DESPLAT, J. C. & CATES, M. E. 2005 Colloidal jamming at interfaces: A route to fluid-bicontinuous gels. *Science* **309** (5744), 2198–2201.
- STRONGE, W. J. 2004 *Impact Mechanics*. Cambridge University Press.
- TENNAKOON, S. G. K., KONDIC, L. & BEHRINGER, R. P. 1999 Onset of flow in a horizontally vibrated granular bed: Convection by horizontal shearing. *Europhysics Letters* **45** (4), 470–475.
- THORNTON, C. 1997 Coefficient of restitution for collinear collisions of elastic-perfectly plastic spheres. *J. Appl. Mech.* **64** (2), 383–386.
- THORODDSEN, S. T. 2006 Fluid dynamics: Droplet genealogy. *Nat. Phys.* **2** (4), 223–224.
- THORODDSEN, S. T. & TAKEHARA, K. 2000 The coalescence cascade of a drop. *Physics of Fluids* **12** (6), 1265–1267.
- UEPG 2013 European aggregates association: Annual review 2012-2013. URL <http://www.uepg.eu/>.

- UMBANHOWAR, P. B., MELO, F. & SWINNEY, H. L. 1996 Localized excitations in a vertically vibrated granular layer. *Nature* **382** (6594), 793–796.
- VANEL, L., HOWELL, D., CLARK, D., BEHRINGER, R. P. & CLÉMENT, E. 1999 Memories in sand: Experimental tests of construction history on stress distributions under sandpiles. *Phys. Rev. E* **60** (5), R5040–R5043.
- VASSILEVA, N. D., VAN DEN ENDE, D., MUGELE, F. & MELLEMA, J. 2005 Capillary forces between spherical particles floating at a liquid-liquid interface. *Langmuir* **21** (24), 11190–11200.
- VÖLKEL, S. 2014 Messung der Kontaktwinkelhysterese von Wassertropfen auf einer horizontalen Teflonoberfläche. B. S. thesis, Universität Bayreuth.
- VROEGE, G. J. & LEKKERKERKER, H. N. W. 1992 Phase transitions in lyotropic colloidal and polymer liquid crystals. *Rep. Prog. Phys.* **55** (8), 1241.
- WADA, K. 1966 Spiral growth of nacre. *Nature* **211** (5056), 1427–1427.
- WEIR, G. & TALLON, S. 2005 The coefficient of restitution for normal incident, low velocity particle impacts. *Chemical Engineering Science* **60** (13), 3637.
- WHITESIDES, G. M. & GRZYBOWSKI, B. 2002 Self-assembly at all scales. *Science* **295** (5564), 2418–2421.
- WILD, M. 2013 Oberächenschmelzen granularer Materie. Diploma thesis, Universität Bayreuth.
- WILLETT, C. D., ADAMS, M. J., JOHNSON, S. A. & SEVILLE, J. P. K. 2000 Capillary bridges between two spherical bodies. *Langmuir* **16** (24), 9396–9405.
- WILLS, B. A. 1997 *Mineral processing technology*, 6. Oxford, U. K.: Butterworth-Heinemann.
- YOKOYAMA, T., TAMURA, H., USUI, H. & JIMBO, G. 1994 In *Proceedings of the Eighth European Symposium on Comminution* (ed. E. Forssberg), pp. 413–425.
- YU, A., DONG, K., YANG, R. & STEFAN, L. (eds.) 2013 *Powders and grains 2013: proceedings of the 7th International Conference on Micromechanics of Granular Media*, vol. 1542. Melville, New York: American Institute of Physics.
- YUNKER, P. J., STILL, T., LOHR, M. A. & YODH, A. G. 2011 Suppression of the coffee-ring effect by shape-dependent capillary interactions. *Nature* **476** (7360), 308–311.
- ZACCARELLI, E. 2007 Colloidal gels: equilibrium and non-equilibrium routes. *J. Phys.-Condes. Matter* **19** (32).
- ZHANG, H. P., BE’ER, A., FLORIN, E.-L. & SWINNEY, H. L. 2010 Collective motion and density fluctuations in bacterial colonies. *Proc. Natl. Acad. Sci.* **107** (31), 13626–13630.

